DESIGN AND ANALYSIS OF A LOW TEMPERATURE

CO-FIRED CERAMIC MICRO COMBUSTOR

by

Matthew H. McCrink

A thesis

submitted in partial fulfillment

of the requirements for the degree of

Master of Science in Mechanical Engineering

Boise State University

May 2010

BOISE STATE UNIVERSITY GRADUATE COLLEGE

DEFENSE COMMITTEE AND FINAL READING APPROVALS

of the thesis submitted by

Matthew H. McCrink

Thesis Title: Design and Analysis of a Low Temperature Co-Fired Ceramic Micro Combustor

Date of Final Oral Examination: 28 July 2009

The following individuals read and discussed the thesis submitted by student Matthew H. McCrink, and they evaluated his presentation and response to questions during the final oral examination. They found that the student passed the final oral examination.

Donald G. Plumlee, Ph.D.   Chair, Supervisory Committee

Amy Moll, Ph.D.   Member, Supervisory Committee

John F. Gardner, Ph.D.   Member, Supervisory Committee

The final reading approval of the thesis was granted by Donald G. Plumlee, Ph.D., Chair of the Supervisory Committee. The thesis was approved for the Graduate College by John R. Pelton, Ph.D., Dean of the Graduate College.

ABSTRACT

This thesis details the design and construction of a Low Temperature Co-Fired Ceramic (LTCC) micro combustion system. The design of the combustor requires a detailed analysis of the flame's operational properties and stability. To this end, an analytic model was created to address these concerns. These results were used in conjunction with a detailed numerical analysis to determine the stable operating range of the combustors. The combustion of gaseous fuels requires a device with a lower bound on the channel feature size. This lower limit for combustion corresponds to the minimum quenching distance of the specific fuel being used and usually corresponds to the upper end of silicon MEMs processing techniques and the lower end of meso-scale production processes. This millimeter size range represents the normal feature size range for the LTCC tape system. A potential material imposed restriction to using LTCC is the relatively low temperature operating range when compared to the adiabatic flame temperatures encountered in the combustion of gaseous fuels.

To address this concern an analytic model of the heat transfer from a simple straight channel device is presented. This model allows for the analysis of the thermal loads in the substrate as well as provides insight into the effects of the channel geometry on the stability of the flame. Several experimental devices were designed and tested in accordance with the predictions of the analytic model. These devices have similar geometric configurations with different characteristic lengths to explore the feasible

operating regimes of the LTCC micro combustor. This allows for the validation of the flame stability margins and heat transfer properties predicted by the analytic model.

Infrared imaging allows for the mapping of the device surface temperature and provides a correlation mechanism to the analytic model. The results of the experimental testing show the same trending characteristics predicted by the analytic analysis. However, a detailed numerical analysis is needed to fully capture the quantitive power production capabilities of the device.

TABLE OF CONTENTS

LIST OF FIGURES

LIST OF EQUATIONS

INTRODUCTION

The explosive growth of miniature electronic devices in recent years necessitates a reevaluation of their power sources. The design push for electronics manufacturers of mobile devices is, and always has been, to create devices that best utilize the limited power available from the devices batteries. This one single feature provides the largest constraint on device longevity and field performance. The maturity of the micro-fluidic micro electro-mechanical systems, or MEMS could provide an alternative to the standard chemical battery to address the needs of high power, long life mobile devices. There are a myriad of options for micro-scale power production, including passive scavenging, micro combustion, and micro fuel cell technologies. Developing power in micro power devices is typically accomplished catalytically or through direct combustion, relying on the heat generated to power a thermo-ionic generation device or chemical fuel cell. The high potential power output of these micro power devices necessitates a serious look into their design and fabrication.

A large percentage of the work done in the micro combustion field has relied on the silicon MEMS processing techniques borrowed from the electronics industry. While using silicon has advantages in being well understood and readily available, it poses problems when trying to create complex, three-dimensional geometries. Others have tried using sintered metals from three-dimensional rapid prototyping devices with great success, shown in Figure 1. However, the machines and materials used to create these

devices can be prohibitively expensive for high volume production and are usually reserved for rapid prototyping processes.
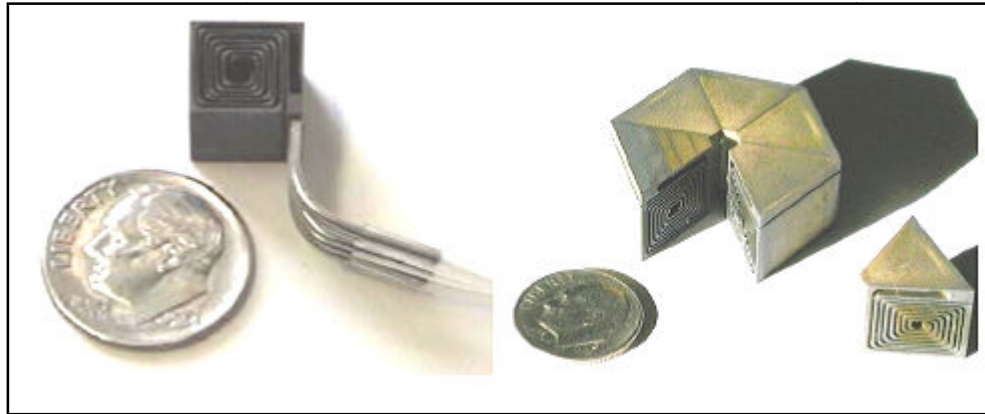
Figure 1: Swiss roll micro combustion devices, fabricated using a sintered metal rapid prototyping machine (Sitzki, Borer, Schuster, Ronney, & Wussow, 2001).

A potential solution to the need for a materials system that can rapidly and economically produce three-dimensional micro-fluidic systems is Low Temperature Co-fired Ceramics, or LTCC. LTCC is a ceramic substrate initially designed for electronics packaging in high frequency and harsh environment applications. LTCC has been used in a myriad of applications from micro-fluidic systems to embedded sensors and actuators. The material has a relatively high sintering temperature of approximately 850 C, and can be readily formed into complex structures using inexpensive processing techniques (DuPont, 2001). These complex three-dimensional structures can also take advantage of LTCC's original purpose by allowing for embedded electrical circuits using a host of pastes produced by various manufacturers. These available options make it an attractive choice for use in the development of a chemical combustion system requiring

high temperature stability, complex geometries, and embedded control circuitry (DuPont, 2001).

The work presented in this thesis is a full life-cycle process, which describes the development of the micro-combustion idea from its conceptual stage through the design and experimental testing phases. This includes the development of an advanced analytic model of the devices performance and the creation of a numeric model to extract detailed heat transfer performance parameters. These analytic and numerical performance parameters formed the basis for the experimental investigation. Relevant design decisions and construction techniques are presented throughout the thesis.

LTCC

The LTCC materials system is a common packaging material used in the electronics industry. One common electronics use of LTCC is in wireless sensor and transmitter packaging. LTCC is ideal for this type of application due to its low dielectric loss and ability to support integrated passive circuitry, shown in Figure 2. These passive devices, such as resistors, capacitors, and inductors are formed using printed co-fired pastes. In the fired state, the LTCC encapsulates the passive components, forming a multilayer, hermetically sealed device. The ability to stack the embedded circuitry in the vertical direction creates a smaller overall device size and increased component density.
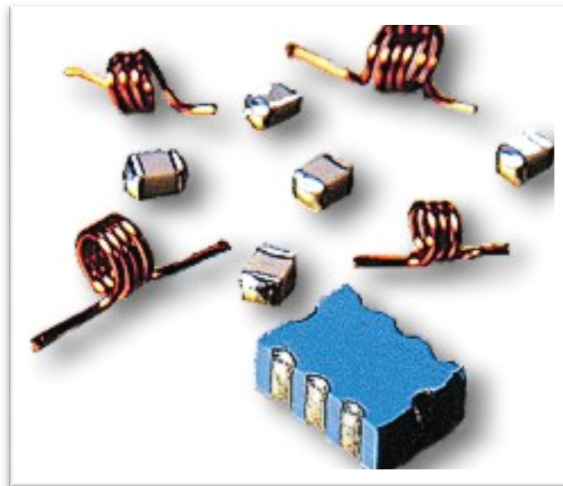
Figure 2. Passive components that can be integrated into the LTCC substrate (NovaSensor).

The processing of the LTCC material is performed in what is known as the "green" state. This "green" material contains a binder element that allows the material to be flexible and workable. The LTCC material is composed primarily of glass, alumina, and an organic binding agent.   When the "green" material is fired at approximately 850

C, the organic binder volatizes, the glass flows and forms a solid glass-alumina structure. The volatization of the organic binder and densification of the glass ceramic matrix results in a device that is smaller in the post-fired state than in the green state by approximately 13 percent in the x and y directions, and 15 percent in the z direction (DuPont, 2001). These shrinkage margins are unique to the specific type of LTCC being used. For the devices presented in this research, the base material is DuPont's 951 LTCC tape. There are different LTCC compositions that minimize the transverse shrinkage produced by both DuPont and other manufacturers. For the purposes of this research, the shrinkage of DuPont's 951 tape is well characterized and easily offset during the design phase (DuPont, 2001). This is accomplished by increasing the pre-fired dimensions of all critical features by the 12-15 percent shrinkage margin.

The fabrication process used in the construction of LTCC devices is capable of creating multi layer devices with features much larger than what is possible in a similar silicon process. An example of the multi layer capability is the ion mobility spectrometer created by Boise State University's ceramic MEMS, or C-MEMS, laboratory, shown in Figure 4 (Plumlee, 2007). The standard production cycle for a LTCC device is shown in Figure 3.
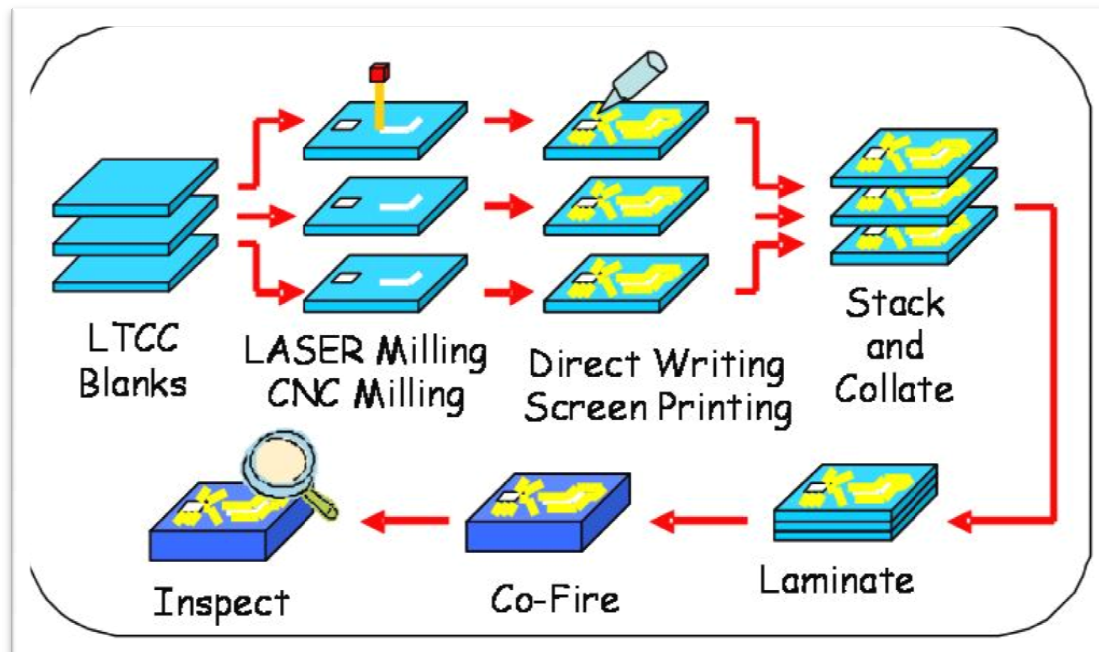
Figure 3. LTCC manufacturing process as used by Boise State University's CMEMS laboratory(Plumlee, 2007).

The standard construction process for the micro combustion devices relies on internal features created using a CNC LASER milling station and a CNC rotating bit mill. The minimum feature size for these processes is approximately 250 μm. Using femtosecond ablative LASER milling, the minimum feature sized can be reduced to the tens of microns range. After the creation of the geometric features, passive elements and conductive traces are added. The most common method used to create the traces and passives in industry are screen-printing. This method produces traces with a minimum spacing of 50 μm, covering the standard spacing of most surface mounted components. A more advanced paste deposition machine allows for a 50 μm minimum feature size at the expense of a longer production times.
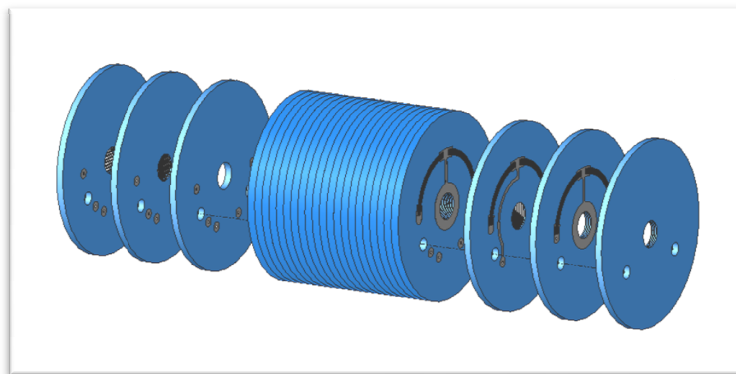
Figure 4. Multi layer LTCC ion mobility spectrometer. Picture depicts embedded electrode capability in multi layer devices (Plumlee, 2007).

Demands from research and development firms for improved LTCC resulted in second and third generation LTCC tapes. These second and third generation tapes require less processing, while maintaining the same capabilities of the first generation tape. The second-generation tapes do not require the pressure lamination of the individual layers, potentially reducing the incidence of collapsed channels and flattened features. The third- generation tape is self-constrained and requires no pressure lamination. This tape will reduce the effect of misaligned vias that occur during the firing process (DuPont, 2003). DuPont also has a photoimageable tape capable of forming geometric features as small as 50 μm. Ultraviolet light exposes the photo resist on the surface of the tape. This production process closely mirrors standard glass and silicon fabrication techniques and allows for the use of similar machines and line processes. The LTCC is exposed and etched using a one percent sodium carbonate solution and then fired. This manufacturing process lends itself to the creation of wave filters, which require high fidelity microstructures to filter specific microwave frequencies (Taylor, Bidwell, &

Lawrence, 2001). A supplemental advantage to the photoimageable tapes is the ability to perform batch processing using tape reels instead of individual sheets.

The scope of applications for ceramic packaging materials has increased in the last five years due to their feature size and geometric construction advantages over standard silicon MEMS. Multi-layer ceramic materials can incorporate micro heat exchangers and heat pipes for thermal control (Jones, Liu, & Zampino, 2003), shown in Figure 5, and three-dimensional electronic and micro-fluidic paths (Peterson, et al., 2005); (Golonka, Zawada, Radojewski, Rogusczack, & Stefanow, 2006). Sensors and actuators can be integrated directly into the substrate materials. (Gongora-Rubio, 1999). The LTCC material system has been used to develop chemical and biological reactors (Sadler, Changrani, Roberts, Chia-Fu, & Zenhausern, 2003), micro-fluidics and miniaturized analysis systems (Thelemann, Thrust, & Hintz, 2002). This new class of devices has been termed Ceramic-MEMS (C-MEMS).
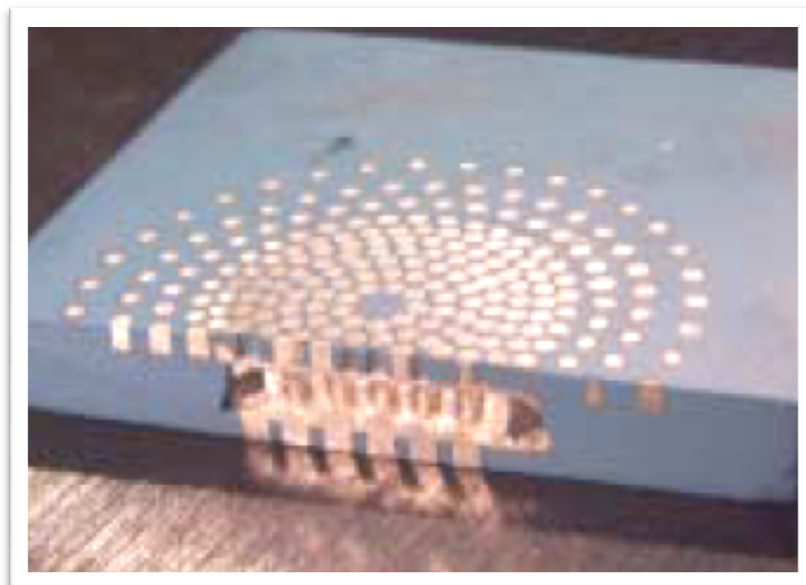
Figure 5. Micro heat exchanger in LTCC. Embedded conductive pastes can also be used as a thermal control mechanism (Jones, Liu, & Zampino, 2003).

C-MEMS Design and Fabrication Process

The process of creating the fluidic and electrical components in the LTCC material has been developed by the C-MEMS laboratory at Boise State University (Plumlee, 2007). The design process begins with a layer-by-layer model created using the SolidWorks computer aided design (CAD) environment. This model includes all internal channels, vias, and electrical circuits that will be present in the final design as shown in Figure 6. Figure 6 represents a sample device that contains the major features common to both micro fluidic devices and micro combustion devices. This design contains a fluidic inlet port on the top surface of the device and the embedded spark electrodes needed for the ignition process. The ability to discretize the design into multiple layers is another attractive feature of the LTCC material system. It is a simple matter to add or remove layers and features in the CAD program, which allows for rapid design iterations and improvements. The three-dimensional CAD file is split into its constitutive two-dimensional layers for printing and saved in the required format for the specific milling machine being used.
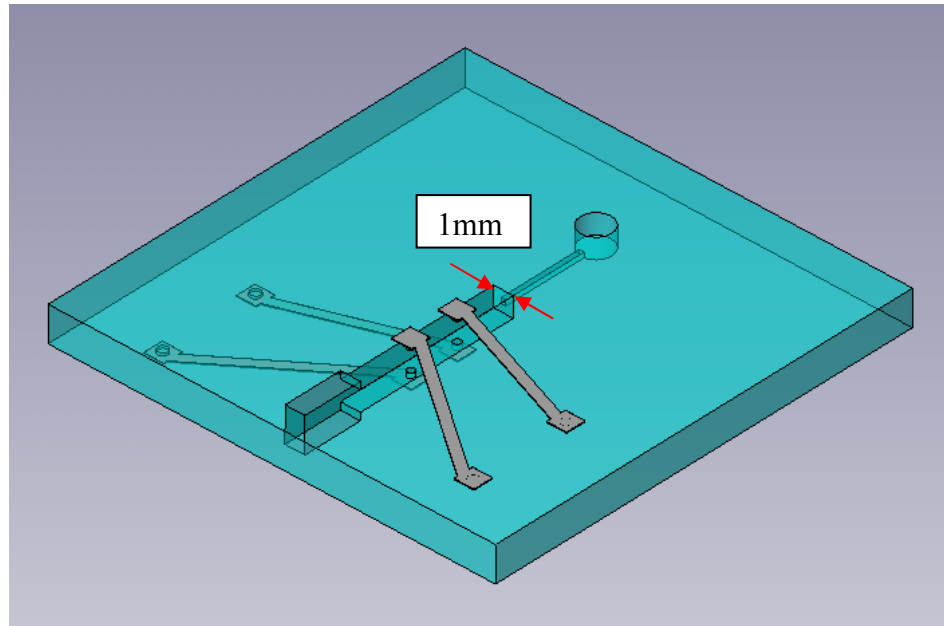
Figure 6. Initial concept device for LTCC micro combustor. Note fluidic entry port and embedded spark ignition circuitry.

After the design of the electronic circuitry and channel geometries, the two dimensional sheet images are transferred to the LTCC green tape via LASER or rotating bit milling. Each process has its own unique advantages and is used to create different features in the fired part. The LASER system excels in rapidly creating fine features in single layers of LTCC material and is shown in Figure 7. The minimum feature size of the LASER is 0.10 mm using the maximum dots per inch (DPI) resolution setting. This minimum is related to the minimum spot size of the CO_2 LASER using the enhanced optics. The rotating bit milling machine is capable of producing a minimum feature size of 0.25mm, limited by the available bit sizes. Unlike the LASER system, there is a much smaller heat affected zone in the part using the rotating bit mill. The bit mill is also capable of performing a hog-out, or a multilayer material removal machining process, on pre-laminated LTCC structures, allowing the creation of standalone structures not

possible using the LASER mill. The main disadvantage to the rotating bit mill is the significantly longer and more user intensive production time.

Figure 7. CNC LASER milling machine. Used in all milling operations for the LTCC micro combustor (Systems, Universal LASER, 2009).

The next step common to most designs is to deposit pastes and sacrificial tapes to the individual milled layers. The sacrificial tapes used in this design process are carbon sheets with the same thickness as the LTCC layers. The sheets support internal features during the lamination phase, but are burnt out during the firing cycle. The pastes used for the construction of the micro combustion device include a silver-based material used to print conductive traces for the spark electrode system. This paste contains silver, an organic frit binder, glass, and solvent, allowing it to flow during processing. The binders burn out during the firing process in much the same way as the base LTCC material, forming hermetically sealed internal circuitry. The most cost and time effective method for depositing the traces on the substrate material is to use an electrode stencil and palatte

knife blade. The same alignment pins are used for the stencil and collating steps, ensuring accurate placement of the traces. The palatte knife is used as a squeegee to force the paste through the stencil and onto the substrate surface. Using this method, the trace sizes are dictated by the thickness of the stencil material being used, typically 0.1mm. An alternative method to the manual printing of circuitry elements is using the screen-printing machine. This method is more time intensive in the setup phases of production, but produces superior results in high volume production with a minimum spacing capability of 0.2mm. If the specific part requires extremely accurate traces, the direct write tool may be used, shown in Figure 8. This machine features a conformal mapping function to accurately and repeatedly produce traces of 0.05mm on non-uniform surfaces. This ability allows for close control of resistive and capacitive circuitry.

Figure 8. Direct write machine. Used for precision paste application for spark electrodes.

The milled and patterned substrate sheets are then collated and aligned in a steel alignment jig. This jig allows for accurate alignment of through sheet vias and minimizes

the shifting of layers during the lamination phase. The collated layers are pressed at 70°C and a pressure of 20 MPa for ten minutes in a hot uni-axial press, shown in Figure 9. The heat and pressure present in the lamination press allow the organic binders in the LTCC material to flow, causing the sheets to fuse into a single base substrate. The relatively large channels found in micro combustion devices necessitate the use of sacrificial carbon tape during the lamination and firing phase. This sacrificial tape acts as a support matrix during lamination, keeping the channel's ceiling from collapsing. The base material of the tape is a carbon film and binding agent. The tape is the same thickness as the individual LTCC sheets and is patterned in the same way. During the firing process, the carbon supports the channel while the organic binder burns out, at 600 C, the carbon burns out, leaving a clean cavity and sag free channel ceilings.

Figure 9. Laboratory unidirectional hot press. Used for prelamination of LTCC layers (Plumlee, 2007).

The laminated device is co-fired in a programmable laboratory box furnace. At approximately 350 C, the organic binder material burns away, leaving a glass and

alumina mixture. The part is then heated to 850 C allowing the glass to flow and allowing the part to sinter. As previously mentioned, during the sintering phase, the part undergoes 13 percent shrinkage in the x and y directions and 15 percent shrinkage in the z direction. The embedded circuitry and LTCC co-sinter to form a dense structure with hermetically sealed electrical circuitry. A specific difficulty encountered during the firing phase was the axial splitting of the upper channel wall. The proposed failure mechanism is the uneven sintering and ensuing shrinkage of the material in the channel ceiling that occurs during the firing phase. This uneven sintering is due to rapid temperature rises in the furnace, leading to sustained temperature gradients in the substrate material. To mitigate the uneven heating and shrinking of the component, the ramp rates were halved over the standard firing cycle. This allowed the part to reach thermal equilibrium at the plateau temperatures uniformly and minimized the amount of localized sintering and shrinking. This longer ramp rate resulted in no device failures due to splitting after its implementation.

The fired LTCC component can then undergo a large variety of post processing depending on the application. The usual post-fire applications are soldering, glass frit bonding, wire bonding, and brazing. Multiple fired ceramic parts can be joined using a glass frit material. This same material also allows for the application of post-fired sapphire viewing ports for flow visualization. While it is possible to embed the windows during the initial firing process, it is difficult to size the slot in the LTCC to account for its shrinkage and the different thermal expansion coefficients of the sapphire and LTCC. It is also possible to incorporate integrated circuit chips via flip-chip soldering or a solder

paste reflow process. This process opens LTCC to the wide array of commercially available surface mount IC components.
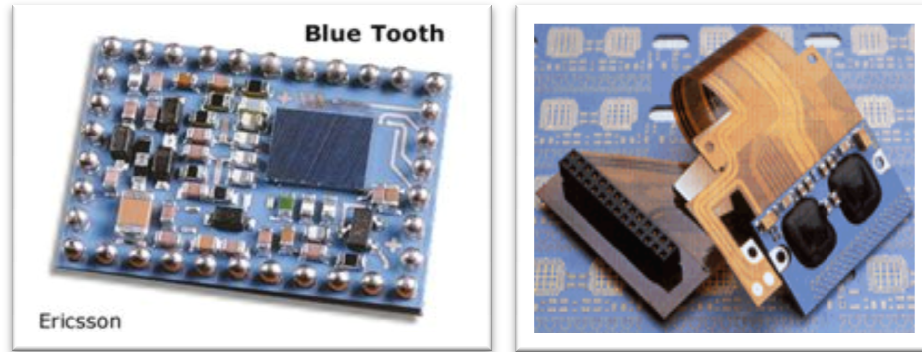
Figure 10. Commercially available LTCC devices. The image on the right is the Ericsson Bluetooth module. On the left is the Seagate hard drive components (courtesy of Ericsson and Seagate).

The bonding of fluidic interconnects presents a challenge for almost all micro fluidic substrates. In the standard silicon and glass fluidic structures, the only viable attachment options are direct mechanical seals through clamps and o-rings or epoxy sealing. LTCC adds additional interfacing options including brazing and glass reflow compounds used to bond glass and metallic fittings. It is also possible to co-fire sapphire tubes into the LTCC, taking advantage of the inherent shrinking to form the seal between the tube and substrate. This process has been pressure tested to 5 atm with no reported leakage (Younsgman, 2006). For the micro combustors presented in this work, an external clamp and o-ring seal function as the fluidic interconnect to the experimental apparatus detailed in subsequent sections. This facilitates rapid changing of the devices and limits the possibility of mechanical failure of the interconnecting surface.

Global Performance Estimation

The design of a complicated combustion system requires many assumptions regarding the geometric and fluidic design of the device in order to determine feasible stable operating parameters. On the simplest level however, the efficiency and power capacity of any combustion system is primarily a function of the mass flow rate of the fuel and oxidizer, termed the reactants, and their equivalence ratio. The mass flow rate of the reactants refers to the amount of reactants present in the combustion region at any given moment in time. Simply putting a mixture of fuel and oxidizer in the chamber is not sufficient to guarantee combustion. Controlling the equivalence ratio, or the fuel to oxidizer ratio, ensures that there is enough oxidizer to react with the available fuel. If the fuel and oxidizer are perfectly balanced, known as stoichiometric proportions, then the equivalence ratio is one, if however if the fuel to oxidizer ratio is greater than the stoichiometric case, then the flame is termed fuel rich, with an equivalence ratio greater than one. Conversely, if the fuel to oxidizer ratio is lower than the stoichiometric case then the flame is termed fuel lean. If the fuel and oxidizer are present in the right equivalence ratio range to sustain a flame, the heat released is proportional to the flux of reactants into the combustion chamber, described by the mass flow rate. The heat released through combustion can also be controlled by holding the mass flow rate constant and varying the reactant proportions. By reducing the oxidizer to fuel ratio below unity, referred to as the fuel rich condition, the products of the reaction will include an unused amount of fuel. Passing fuel through a system without reacting it limits the maximum flame temperature, but is inherently inefficient and is usually avoided in favor of operating in the fuel lean condition. The fuel lean condition refers to

an excess amount of oxidizer in the reactant stream. Operating in the fuel lean condition allows for the complete use of the available fuel while limiting the maximum temperature of the products due to the increased enthalpy fraction of the oxidizer in the mixture.

The power available from the reactants is a function of the reactant mass flow rate, the specific fuel being used, and the equivalence ratio. The dependence on the equivalence ratio is graphically depicted in Figure 11. The maxima of the graph corresponds to the highest attainable flame temperature with a hydrogen and air flame. For most hydrocarbon fuels such as methane and butane, the maximum flame temperature for the given reactant mixture, termed the adiabatic flame temperature, occurs at an equivalence ratio of one, signifying complete combustion of the fuel and hence the maximum energy release. The adiabatic flame temperature is calculated by assuming the heat released through combustion goes solely to raising the temperature of the products. Hydrogen differs slightly in that it is much more diffusive than standard hydrocarbon fuels, shifting its maxima closer to an equivalence ratio of 1.1 and broadening the temperature curve.
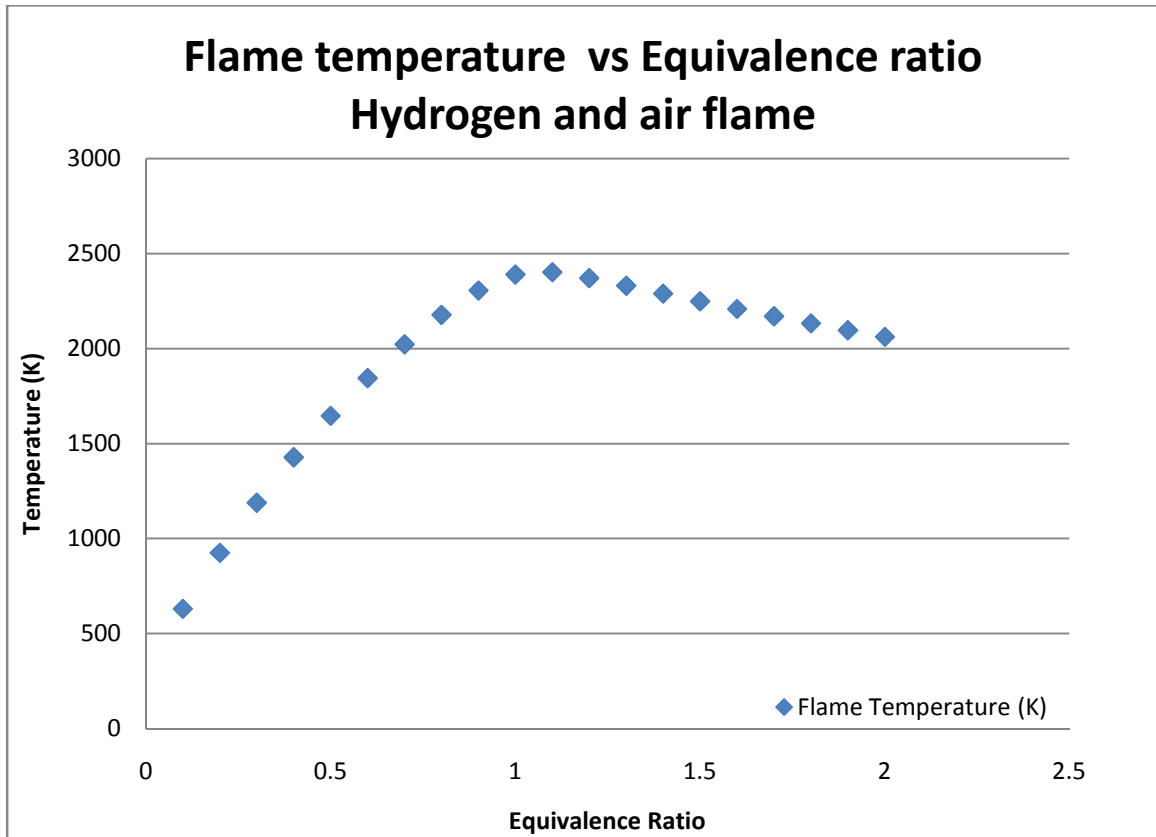
Figure 11. Hydrogen-air adiabatic flame temperature versus equivalence ratio. Graph shows equivalence ratio dependence on the flame temperature of the reactants.

The maximum temperature that a certain type of fuel can produce is termed the adiabatic flame temperature. This temperature is a function primarily of the equivalence ratio of the reactants and is calculated as an enthalpy balance between the product and reactant species. Figure 12 shows typical adiabatic flame temperatures for various fuel and oxidizer combinations.
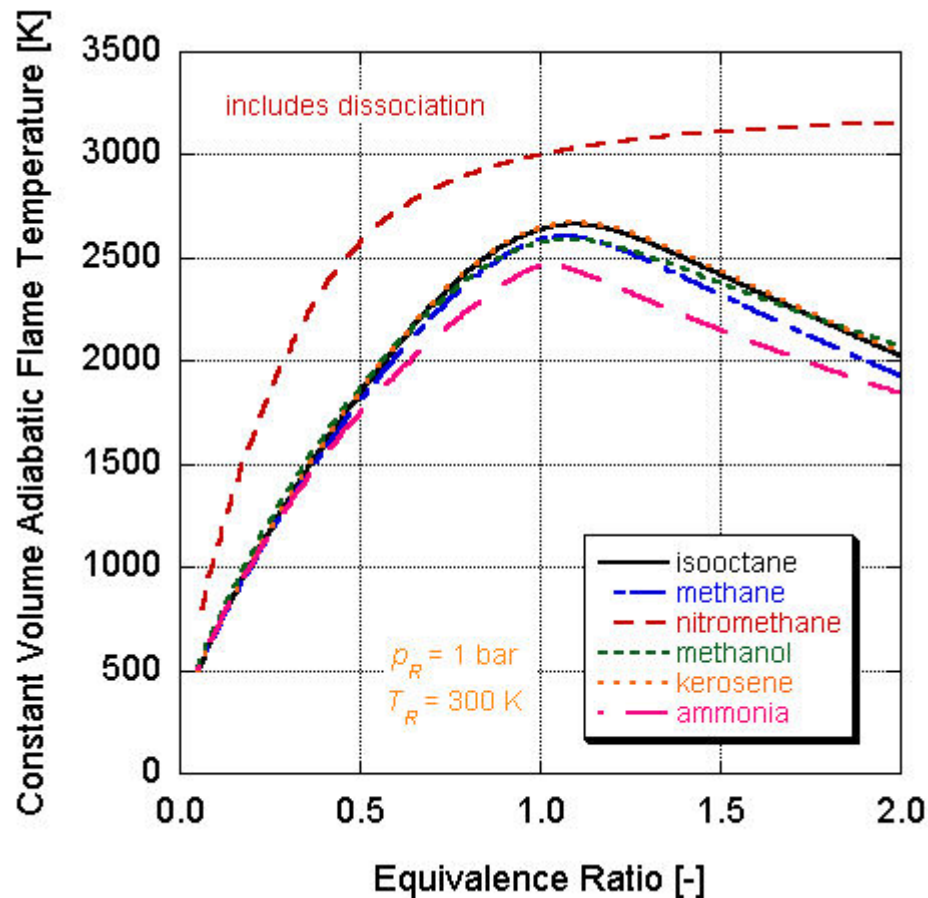
Figure 12. Adiabatic flame temperatures for various reactants. Note peak temperatures at an equivalence ratio of one. Hydrogen-oxygen flame's peak temperature, 3200K, occurs at an equivalence ratio of 1.1 (Depcik, 2006).

To obtain the maximum heat output from the device, it should be operated as close to the adiabatic flame temperature as possible. However, these temperatures are prohibitively high for most combustor materials. To prevent catastrophic failure of the combustor via melting, a limit on the equivalence ratio combined with an estimation of the heat transfer into and out of the combustor is needed. This requires a detailed

analysis of the flame/substrate interaction. This analysis is the topic of the analytic

modeling section.

As indicated by T. Leach, a global analysis assumes the reactants react

completely, creating products at the adiabatic flame temperature of the mixture (Leach &

Cadou, 2004). This assumption indicates that the energy released is directly related to the

combustion enthalpy of the fuel. The combustion enthalpy, or chemical energy in the

reactants, refers to the difference between the reactant and product enthalpies, formulated

in Equation 1. From a simple first law analysis, it follows that the heat-released in the

reaction scales linearly with the reactant mass flow rate and varies in the same manner as

the adiabatic flame temperature with the equivalence ratio. In Equation 1, the "h" values

are the enthalpies of the subscripted quantities, mdot is the mass flow rate of reactants,

phi is the equivalence ratio, q is the heat released per unit mass, and Q is the power

released. These enthalpies are the sum of the individual chemical species enthalpies and

therefore are a function of the equivalence ratio of the reactants.

$$q_{combustion}(\phi) = h_{combustion}(\phi) = h_{products}(\phi) - h_{reactants}(\phi)$$

$$Q_{combustion} = H_{combustion} = \dot{m}\left(h_{products}(\phi) - h_{reactants}(\phi)\right)$$

Equation 1. Heat of combustion. The heat released through combustion is

calculated as the difference between the reactant and product enthalpies. The

formulation is either per unit mass flow rate or a total power output.

Therefore, the best-case performance for a combustion system is if it produced

reaction products at the adiabatic flame temperature. This is not feasible for most

combustor materials, and necessitates creating a model of the heat transfer inside the device to establish workable operating parameters. If the device were sized in accordance with other micro combustion systems however, the maximum available power would be between 3-50 W. This is depicted in Figure 13.
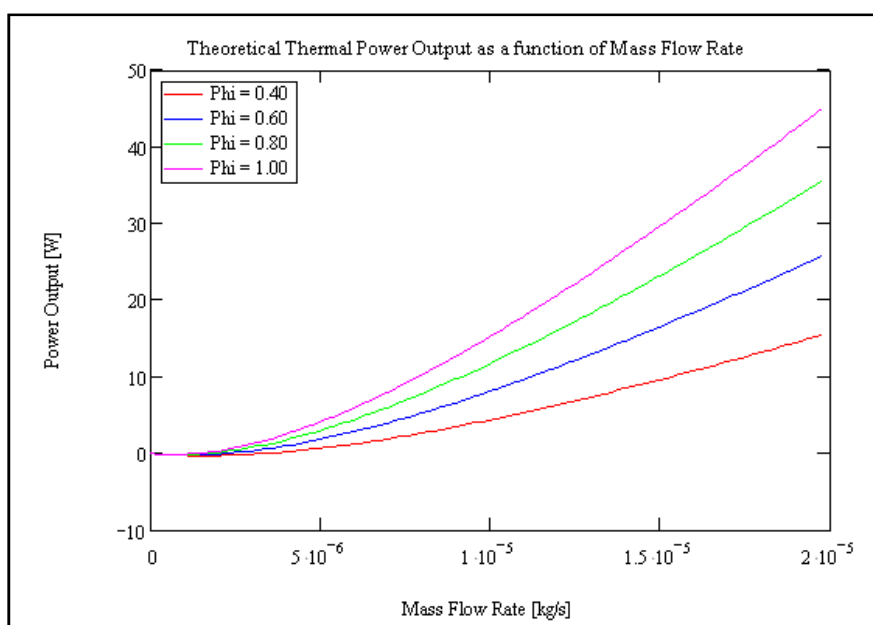
Figure 13. Theoretical power output versus mass flow rate for hydrogen and air reactants. Note increasing power output with increasing equivalence ratio, phi.

Power Conversion

The combustor device is well suited for the remote production of heat and power. Any number of conversion devices such as a mechanical Sterling engine, or thermoelectric generators can harness this energy (Yoshida, et al., 2004). Unfortunately, the power harnessing process is usually the source of the lowest efficiency in the system. Typical Seebeck generation devices operate with efficiencies between 5-10 percent (Flipsen, 2006). While this may seem like a hurdle to the adoption of such a device, the total power output of the gaseous reactants combined with their high energy storage density makes them an attractive option for long duration, constant power applications.

Thermoelectric power generation is the usual means of harnessing the power generated by micro combustion devices (Flipsen, 2006). These generators rely on the Seebeck effect to turn a gradient in temperature into an electrical potential.   The Seebeck effect describes the diffusion of charge carriers between two dissimilar metals. A temperature gradient in the material provides the driving force for this diffusion. When the electrons diffuse through the material, they leave behind positively charged nuclei. The result of a charge gradient in the material due to a temperature difference is the creation of an electric potential between the hot and cold sides of the device. Equilibrium is reached when the thermal diffusion gradient is matched by the electric field gradient. The electric potential that exists between the hot and cold sides allows current to flow, in this case providing the power needed to operate mobile electronic devices. The measure of performance of Seebeck effect generators is the Seebeck coefficient. With units of µV/K, it provides an indication of the materials ability to convert a temperature

differential into and electrical potential. Bismuth telluride, a common TEG base material

has a Seebeck coefficient of -287 µV/K (DiSalvo, 1999).
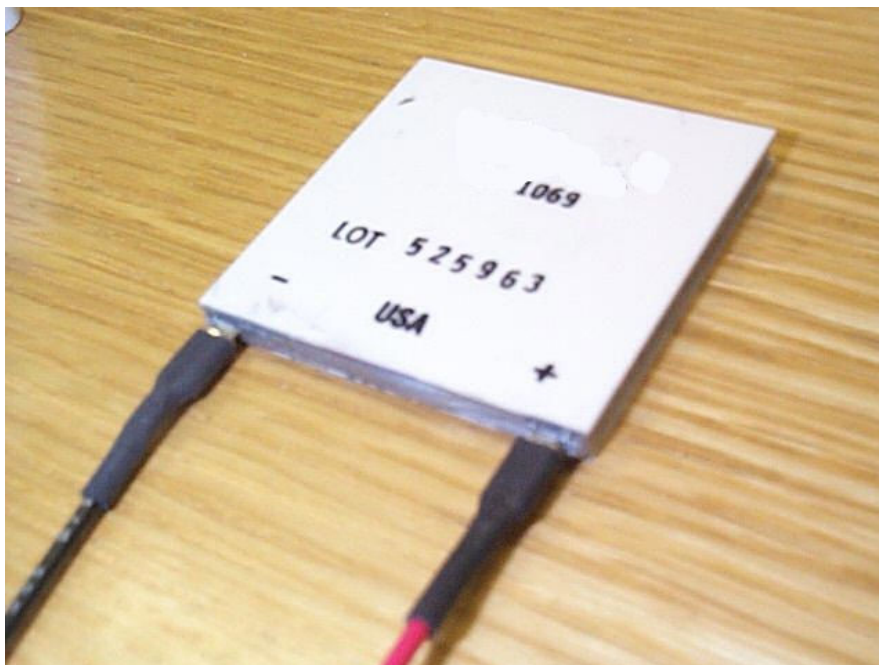
Figure 14. Commercially available thermoelectric generation device, or Peltier

module ("Carl's electronics", 2009).

The effectiveness of the thermoelectric generation devices depends greatly on

their constitutive materials and purities. The current state of the art generation devices

rely on n-p type semiconductors tied to metallic surfaces. These devices have conversion

efficiencies near 5 percent. The efficiency of a thermoelectric generator is defined as the

energy output divided by the energy absorbed at the hot side junction. These devices

have found widespread use in the powering of spacecraft and cooling of integrated

circuits. Figure 14 shows a commercially available thermoelectric generation device.

Long confined to these specialized applications, recent advances in thermoelectric

generators using exotic materials and nano patterning techniques have raised the

efficiency to 20-25 percent (Snyder, 2008). These generation devices are finding
widespread use and are hence becoming less expensive through their adoption by the
automotive industry. Currently, Volkswagen and BMW have integrated TEGs into their
current production model cars, shown in Figure 15. They reportedly supply between 200
and 600W, providing 30 percent of the cars necessary electrical power and between 5 and
10% increase in fuel efficiency (Snyder, 2008).
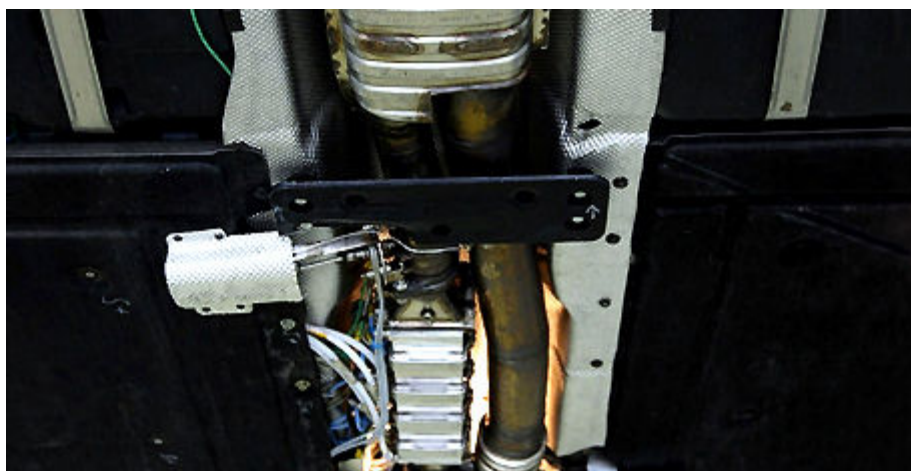
**Figure 15. BMW thermoelectric generators on the new 5-series. TEGs are the five
silver shaped rectangles surrounding the exhaust manifold.**

Heat engines provide an alternate mechanical means for portable power
production. Advances in micro machining technologies have increased the base
efficiency of such engines and make them an attractive alternative to the thermoelectric
generation devices. MIT led the pioneering research into the development of a Brayton
cycle micro turbine capable of producing power from its rotating output shaft. Other
engine types have been explored such as the micro rotary, or Wankle, engine, shown in
Figure 16 (Jiang, Prewett, Ward, Tian, & Yang, 2001). The mechanical power producing
devices are limited in their minimum size, while the TEGs scale easily to any device size.

Each of these devices could be integrated with a single or arrayed LTCC micro

combustion device depending on the power requirements.

The advances in power harnessing technologies make a micro combustion system

a viable alternative to current battery technologies. A specific advantage of the LTCC

system is the ease of integration with any of the aforementioned power producing

components. With micro power generation devices increasing availability, the costs and

performance will continue to improve.
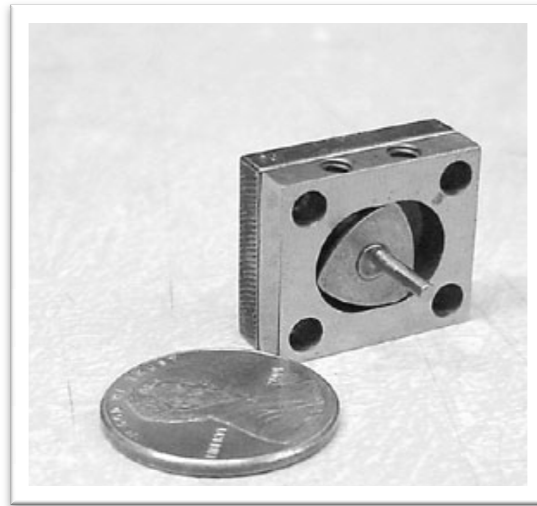
Figure 16. Micro Wankle engine. Fabricated by UC Berkeley (Jiang, Prewett,

Ward, Tian, & Yang, 2001).

Thesis Overview

This thesis will focus on the design, analysis, and experimental testing of an LTCC micro combustor. While the true design process was a highly parallel operation, it has been serialized in this report for clarity. The beginning step in the design process is the identification and clarification of the relevant design parameters, discussed in the next section. This is followed by the generation of a basic concept design that allows for the construction capabilities of the LTCC to be matched to an analytic prediction of the device's performance.

Using the initial concept geometry, an analytic performance analysis of the devices is presented. This analysis allows for the prediction of the operating parameters and flame stability margins for a wide array of future device geometries. The thermal analysis carried out in this section is augmented by a computational investigation in order to determine realistic internal heat transfer properties.

The next detail the design and construction of the testing apparatus. This includes a detailed description of the control software and the auxiliary control and safety hardware. The final section outlines the experimental testing carried out in line with the predictions of the analytic model. The results from this section are compared to the predictions of the analytic model and recommendations for future devices are presented.

Previous Research Efforts

The work of others in the field of micro combustion has primarily focused on the design of catalytic and combustion systems. These devices have taken on a myriad of forms from planar silicon devices to highly three-dimensional sintered metal swiss-roll designs. The wide variety of designs found in the literature is representative of the challenges faced by the designer. These challenges typically center on the tradeoff between the flames stability, and the desire for high power production capability. Several representative designs by others are presented in this section.

Kazushi Yoshida presented work on the design and development of a catalytic combustion power generation device. This device was created using standard silicon MEMS processing techniques. The physical device consisted of a 0.65 mm silicon wafer bonded to two 0.7 mm glass wafers on either side of the silicon. The glass wafers contained thin film ignition heaters and the Pt-TiO$_2$ catalyst. The overall device is 14mm x 10mm x 2mm and had sustained catalytic combustion temperatures between 200 and 400 C using a butane fuel source.
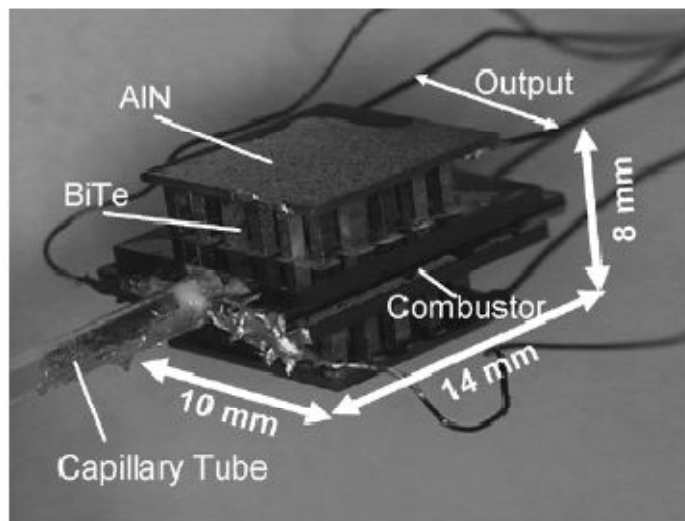
Figure 17. Prototype combustion system designed by Yoshida for the catalytic combustion of butane (Yoshida, et al., 2004).

Kim presented work detailing the development of a small swiss-roll design fabricated using an electrical discharge machining (EDM) process, pictured in Figure 18. This process allowed for channels with 2 mm widths to be cut with a 1.5 mm gap between channels. This machined steel core was capped top and bottom with a 0.6 mm quartz plate. This plate allowed for visualization of the reaction zone and tied into their analytic model of the heat transfer from the device. Using the material properties of the quartz plate, they estimated that a large fraction of the heat transfer from the device occurred through radiation. Using Wein's displacement law, the quartz allowed for a high spectral transmissivity from the reaction zone. This loss was later minimized using refractory blankets over the reaction zone. Ignition of the propane reactants in this device was accomplished in a similar fashion to the research presented in this work, through a spark discharge device. The performance of the combustor was measured using surface thermocouples and a gas chromatograph tied to the exit plane. The information gained

through the gas chromatograph indicated that there was effectively complete combustion of the reactants due to the high overall temperature of the device. The high substrate temperature allowed for pyrolysis of the propane mixture.
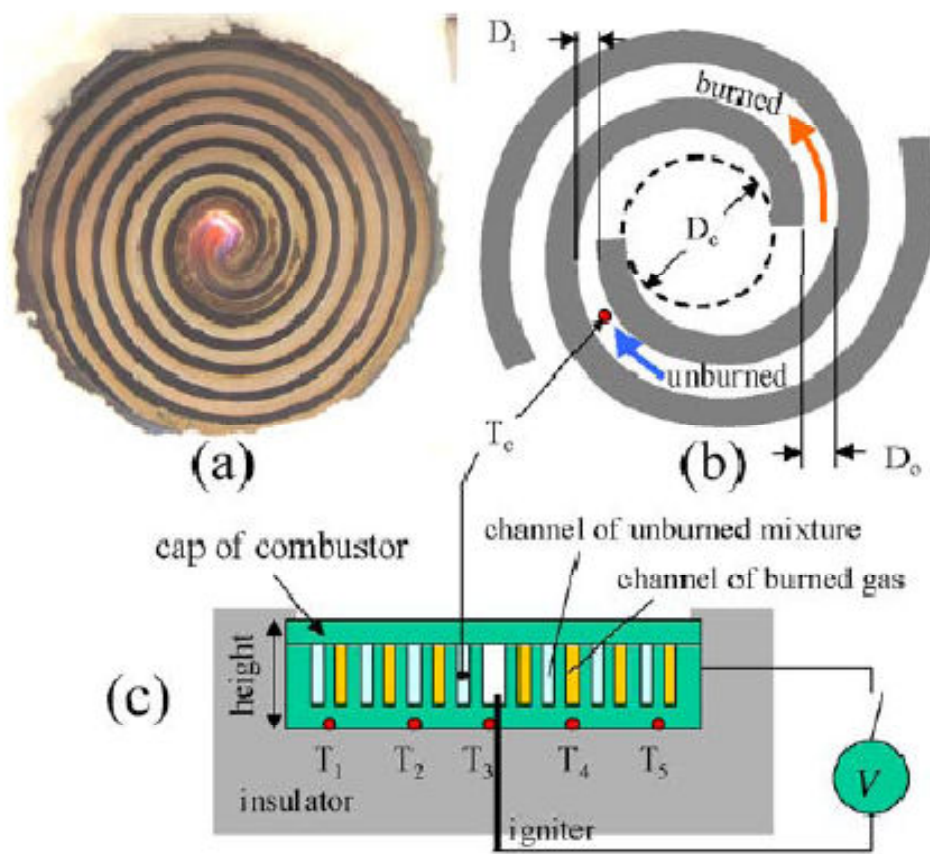
Figure 18. Design of Kim's reactor. Swiss roll is fabricated from steel and capped with quartz plates. Figure(a) is the device in operation with a sustained propane flame in the central combustion chamber .

Vican produced a micro combustion system with a target power capacity of 300mW. In line with Leach's assumption, he used a global combustion model that assumed no dissociation of the products, and hence complete combustion. He later added a combustion efficiency term to account for the real performance of the system. The

modeling presented in his work used a lumped capacitance model based on the assumption of very low Biot numbers. The devices were fabricated using a stereolithography process with an aluminum oxide base material. The substrate contained an embedded platinum catalyst to initiate combustion of the hydrogen-air reactants. The reactants were premixed off chip in an external mixing T, similar in design to the testing apparatus used in this research. Vican validated the complete combustion assumption using an external oxygen sensor. The exhaust products were first passed through an ice bath to cool and condense the water vapor, and the resulting cold gas was routed into a Delta-F oxygen analyzer. This device performed well in both the catalytic mode and the combustion regime (Vican, Gajdeczko, Dryer, Milius, Aksay, & Yetter, 2007). The model and experimental work presented in the design of an LTCC combustor draws heavily on the work of Vican and T. Leach (Leach & Cadou, 2004).
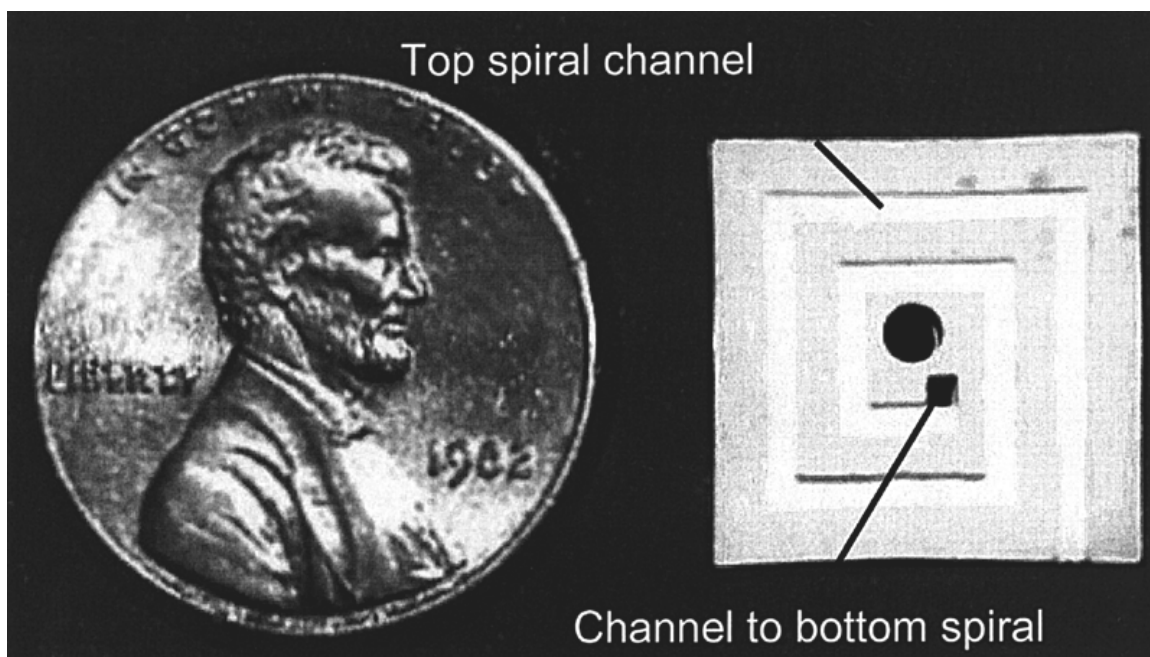
Figure 19. Vican's spiral sintered alumina combustor (Vican, Gajdeczko, Dryer, Milius, Aksay, & Yetter, 2007).

DESIGN INTRODUCTION

The design and fabrication process follows a generational approach, with each subsequent design building on the success and complexity of its predecessor. Each generation contains an iterative design cycle relying on the overall design requirements and an analytic performance prediction. This parallel design process is serialized for clarity in the following sections. The first design objective common to all future designs is the selection of a fuel source and operational parameters. This requires the analysis of the internal and external heat transfer between the reacting gas streams and the solid substrate. The design feedback loop occurs between determining feasible geometries and the required flow rates and equivalence ratios to limit the maximum device temperature to acceptable levels. Before a presentation of the detailed geometries can be given, a brief overview of the relevant flame stability and terminology is required.

Flame Parameters

A brief introduction to the relevant terminology inherent to the design and analysis of a micro combustion system is presented in this section. Along with the terminology, several assumptions regarding the operational conditions of the device, such as pressure effects, are discussed.

Adiabatic Flame Temperature

The maximum temperature that a certain type of fuel can produce is termed the adiabatic flame temperature. This temperature is a function primarily of the equivalence ratio of the reactants and is calculated as an enthalpy balance between the product and reactant species. Figure 12 shows typical adiabatic flame temperatures for various fuel and oxidizer combinations.

Flame Speed

The speed at which a flame propagates is termed the adiabatic flame speed. For instance, if a long tube were filled with a combustible gas mixture ignited on one end, the speed at which the flame moved through the tube would be the adiabatic flame speed for that mix of reactants. By this example, the speed at which the flame moves is a function of the concentration, or equivalence ratio of the reactants in the tube. Instead of letting the flame move upstream into stagnant reactants, most combustion systems feed reactants into a fixed reaction zone. To stabilize the flame inside this zone, the reactants must be fed into the zone at a rate equal to their consumption. Following the above analogy, the reactants must flow through the tube at a speed that just matches the flames speed. This

makes the flame stationary in the laboratory reference frame. Typical laminar flame speeds for hydrogen and air mixtures are shown in **Error! Reference source not found.**.

Adiabatic Flame Temperature vs. Flame speed
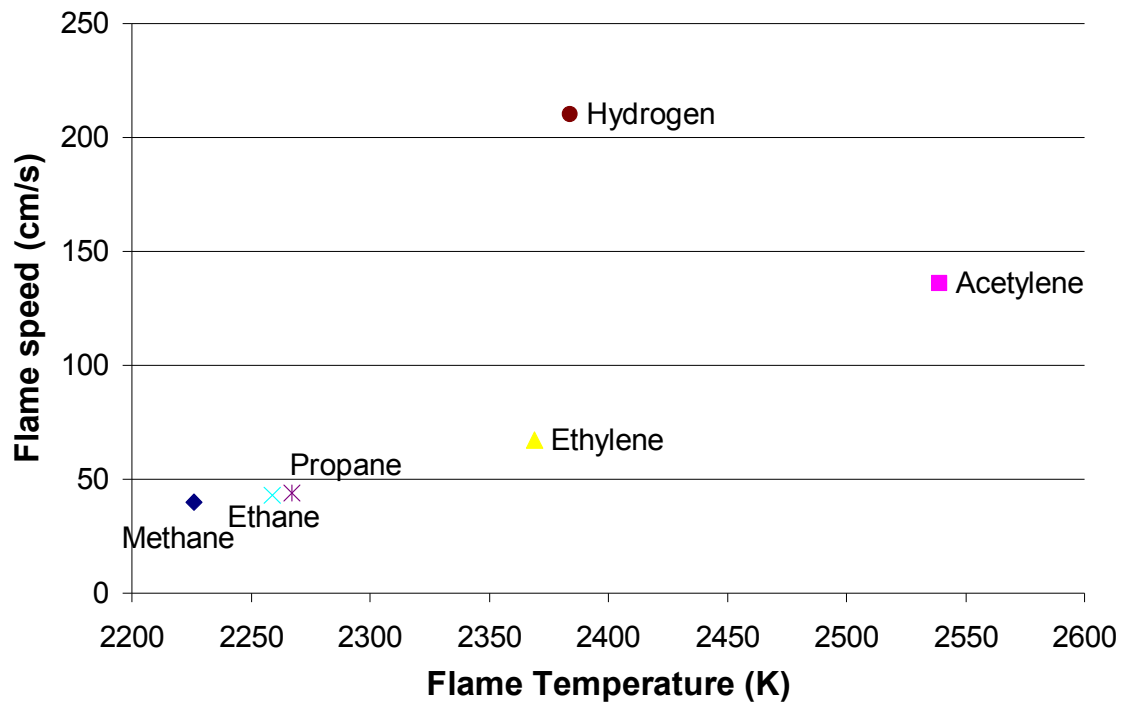
Figure 20. Flame speeds versus flame temperatures for various reactant combinations (Turns, 2006).

Quenching Distance

The minimum channel size through which a chemically reacting flame can propagate is called the minimum quenching distance. This distance is a function of the equivalence ratio of the reactants and the specific type of fuel used. The quenching

distance represents the minimum balance between the heat generated through combustion and the heat lost through conduction into the solid channel surface.

This parameter also represents the largest challenge in designing micro combustion systems. In macro scale combustors, the ratio of the enclosed volume to the wetted surface area is typically much greater than in a micro combustor. This translates to both increased heat loss and heat recirculation in small-scale combustion devices. Heat recirculation refers to heat leaving the device after the flame and reentering the inlet gasses. An effect of recirculation is the broadening of the operating equivalence ratio range and a decrease in the minimum quenching distance (Maruta, et al., 2002) (Leach & Cadou, 2004). Along with the broadened equivalence ratio range, there comes the side effect of a larger sensitivity to the mass flow rate of reactants. If the reactant velocity is too high, the flame will be forced out of the exit plane of the channel and extinguish itself. Conversely, if the mass flow rate is too low, the increased surface area of the channel will remove a large amount of heat than a comparable macro scale burner. This increased heat loss can lead to extinguishing of the flame (Kaisare & Valchos, 2007).

With careful design, it is possible to increase the mass flow rate operating range in small-scale combustors. By tailoring the thermal conductivity of the substrate, the heat transmitted axially through the substrate material can act to stabilize the small-scale flame to instabilities in inlet reactant velocities. This well documented effect is the basis for the analytic model presented in the following sections.

Flame Width

For the purposes of the analytic and numerical model presented in the ensuing

sections, it is assumed that the heat released by the flame is equal to the combustion

enthalpy of the reactants. As reported by T. Leach, this assumption is valid as long as the

flame is operated in the fuel lean condition and the residence time in the channel is

sufficient for complete combustion (Leach & Cadou, 2004). While it is a simple matter

to ensure that the flame is operated in the fuel lean condition, ensuring adequate

residence time requires an estimation of the combustion time constant for the prescribed

fuel and oxidizer combination.   The time constant is estimated using an energy

conservation equation for the reactants and by assuming a linear temperature profile in

the reaction region. The solution to this differential equation is an explicit expression for

the flame width, δ, shown in Equation 2.

$$\delta = \left[\frac{-2\rho\alpha}{(\nu+1)\dot{m}_f}\right]\frac{1}{2}$$

Equation 2. Flame width. Analytic result for the width of a flame propagating in

free air. The derivation of this expression relies on the assumption of a linear

temperature profile across the flame front and no heat loss to the surroundings. ρ

represents the density of the reactants, ν is the viscosity, α the thermal diffusivity,

and m the mass flow rate of reactants (Turns, 2006).

The flame width is expressed in terms of the mass flow rate and inlet gas

parameters. While a reasonable estimate of the gas parameters can be made, the mass

flow rate of the fuel is still an unknown that depends on the total reactant mass flow rate

and its equivalence ratio. The solution of this equation for the particular devices developed in this work is presented in the analytic modeling portion of this report. Historically, the flame widths of hydrogen fueled combustion systems range from 0.5 mm to 1 mm (Turns, 2006) (Leach & Cadou, 2004). Therefore, to meet the requirement for adequate residence time, the combustion chamber should be on the same scale as the flame width, or approximately 1 mm.

Catalytic and Chemical Combustion Systems

The operation of a micro combustion device requires the heat to be released either though a catalytic reaction, or through a combustion reaction. The advantages and disadvantages of each type of device are presented in this section. The result is the selection of a combustion reaction for the power generation in the LTCC micro combustion. This decision guides the design, fabrication, and testing of all subsequent devices presented in this research.

Previous research in the micro combustion field has fallen into two distinct categories, those that catalytically decompose the fuel to provide heat and those that burn the reactants. The choice between a catalytically reactive device and a true combustion device is dependent on the scale size of the physical device. The catalytic devices take advantage of the increasing surface to volume ratio of sub-millimeter channels in order to adequately expose the reactants and ensure complete decomposition. Not only does this reduce the need for an ignition source, but the channel sizes under consideration are typical of the micro fluidic channels created using standard silicon and glass processing techniques. The drawback to such devices is their lack of output power. Their small size,

coupled with the large solid volume of the device has introduced problems with sustained reactions due to the high heat loss. This high heat loss also limits the maximum obtainable temperature of the products and hence reduces the power available from such devices. While the size of the substrate is under the control of the designer, different size devices typically require new tooling for the lamination phase. A supplemental problem is that of catalyst degradation at high reaction zone temperatures. This limit on catalyst performance is at direct odds with the goals of a combustion power generation system and has provided a materials imposed limit to the maximum efficacy of such devices (Tanaka, Yamada, Sugimoto, Li, & Esahi, 2003).

Devices relying on the thermal decomposition of the inlet reactants through a propagating flame structure can overcome many of the shortcomings of their smaller catalytic cousins. However, the nature of containing a flame in an enclosed environment provides different, but equally challenging, materials related problems. By burning the gasses within their flammability regime, the temperature of the exhaust products often exceed the maximum allowable temperatures in most common materials. To combat this problem, the combustion process is carried out in the lean condition, where the excess air or oxygen is used to limit the maximum flame temperature and hence reduce the maximum temperature in the device. Limiting the flame temperature by reducing the equivalence ratio will still provide more heat than the relatively cold catalytic reactions and therefore allow more power to be extracted from the devices.

Vican presented work detailing the design and analysis of a catalytic micro combustion system using hydrogen and air as the reactants. His reports all pointed towards strong catalyst degradation once the test piece neared 300 C. Beyond this point,

the hydrogen and air mixture would enter the auto ignition region, producing exhaust gasses that exceeded the initial catalytic temperature. Once the device underwent auto ignition, the platinum electrodes were oxidized to the point that simply shutting off the reactor and attempting to restart was unsuccessful. Their initial testing required the device to be preheated to 300 C to initiate the surface catalysis. They point to the fact that the power required to initiate combustion is prohibitively high, but could be augmented through a supplemental heat source. Once the device reached 300 C, the combustion reaction was initiated and is described as extremely stable over a wide range of equivalence ratios and mass flow rates (Vican, Gajdeczko, Dryer, Milius, Aksay, & Yetter, 2007). This points towards one of the well documented examples of the benefit of using a catalytically powered micro combustion system. Their stability and reproducibility are unmatched in the strictly combustion powered devices.

Another successful example of a catalytically fueled reactor is the device produced by Sitziki (Sitzki, Borer, Schuster, Ronney, & Wussow, 2001). This device used a reactive propane –air mixture in conjunction with an excess enthalpy, or Swiss-roll design, to produce a device with a greatly broadened flammability regime. He reports a supplemental benefit in that the catalytic devices allow the reaction zone to be confined to a known area, thus eliminating flames location as a variable present in the purely combustion systems. By using a catalytically driven reaction, the fluidic channels were scaled below the minimum quenching distance of the fuel being used. In this case the Sitziki's channels were approximately 2 x 2 mm^2 (Sitzki, Borer, Schuster, Ronney, & Wussow, 2001).

Channel Operating Pressure

An operational assumption regarding the pressure drop in the channel due to the flame is needed. Typically the pressure change can be safely neglected. The ambient pressure in the reaction zone affects the flame speed and thickness differently than an increase in inlet reactant temperature. Theoretically, the flame speed for a reactant mixture should be independent of pressure (Turns, 2006). However, experimental results indicate that higher pressures decrease the burning velocity according to a correlation proposed by (Turns, 2006).

$$S_L \propto C[P_{atm}]^{-0.5}$$

Equation 3. Laminar flame speed pressure dependence. In this expression, C represents a fuel-oxidizer dependent constant, P represents atmospheric pressure, and S is the flame speed (Turns, 2006).

The design of this combustion device presupposes that there is a negligible pressure change across the flame sheet. This assumption is based on the analysis of the Rayleigh lines for a weak deflagration flame. The Rayleigh lines result from the solution of the continuity and momentum equations governing the flow through the device. The solution to this set of equations is a function relating the pressure, velocity, and mass flow rate of the gasses through the channel. These lines provide an upper and lower bound on the flame velocity and pressure change with the limits indicated by their intersection with the Hugoniot curves (Law, 2006).

$$\hat{p}_{\pm} - 1 = -\frac{(1 - M_u^2)\gamma}{\gamma + 1}\left\{1 \pm \left[\frac{2(\gamma^2 - 1)}{\gamma}\frac{M_u^2}{(1 - M_u^2)^2}q_c\right]^{1/2}\right\}$$

$$\left(\hat{p} + \frac{\gamma - 1}{\gamma + 1}\right)\left(\hat{v} - \frac{\gamma - 1}{\gamma + 1}\right) = \frac{4\gamma}{(\gamma + 1)^2} + 2q_c\left(\frac{\gamma - 1}{\gamma + 1}\right)$$

Equation 4. Hugoniot curve equations. Represents pressure drop dependence on reactant mach number. In these equations, γ is the ratio of specific heats, q_c is the heat released through combustion, M is the flame mach number, p is the operational pressure and v is the flame velocity.

The reactant velocities are subsonic in all versions of the combustion devices designed for this study. Therefore, the pressure and density in the post flame region is lower than in the inlet region with a correspondingly higher velocity. The Hugoniot curves intersect the Rayleigh curves in two locations, the first intersection point is referred to as a weak deflagration and the second a strong deflagration. These intersection points occur when the two expressions in Equation 4 are solved simultaneously for the pressure change, p_hat, seen in Figure 21. Deflagrations are flames which propagate slower than the pressure wave and are hence subsonic. However, if a flame exists with a positive heat release and a strong pressure drop, there is only one intersection of the two curves, the strong deflagration. Liepmann and Roshko showed that there is an entropy increase in crossing such a wave, making it a physically impossible for such a solution to exist (Liepmann & Roshko, 2002). Therefore, for the flows under consideration in these devices, a mach number much less than one corresponds to a unity pressure ratio. This indicates that the combustion process is isobaric for these devices.
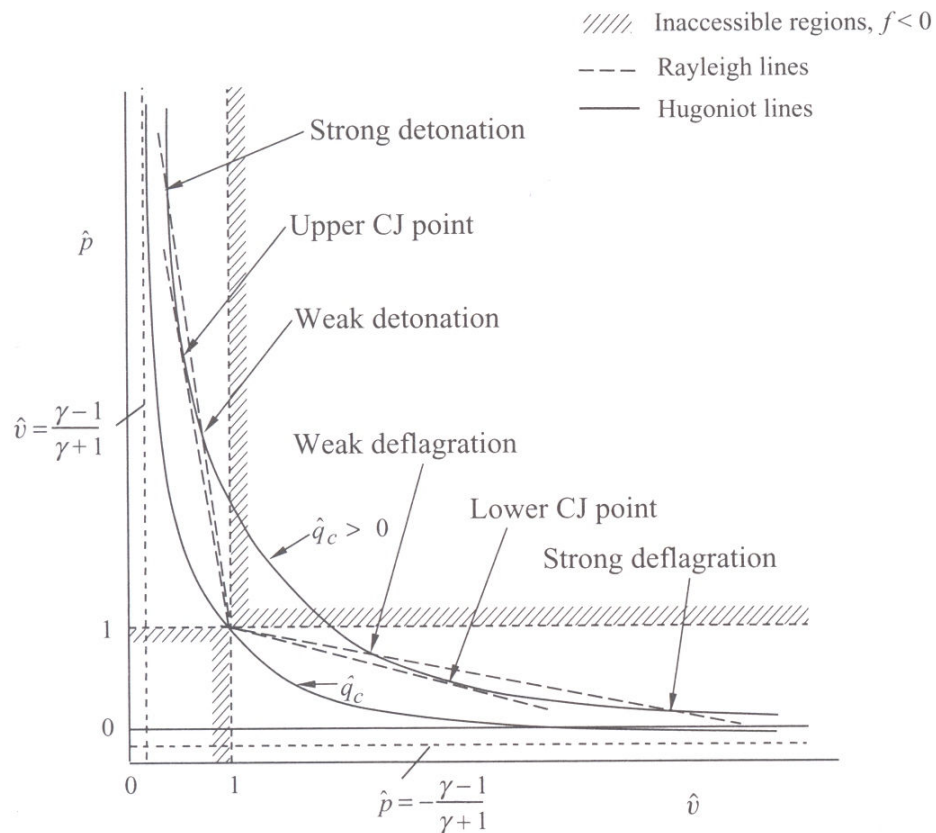
Figure 21. Rayleigh –Hugoniot curves for flame propagation. Analysis indicates that the only favorable solution for a deflagrating flame is the weak case, seen in the above figure (Law, 2006).

<u>Fuels</u>

Various fuels are used in the micro combustion devices presented by others working in the field. The most common fuel sources are the low molecular weight fuels such as hydrogen, methane, butane, and propane. The hydrocarbon fuels exhibit similar burning characteristics such as low flame speeds, and similar flame temperatures. Hydrogen deviates significantly from the trends of the other fuels by exhibiting a much higher maximum flame velocity and a relatively high maximum flame temperature. The flame temperature characteristics are depicted in Figure 12. The main difference between the hydrocarbon fuels used in micro combustion systems is in the flammability limit of the fuel. The flammability limit refers to the maximum and minimum equivalence ratios at which a flame can be sustained. The heavier fuels exhibit higher rich flammability limits, 2.83 for propane versus 1.64 for methane, while the lighter fuels have lower lean flammability limits, approximately 0.4 for methane and 0.5 for propane. The major distinction between them is based on the intended use of the fuel. If the system is designed to run lean, the lower weight fuels are usually preferred over their heavier counterparts. The heavier weight fuels tend to dominate in the non-premixed combustion systems where their increased rich flammability limit increases the flame stabilization region during the mixing process.

Hydrogen is unique when compared to hydrocarbon fuels. It has one of the lowest lean flammability limits of any combustible fuel at an equivalence ratio of 0.14, and a respectably high upper flammability limit at a fuel rich equivalence ratio of 2.54. It also possesses one of the highest adiabatic flame temperatures of 2200 C (Turns, 2006).

The broad flammability region combined with a high variance in flame temperatures over hydrogen's allowable operation range makes it an attractive candidate for a micro combustion fuel source. Meaning, greater control can be obtained over the maximum flame temperature by varying the equivalence ratio with hydrogen than most other fuels. This also correlates to a much larger flame stability region, discussed in the analytic modeling section. Hydrogen has the highest flame speed, ~3.2 m/s, and lowest quenching distance, approximately 0.64 mm, of all the hydrocarbon fuels (Turns, 2006). This allows the micro combustor to be smaller than would be possible with other fuel sources. For these reasons, hydrogen was chosen as the fuel source for the design and analysis of the LTCC micro combustor.

Air functions as the oxidizer source due to its availability, low cost, and lower maximum flame temperature. If the hydrogen were burned in a pure oxygen environment, the maximum flame temperature could reach 3200 C, well above the capabilities of the LTCC material system (Law, 2006). From a practicality standpoint, the need to transport the fuel and oxidizer places a strong limitation on the feasibility of the system. Using standard atmospheric air with approximately 21 percent oxygen posed no additional problems during the experimental investigation.

Design

The generational design of the micro combustors well suits the rapid prototyping capabilities of the LTCC material. The fast design to testing time allowed for rapid iterative improvements in the capabilities of the devices. Over the course of the project, six unique device generations were developed, with multiple devices per generation. This section details the commonalities between the device generations and the starting point for the generation one design. The other generation's unique features are described in detail in the results section.

The geometry of the first generation device was the basis for the analytic model and provided insight into the construction challenges that would be faced with future generation devices. It consists solely of a straight channel with a width and height of 1 mm. The 1 mm feature size of this device represents a 33 percent increase over the minimum allowable feature size of 0.6 mm as dictated by the quenching distance of the fuel source. The reactants enter the device through a porthole in the top of the substrate as a premixed combination of fuel and oxidizer. This eliminates the need to mix the reactants in the substrate and simplifies the fluidic delivery system, requiring only a single inlet.

The flame temperature versus equivalence ratio data for a hydrogen and air flame was used to determine a conservative first estimate of the devices operating parameters. Initially, the equivalence ratio was chosen such that the flame temperature would be lower than the sintering temperature of the LTCC. This corresponds to a fuel lean equivalence ratio of 0.4 and a flame temperature of 750 C. While this functions as a base

operating point, it neglects the actual heat transfer inside the device, which will reduce the predicted substrate and flame temperature. The laminar flame speed for a hydrogen and air flame operating at an equivalence ratio of 0.4 is approximately 1.5 m/s. This corresponds to a total mass flow rate requirement of 2.64×10^{-6} $kg_{reactants}$/s, derived assuming a 1mm^2 channel and gas properties evaluated at standard temperature and pressure.

From the inlet port, the reactants pass through a 0.3 mm feeder channel. This channel moves the start point of the combustion channel outside of the aluminum substrate clamps, increasing the visibility range of the infrared camera. The small feeder channel also functions as an on chip flash back arrester. By being smaller than the quenching distance of the fuel, the increased surface to volume ratio found in the feeder channel will remove more heat from the flame than is necessary to sustain combustion, thus extinguishing the flame. This effect combined with a higher gas velocity in the feeder channel prevents the flame from propagating back to the testing apparatus.

ANALYTIC MODELING

The functionality of the micro combustion system is strongly tied to the equivalence ratio and mass flow rate of the reactants. More importantly, for a micro combustion system, the flammability limits for a flame in the channel is strongly tied to the heat transfer into and out of the micro combustor. This effect is unique to the micro combustion system and presents a challenge to determining operational parameters that will result in a stable system. In micro combustion systems, the flame speed is affected by the increased inlet reactant temperatures, presented quantitatively in Equation 13 (Turns, 2006). To determine the extent to which the flame speed changes, a detailed analysis of the heat transfer inside the device is needed and is the topic of this section. This change in flame speed is presented in the context of determining whether the change in speed corresponds to a stable system in which the flame will remain in the channel when perturbations in the inlet velocity occur.

To determine the feasible operational mass flow rate and equivalence ratio for the micro combustion devices presented in this work, an analytic performance model was created. This model builds on the baseline operational parameters presented in the global analysis to include the heat transfer taking place inside the device.   This complex heat network is crucial to micro combustion devices that rely heavily on the thermal feedback through the device substrate for operational stability. T. Leach and C. Cadou conducted initial work in this area (Leach & Cadou, 2004). They investigated the effect of the substrate's material properties on the flammability limits of a pseudo-infinite parallel

plate micro combustor. Their findings indicated that the thermal feedback from the post flame region to the inlet region is a major contributor to the overall stability of the flame inside the channel.

The model presented in this section builds on their initial suppositions that the substrate is the prime driver of the flame's stability in the channel. This model has been expanded to include the finite three-dimensional geometry and thermal properties of the LTCC micro combustor. The results presented at the end of this section include the substrate temperatures, operational flow rates and equivalence ratios, and the stability margins for the enclosed flame.

Background

For a flame propagating in a device with a low surface to volume ratio, such as a large tube, the effects of the axial heat conduction through the solid on the flame are considered negligible. This assumption is embedded into many of the meso-scale flame models, the oldest being the LeChatlier model (Turns, 2006). In this simplified model of a freely propagating flame, the flame speed is limited by the rate at which the heat released during combustion can conduct upstream through the channel into the incoming reactants. Conduction through the substrate wall is ignored. For most fuel and oxidizer combinations, this results in a flame speed on the order of 10 cm/s (Turns, 2006). The higher diffusivity of the hydrogen and air reactants drive the flame speed much higher, approaching 3 m/s. The negligible wall interaction assumption embedded in the various flame speed models work well for freely propagating flames in large systems; however, the small size of the micro combustor necessitates a closer look at the fluid-wall interaction.

Depicted in Figure 22, the channel sizes considered for the micro combustors of approximately 1-2 mm correspond to a significantly increased surface to volume ratio over the meso-scale combustors with characteristic sizes in the tens of millimeters size range. If the heat transfer properties of the burners were equivalent, the ratio of heat convected into the substrate versus the heat generated in the small burner would be much larger than the equivalent ratio in the meso-scale burner. In fact, this ratio would directly parallel the surface to volume plot in Figure 22. This means that in the small size regime of micro combustors, a larger percentage of the heat generated is transferred to the substrate.
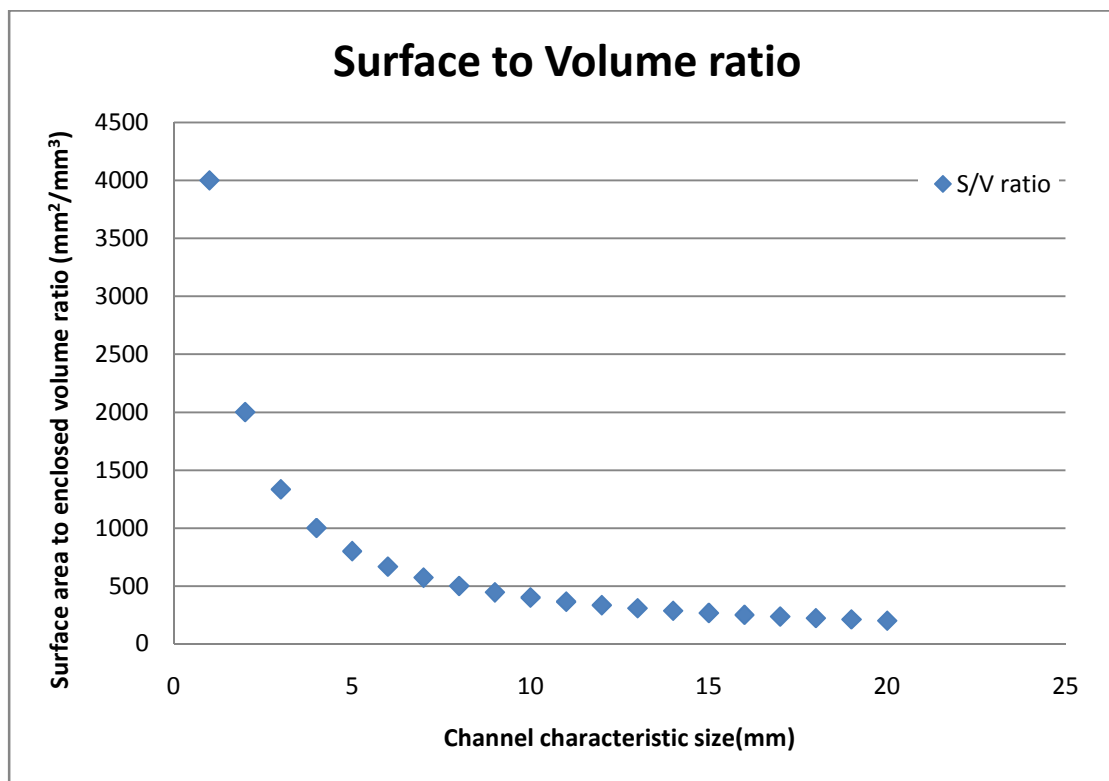
Figure 22. Surface to volume ratio for rectangular channel. Note the size range of the LTCC micro combustor falls in the S/V ratio of approximately 3500 mm^{-1}.

Once the heat has entered the substrate, it can either progress out to the ambient air, or pass back into the inlet region of the device.   The heat leaving the surface of the device represents the available energy for conversion into electrical power. The fraction of heat recirculating to the inlet is not directly usable for power production, but functions to stabilize the flame inside the channel to perturbations in the inlet conditions. This effect is unique to micro-scale combustion devices and is the basis for a large portion of the ongoing research in the field (Sitzki, Borer, Schuster, Ronney, & Wussow, 2001); (Kaisare & Valchos, 2007).

Turns provides an empirical correlation for the effect of increasing the inlet gas temperature on the laminar flame speed. In essence, any increase in inlet gas temperature will have the net effect of increasing the speed of the flame in the channel.

$$S_{laminar} \propto \overline{T}^{0.375} T_b^{\frac{n}{2}} exp\left(\frac{-E_a}{2R_u T_b}\right) P^{-\frac{n}{2}}$$

$$T_b = \frac{T_{adiabatic} + T_{inlet}}{2}$$

Equation 5. Laminar flame speed correlation for increased inlet reactant temperatures (Turns, 2006).

In Equation 5, T_{bar} is the adiabatic flame temperature, T_b refers to the average between the flame temperature and the inlet temperature, R_u is the universal gas constant, n is the reaction order, E_a is the activation energy for the reactants, and P is the combustor's operating pressure. The effect of increasing T_b by increasing the inlet reactant temperature is a positive increase in the speed of the flame.

To hold a flame stationary in space, the reactants must be moving into the flame region at a rate equal to their consumption by the flame. In most meso-scale burners, the flame speed is only a function of the equivalence ratio of the reactants. In the micro scale burners however, the thermal feedback through the device substrate and into the inlet region of the device raises the inlet gas temperature, resulting in an increased flame speed. Adding to the complexity, the amount of heat conducted into the preheat region through the substrate is a strong function of the location of the flame in the channel. This interdependence between the flame location and the flame speed requires an iterative approach to determining a stable operating regime for the device.

Model Setup

The geometry of the channel under consideration is directly analogous to the geometries tested in the experimental section of this project. These devices were comprised of straight channels that varied in length from one to four centimeters with widths of two millimeters. An average length was chosen for the two dimensional model of two centimeters with a two millimeter cross sectional width.   The solid channel walls use multiple layers of the LTCC material and average approximately two millimeters thick. Figure 23 depicts the basic geometry.
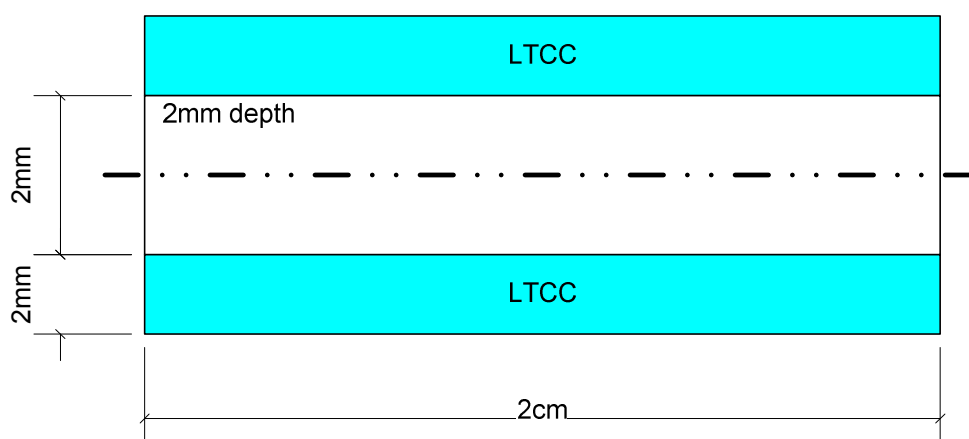
Figure 23. Representative channel geometry. The channel is assumed symmetric about the centerline of the channel.

The analytic heat transfer model of the LTCC device is based on the previous work of T. Leach (Leach & Cadou, 2004). The model centers on an expression for the global energy balance of the proposed device, which includes the enthalpy of the incoming and outgoing reactants and the heat lost to the environment from the surface of the device. The heat transfer in the solid substrate is modeled using a resistive network,

depicted in Figure 25, to define the potential heat paths that affect the stability of the flame in the micro channel. The model inputs include the mass flow rate of the reactants, their equivalence ratio, and the geometry of the channel. T. Leach and C. Cadou's model focused primarily on non-dimensional length and flow rate results that demonstrated the flow physics of micro-combustion devices. However, the model presented in this report is specifically tailored to the fabrication capabilities of the LTCC system. This requires the direct calculation of the mass flow rates and equivalence ratio ranges that will not only provide a stable flame in the combustor, but will result in surface temperature below the critical sintering temperature of the material. Unfortunately, the flow rates cannot be found explicitly and require numerical approximation. The numerical solutions were obtained using the MathCAD software package.

The global energy balance is formulated using a control volume that encompasses the entirety of the device, graphically depicted in Figure 24 and formulated in Equation 6. The global energy balance requires an estimation of the external natural convective heat transfer coefficient for the top and bottom surfaces. The inlet and outlet enthalpy assume constant specific heats of the reactants and products. The specific heat of the gas moving through the channel does exhibit temperature dependence, but for the analytic model, these effects are neglected as the change is slight. To represent the three dimensionality of the device, additional heat loss paths were added in the form of fins. These fins were added to account for the heat spreading observed during the experimental testing phase.
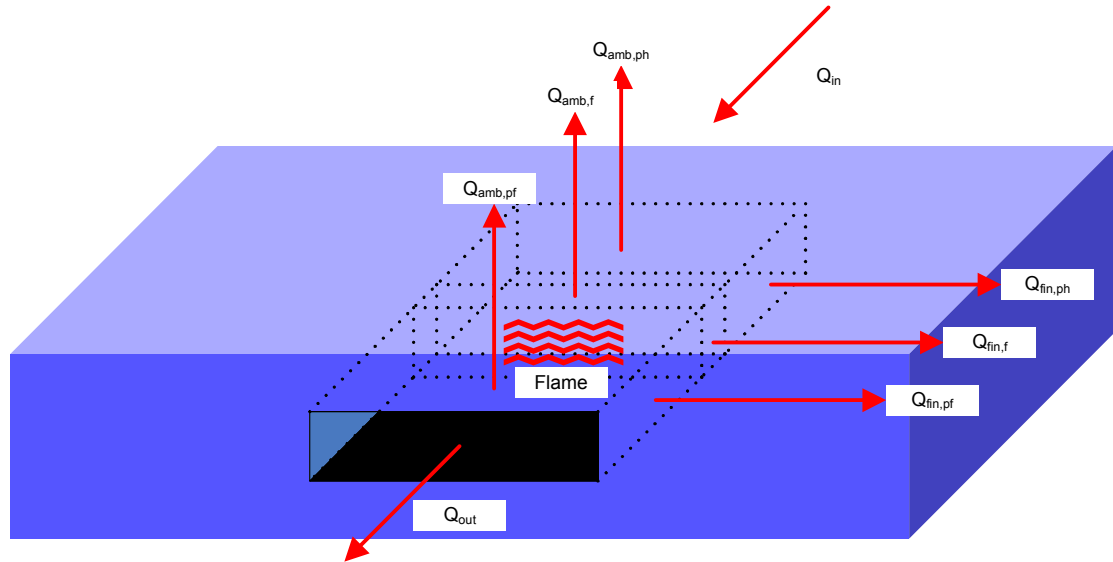
Figure 24. Analytic model heat paths. This figure shows the regions of interest for the analytic model. The three regions enclosed by the dashed lines from top to bottom are the preheat, flame, and post flame regions respectively.

$$Q_{gen} + mC_pT_{inf} = mC_pT_f + Q_{fin_{ph}} + Q_{fin_f} + Q_{fin_{pf}} + Q_{conv_{ph}} + Q_{conv_f} + Q_{conv_{pf}}$$

Equation 6. Global energy balance used in the analytic model. This equation mirrors Figure 24. In this equation, Q represents the power leaving through the subscripted portion of the substrate.

Detailed Model Development

The global energy balance does not identify the specific heat paths inside the device that are critical to its performance. To capture the inner physics of the device in detail, equations relating the internal heat flows are needed. This model of the internal device physics can then be combined with the global analysis, creating a fully defined model of the micro combustor. The equations for the internal heat flows are conservation equations that closely mirror the analysis performed on electrical circuits. In heat transfer, this analysis is dubbed lumped capacitance. The basic premise of using a lumped capacitance analysis is that the resistance to heat flow inside a solid body is much smaller than the external resistance to heat entering or leaving the body through convection, therefore the solid can be treated as a one-dimensional object whose temperature only varies along one axis. The Biot number is the factor by which the validity of the lumped capacitance method is characterized, shown in Equation 7 (Dewitt & Incropera, 1996).

$$Bi = \frac{hl}{k}$$

Equation 7. Biot number equation. The Biot number represents the ratio of the convective heat transfer to the internal conductive heat transfer.

The Biot number physically is the ratio of the external heat transfer coefficient , h, to the thermal conductivity, k, of the solid body. l represents a characteristic length of the solid. To ensure the validity of the lumped capacitance method, the Biot number must be below approximately 0.01. For this device with an assumed external heat transfer

coefficient of 25 W/m^2, a solid thermal conductivity of 3.3 W/m, and a characteristic length of 0.5mm, the Biot number is 0.004. This verifies the applicability of the lumped capacitance analysis to this system (Dewitt & Incropera, 1996).

The internal energy balance assumes the device is in a steady state operating condition, meaning that the temporal variation of temperature in the device is negligible. The solid is assumed axisymmetric about the centerline of the channel, reducing the computational intensity of the system of equations. The development of the internal heat flow equation starts in the flame region of the device where the heat released is assumed proportional to the mass flow rate and equivalence ratio of the reactants. The heat released is determined from the difference in product and reactant enthalpies, shown in Equation 8.

$$Q_{gen} = \dot{m}\left[Y_{O_{2R}}\left(\frac{h_{O_2}}{MW_{O_2}} + \frac{C_{p_{O_2}}}{MW_{O_2}}\Delta T \right) + Y_{N_{2R}}\left(\frac{h_{N_2}}{MW_{N_2}} + \frac{C_{p_{N_2}}}{MW_{N_2}}\Delta T \right) \right.$$
$$+ Y_{H_{2R}}\left(\frac{h_{H_2}}{MW_{H_2}} + \frac{C_{p_{H_2}}}{MW_{H_2}}\Delta T \right) - Y_{O_{2P}}\frac{h_{O_2}}{MW_{O_2}} - Y_{N_{2P}}\frac{h_{N_2}}{MW_{N_2}}$$
$$\left. - Y_{H_2O_P}\frac{h_{H_2O}}{MW_{H_2O}} \right]$$

Equation 8. Combustion power. Power released through combustion of various equivalence ratio combinations of hydrogen and air reactants.

In Equation 8, the h values are the formational enthalpies of the subscripted species, MW is the molecular weight of the species, Y is the mass fraction of the species in the mixture, and C_p is the specific heat of the species. The stoichiometric reaction for hydrogen and air is given by Equation 9. Additional products appear in this equation if

the equivalence ratio is less than unity. Namely, there is excess oxygen in the reactants that appears in the products. The nitrogen in the mixture is a non-reactive species, acting only to absorb some of the heat released during the reaction between the hydrogen and oxygen. In reality the nitrogen does play a part in the overall reaction kinetics, but the Gibbs potential for the formation of water is much stronger than the standard nitrogenated products such as NO.

$$H_2 + \frac{1}{2}O_2 + \frac{3.76}{2}N_2 \Rightarrow H_2O + \frac{3.76}{2}N_2$$
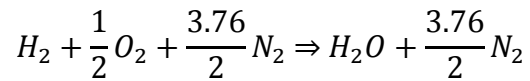
Equation 9. Global stoichiometric chemical reaction for hydrogen and air reactants.

Products change depending on the operating flame regime.

Resistive Heat Transfer Model

The heat generation presented in Equation 12 is the starting point for the analysis of the internal heat transfer in the device. The internal energy balance follows from the application of an energy balance applied to the heat transfer network presented in Figure 25. This resistive network analysis closely mirrors the Kirchhoff laws applied in electrical circuit analysis.
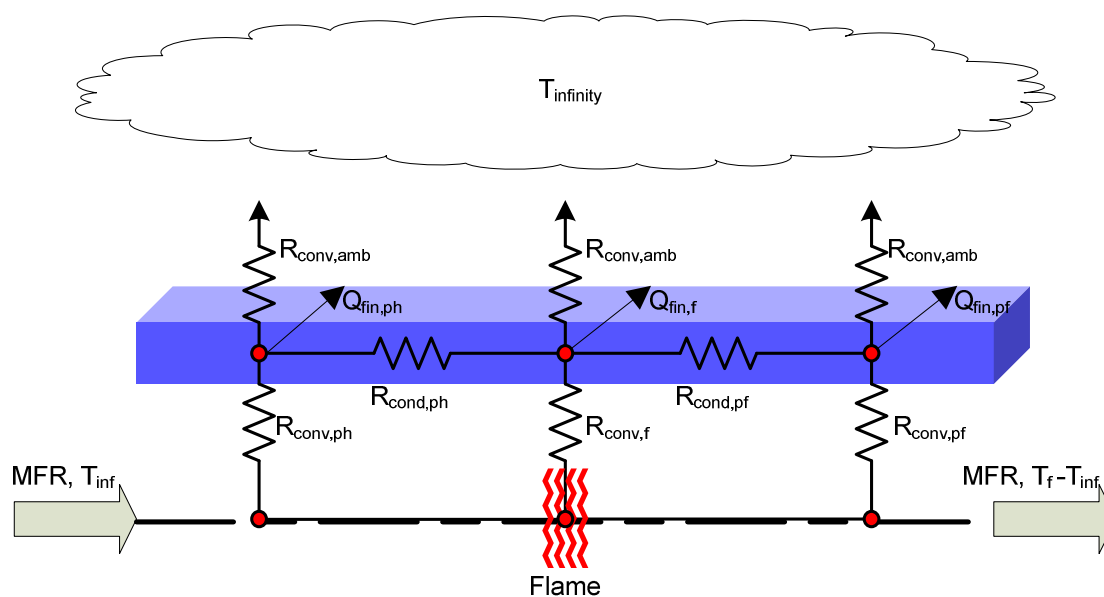
Figure 25. Resistive network modeling the internal heat transfer in the micro combustion device.

In Figure 25, the resistances are tabulated as follows with the specific constants defined in the following sections:

$$R_{conv} = \frac{1}{hA}; \ R_{cond} = \frac{L}{kA}$$

Equation 10. Net resistance to heat flow for convection and conduction. h is the heat transfer coefficient, k is the substrate thermal conductivity, A is the area, L is the characteristic length

The f, ph, and pf designations refer to the location of the resistor. F being flame region, pf is the post flame region, and ph is the preheat region. The area and length scales for the resistances are determined by their specific location in the channel and represent the area normal to the flow of heat. The channel represented by this model is a square channel with a depth equal to the height. Given this geometry, the device is split into nine distinct regions, the three substrate regions immediately above the channel, the three substrate regions flanking the channel and acting as fins, and the three fluidic regions encompassing the reaction zone. The substrate area above the channel is much smaller than the area encompassed by the fins, but is at a higher temperature due to its close proximity to the flame region. In addition, this region provides the majority of the thermal feedback necessary to the stability of the micro combustion system. The fin regions use a base temperature equal to the local nodal channel wall temperature. A fin by its nature represents a thermal device that dissipates heat along its entire surface out to its tip. The tip condition provides the necessary boundary condition to analytically determine the heat flow through the fin. Fins also spread heat from a device in a manner that is consistent with the temperature profiles observed in the experimental testing. The

fin correlation used for this model represents a fin with a convective heat transfer tip condition. This correlation is presented in Equation 11.

$$Q_{fin} = \sqrt{hPkA_c}\left(T_{base} - T_{inf}\right) \frac{\sinh\left(\sqrt{\frac{hP}{kA_c}}L\right) + \left(\frac{\sqrt{h}}{\sqrt{\frac{Pk}{A_c}}L}\right)\cosh\left(\sqrt{\frac{hP}{kA_c}}L\right)}{\cosh\left(\sqrt{\frac{hP}{kA_c}}L\right) + \left(\frac{\sqrt{h}}{\sqrt{\frac{Pk}{A_c}}L}\right)\sinh\left(\sqrt{\frac{hP}{kA_c}}L\right)}$$

Equation 11. Heat transfer through fin with convective tip condition (Dewitt & Incropera, 1996). h is the heat transfer coefficient, P is the perimeter, k is the thermal conductivity, L is the characteristic length, A is the cross sectional area, base refers to the root of the fin, inf is the temperature at infinity.

Equation 12 is the resulting resistive network energy balance for the representative micro combustion device.

$$\frac{Q_{gen}}{2} + \frac{(T_f - T_{inf})}{R_{conv_f} + R_{cond_{ph}} + R_{conv_{ph}}}$$

$$= \frac{(T_f - T_{inf})}{R_{conv_f} + R_{cond_f} + R_{cond_{ph}} + R_{conv_{ph_{amb}}}}$$

$$+ \frac{(T_f - T_{inf})}{R_{conv_f} + R_{cond_f} + R_{conv_{f_{amb}}}}$$

$$+ \frac{(T_f - T_{inf})}{R_{conv_f} + R_{cond_f} + R_{cond_{pf}} + R_{conv_{pf_{amb}}}}$$

$$+ \frac{(T_f - T_{inf})}{R_{conv_{pf}} + R_{cond_{pf}} + R_{conv_{pf_{amb}}}} + Q_{fin_{ph}} + Q_{fin_f} + Q_{fin_{pf}}$$

Equation 12. Internal heat transfer energy balance. Similar to global energy balance but accounts for specific heat paths inside the device. This equation corresponds to Figure 25. R is the resistance model from Equation 10 with the subscripted geometries pictured in Figure 25.

The base temperatures for the fin terms appearing in Equation 11 are evaluated at the mean temperature between the flame and the ambient conditions outside the channel. The ambient air is assumed to be at 20 C and 1 atmosphere. The heat transfer coefficient values such as the external and internal heat transfer coefficients appearing in the above equations are tabulated in appendix B. Equation 6 and Equation 12 form a closed set that is solved numerically using the MathCAD software environment.

The MathCAD solution procedure uses a nonlinear solve block to determine the flame temperature as a function of the three independent variables, the mass flow rate, equivalence ratio, and flame location in the channel. Using these results and any

combination of mass flow rates, equivalence ratios, and flame locations, the resulting

substrate temperatures can be determined. Using this information, two of the

independent parameters, the mass flow rate and equivalence ratio can be limited to values

that do not result in surface temperatures higher than the sintering temperature of the

LTCC. The prime driver of the surface temperature of the device is the equivalence ratio

of the reactants and the internal heat transfer coefficients. From the Figure 26, the

maximum feasible equivalence ratio at the maximum predicted flow rate is

approximately 0.45. This is well above the minimum flammability limit of 0.16 for a

hydrogen and air flame. The restrictions on the mass flow rate come from a detailed

analysis of the flame speed inside the channel, presented in the next section.
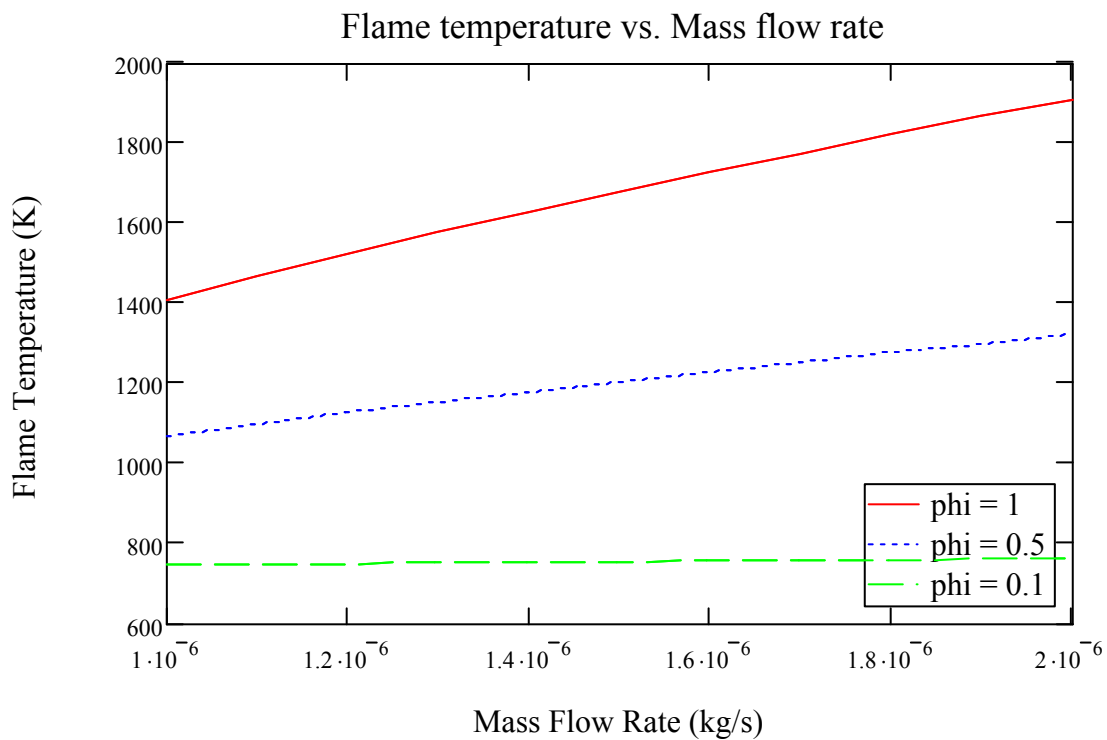
Figure 26. Flame temperature versus mass flow rate at various equivalence ratios. Note, above an equivalence ratio of 0.5, flame temperatures exceed LTCC material capabilities.

Q gen and fin heat fluxes vs Mass flow rate
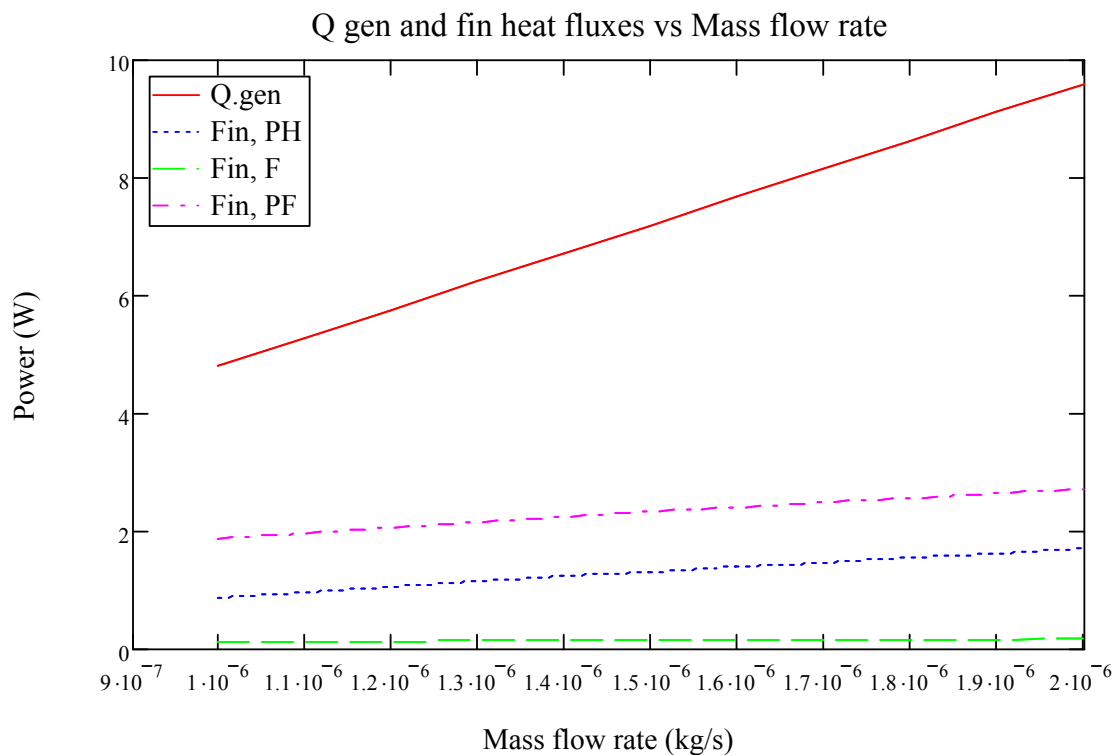
Figure 27. Fin power dissipation versus mass flow rate of reactants at an equivalence ratio of 0.4. Depicts heat transfer through fins at various mass flow rates and a fixed equivalence ratio of 0.45

Figure 27 depicts the power dissipation through the fin surfaces for a range of anticipated mass flow rates. The heat generated by the combustion process is shown as a reference quantity. The above results correspond to the flame fixed halfway between the inlet and outlet planes of the device. As would be expected, the post flame region channel temperature is higher than the preheat region temperature, causing a larger heat flux out of the post flame region fin. The wall temperature immediately adjacent to the flame region fin is significantly higher than the other two regions, but its small area relative to

the other channel regions limits the total heat flow out of the flame region into the flame region fin.
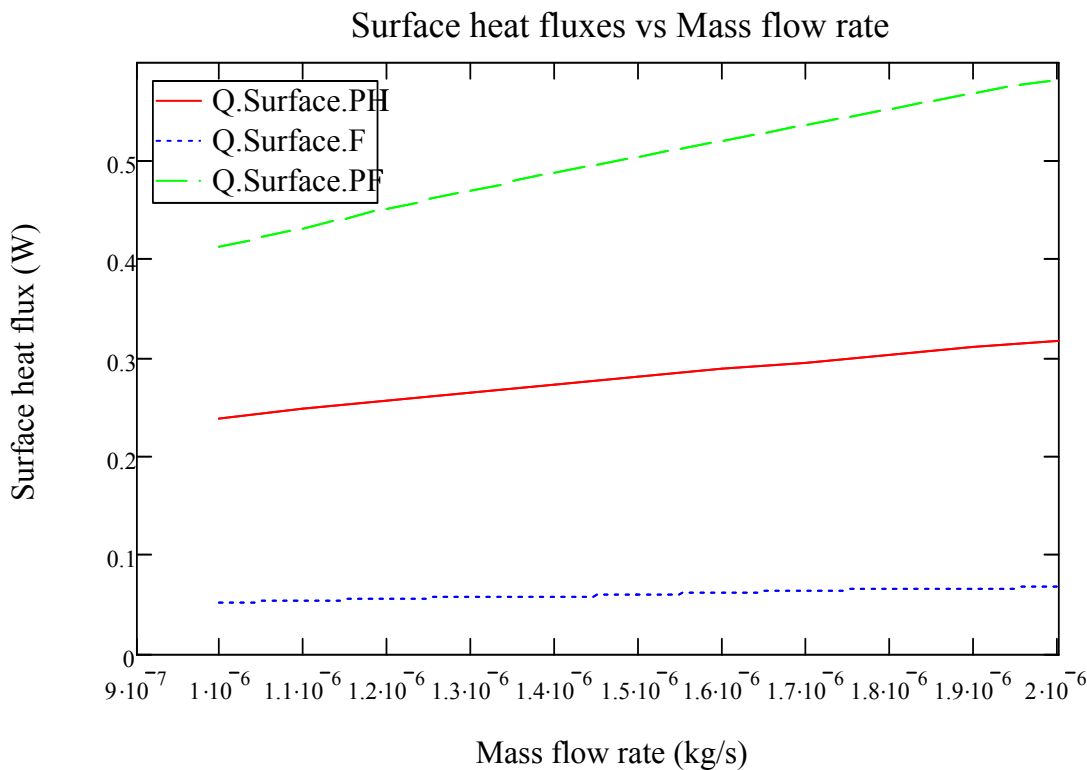
Figure 28. Surface power dissipation in the region immediately above the channel versus the reactant mass flow rate. Note, the post flame region dominates the heat loss from the surface of the device. This region has the highest overall surface temperature.

Figure 28 shows the power output from the region immediately above the channel. As in the fin power dissipation Figure 27, the post flame region represents the largest contributor to the overall power output. However, as in the fin analysis, the temperature of the substrate immediately above the channel represents the highest surface temperature on the device. The low power output from this region is primarily due to the

small surface area. Figure 27 and Figure 28 correspond to different parts of the device with the same operating conditions. These figures indicate that the fins extract the largest amount of heat from the combustion device and should not be neglected in the analysis of a micro combustion system.
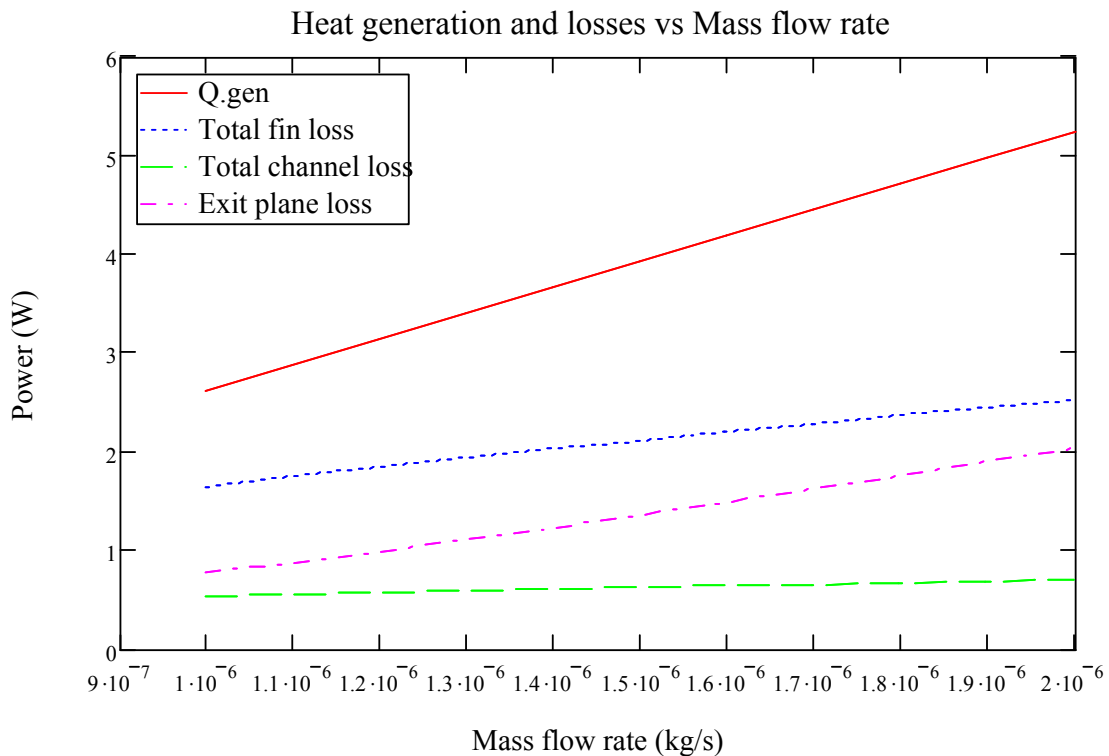
Figure 29. Heat generation and losses vs. Mass flow rate. This figure shows the amount of heat leaving through the substrate. Note large fraction of heat loss is through the exit plane of the device.

Figure 29 shows the heat generation as a function of the mass flow rate and the amount of heat leaving the device through the various loss paths. This figure highlights a major source of heat loss not typically presented in other analytic models, the exit plane loss. This loss represents the power flux of hot product gasses out of the combustion

device and to the ambient air. Given the relative magnitude of this loss, it should not be neglected in the thermal analysis of a micro combustor. This loss is the motivation for the advent of the swiss roll combustor design. Using this design it is possible to capture this wasted heat and pass it through the surface to the power generation device. Regardless, this component of the total heat loss is larger than the fraction passing though the top surface of the device and must be accounted for in the overall energy balance.

This analysis provides a subjective understanding of the relationships between mass flow rate and equivalence ratios as well as the relative magnitudes of the various heat paths being examined. It is clear from this analysis that the out-of-plane effects being modeled as fins are significant components to the thermal energy balance and should be considered in the thermal model. For precise operational parameters, a further analysis must be performed to determine the range of mass flow rates and equivalence ratios that must be used to produce a stable flame. This is presented in the following section.

Stability Analysis

As detailed in the opening paragraphs of this section, the speed of the flame is directly related to the temperature of the incoming reactants. Given the small size of the micro combustor, the heat liberated from the reaction zone and into the substrate can conduct back into the inlet region. This thermal feedback provides an increased reactant temperature and hence increases the flame speed. Through careful design, this effect can positively stabilize the flame in the channel. To account for this effect and design the device to take advantage of it, an analysis of the flame movement in the channel is needed and is the topic of this section. This fundamental stability mechanism present primarily in micro combustion systems allows for a much broader operational range. The next phase of the analytic analysis addresses the increased stability margins of the flame in the channel and allows for the prediction of the associated mass flow rates and equivalence ratios that used in the experimental testing.

Various researchers have measured the speed of a hydrogen-air flame. The diffusive nature of the hydrogen and air flame does not readily lend itself to the standard flame speed analysis used for hydrocarbon fuels. However, the correlation for the increase in flame speed as a function of the inlet temperature of the reactants holds well for most low molecular weight fuels (Turns, 2006). The results of the previous section include a correlation between the flame temperature and the position, mass flow rate, and equivalence ratio of the reactants. Using this information, an iterative solution procedure can determine the mass flow rate or equivalence ratio required to stabilize the flame at any position in the channel.

The flame speed data for hydrogen-air flames was curve fit and used in the MathCAD solution procedure along with the correlation provided by Turns, Equation 5 (Turns, 2006). The result of this curve fit and correlation is an equation for the flame speed as a function of the equivalence ratio and preheated reactant temperature.

$$S_{laminar} = \frac{500\phi^2 + 710\phi - 70}{\bar{T}^{0.375} T_b^{\frac{n}{2}} exp\left(\frac{-E_a}{2R_u T_b}\right) P^{-\frac{n}{2}}} \; ; \; for\; \phi \leq 1$$

Equation 13. Adjusted flame speed calculation for increased inlet gas temperatures.

Equation 13, along with the results of the heat path analysis, are solved for a mass flow rate that results in a stationary flame in the channel. This occurs when the laminar flame speed, adjusted for the effects of heat recirculation, exactly matches the inlet velocity of the reactants in the channel. The results encompass the mass flow rate and equivalence ratio required to stabilize the flame at any position in the channel. These results indicate that if the flame is disturbed from equilibrium by moving it closer to the exit plane, the inlet gas temperature increases due to a larger area for heat to convect into the reactants. This in turn increases the flame velocity and drives it back to its original stability point in the channel. Conversely, if the flame is perturbed towards the inlet of the channel, the reduced inlet temperature will cause the flame to slow down, forcing it back to its original location. This represents a stable system in which the flame can tolerate a ten percent change in inlet gas velocity without being forced into an unstable position. Figure 30 illustrates this effect. This stability margin is directly related to the thermal conductance of the substrate material and indicates that the material is a key contributor to the stability of the overall device. Hence for a high thermal conductivity

device, more heat can be transferred into the inlet region. This increased heat flux can provide a stronger stabilizing effect than a similar device with a lower bulk thermal conductivity.
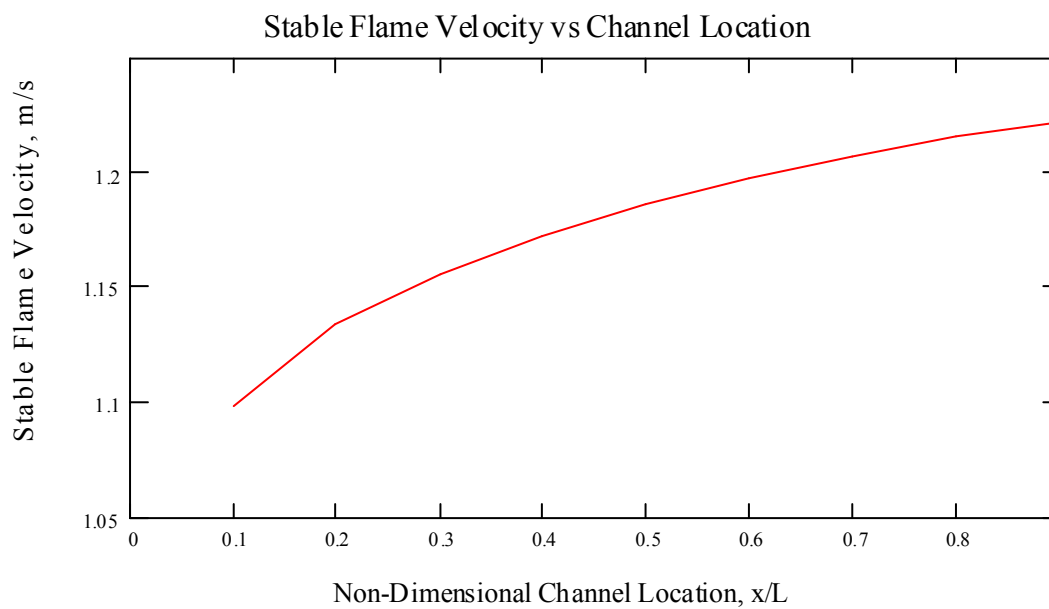
Figure 30. Required inlet reactant velocity for the stabilization of a flame in the channel. Graph is plotted with respect to non-dimensional distance from the inlet.

Figure 31 shows the same stability effect as Figure 30, but is instead formulated in terms of the derivative of the required flame velocity with respect to the channel position. In this case, the positive values correspond to a positive slope of the stable operating velocity graph. Positive values of the derivative indicate that the burning velocity increases as the flame approaches the exit plane, forcing the flame back to its original location. The derivative graph provides further insight into the stability phenomenon by showing the relative magnitude of the stabilizing effect. In Figure 31, a separate plot of a device with a bulk thermal conductivity of 10 W/m-K is shown with an

LTCC device with a thermal conductivity of 3.3 W/m-K. The higher thermal conductivity device has a stronger stability derivative, making the device less sensitive to inlet perturbations. However, this increased thermal conductivity comes at the price of requiring a higher equivalence ratio to overcome the increased heat loss through internal convection. These stability parameters assume that the substrate is isotropic, thereby showing the bulk effects of changing the materials thermal conductivity. This raises the flame temperature and pushes such a device closer to the sintering threshold.
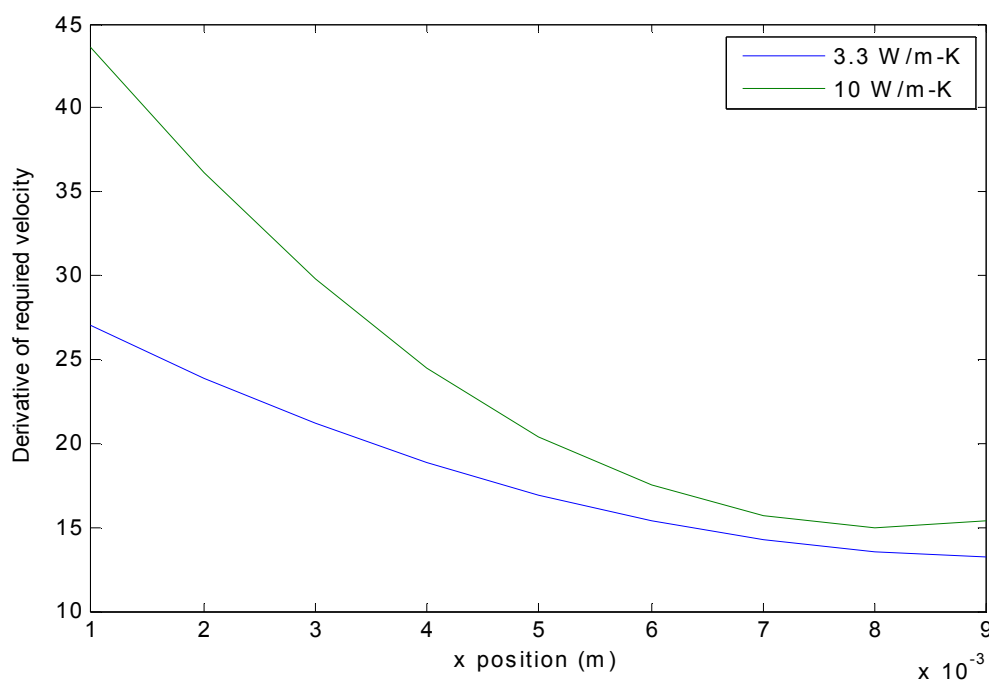
Figure 31. Derivative of required flame speed with respect to distance from inlet. The higher derivative values indicate a stronger stability margin in the channel. In this case, a higher substrate thermal conductivity gives a more stable flame.

The results of the flame stability analysis indicate that a device built to the geometric specifications of the analytic model would require a mass flow rate between $1.2 - 1.9 \times 10^{-6}$ kg/s and an equivalence ratio range of 0.45 to 1.2

Summary of Analytic Models

The analytic model provided insight into the performance and operating parameters of the LTCC micro combustor. These results included a bound on the allowable equivalence ratio operating range and a target mass flow rate to be used in the experimental testing. The stability regime of the flame in the channel proved to be strongly correlated to the heat recirculation capabilities of the device. Hence, it is also strongly correlated to the heat transfer coefficients used to determine the magnitude of the recirculation. Three independent parameters were defined for this analysis, the convective heat transfer coefficient for the inlet, flame, and post flame region. These values were constant, regardless of the flame location in the channel. Due to the sensitivity of the results to the selection of these values, a computational model was created to better determine the coefficients and their variation as the flame moves through the channel. This is the topic of the next section of this report.

NUMERICAL MODEL

The purpose of this investigation into the thermal boundary layer development in a micro combustion device is to understand and quantify the heat circulation through the solid structure. This information allows for a better prediction of the flame stability margins and hence operating parameters of the device. Prior to this analysis, a one-dimensional model of the potential heat paths was used as a first estimate of the operational parameters for the ensuing experimental testing. While this analysis did predict operational parameters that ultimately produced a working device, the methods by which the models input parameters were calculated were based upon a greatly simplified model of the combustion physics. In reality, the solid substrate provides a coupling mechanism between the post flame region and the preheat region which has a dominating effect on the stability of the flame inside the channel. The stability of the flame inside the channel is addressed in the one-dimensional analytic model, but the heat fluxes were estimated assuming a constant surface heat flux and a constant heat transfer coefficients. The assumption of a constant surface heat flux and a fully develop boundary layer implies that there is a linear temperature rise in the reactant temperature as it approaches the flame front and ignores the fact that in reality, heat is also being lost though the solid's top surface to the environment. The external losses reduce the heat flux into the preheat region and thereby reduce the stability of the flame to perturbations in inlet parameters.

These effects were identified during the initial experimental testing phase when the actual stability regime measured in the devices was considerably less broad than predicted by the one-dimensional model. To address these shortcomings, a two-dimensional numerical model of the channel was developed to obtain a better estimate of the heat fluxes inside the device in an effort to improve the calculated stability margins of the device. The geometry for the computational model directly parallels the previous work on the analytic model and is repeated here in Figure 32 for convenience.
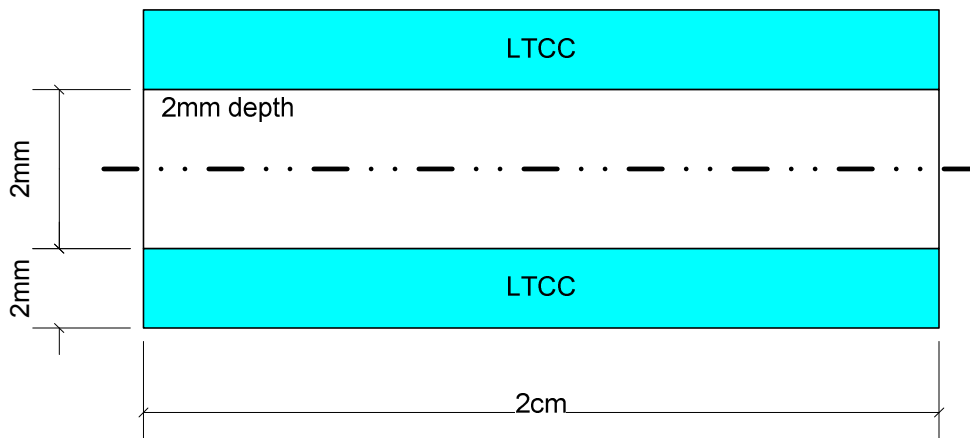
Figure 32. Domain diagram for fluidic and solid body grids

Model

The governing equations for the fluid flow in the channel include the conservative form of the continuity, x and y momentum, and energy equations. The time varying, non-conservative energy equation applies to the solid material. The derivation of these equations is in the appendix and is merely repeated here for clarity.

$$\frac{\partial \rho}{\partial t} + \frac{\partial}{\partial x}(\rho u) + \frac{\partial}{\partial y}(\rho v) = 0$$

Equation 14. Continuity

$$\frac{\partial}{\partial t}(\rho u) + \frac{\partial}{\partial x}(\rho u^2 + p - \tau_{xx}) + \frac{\partial}{\partial y}(\rho uv - \tau_{yx}) = 0$$

Equation 15. X momentum

$$\frac{\partial}{\partial t}(\rho v) + \frac{\partial}{\partial x}(\rho uv - \tau_{yx}) + \frac{\partial}{\partial y}(\rho v^2 + p - \tau_{yy}) = 0$$

Equation 16. Y momentum

$$\frac{\partial}{\partial t}(E_t) + \frac{\partial}{\partial x}[(E_t + p)u + q_x - u\tau_{xx} - v\tau_{xy}] + \frac{\partial}{\partial y}[(E_t + p)v + q_y - u\tau_{yx} - v\tau_{yy}]$$
$$= 0$$

$$where\ E_t = \rho\left(e + \frac{V^2}{2}\right)$$

Equation 17. Energy

$$\tau_{xy} = \tau_{yx} = \mu \left(\frac{\partial u}{\partial y} + \frac{\partial v}{\partial x} \right)$$

Equation 18. Shear stress in x-y direction

$$\tau_{xx} = \lambda (\nabla \cdot V) + 2\mu \frac{\partial u}{\partial x}$$

Equation 19. Shear stress in x-x direction

$$\tau_{yy} = \lambda (\nabla \cdot V) + 2\mu \frac{\partial v}{\partial y}$$

Equation 20. Shear stress in y-y direction

$$q_x = -k \frac{\partial T}{\partial x} \; ; q_y = -k \frac{\partial T}{\partial y}$$

Equation 21. Heat flux in x and y directions

In the above equations, u and v are the x and y components of the velocity, V is the velocity magnitude, k is the thermal conductivity of the gas, μ is the viscosity, del is the vector gradient operator, τ is the shear stress components, λ is the Sutherland viscosity component, q is the heat flux, p is the pressure, ρ is the density of the gas (Pletcher, 1997).

The continuity equation represents the flow of mass into and out of a representative control volume. In the conservative form, it allows for a variation in density to occur as a function of time and the fluids location in the domain. For most simple flows, the density is constant in the domain. But in the case of a combustion model, the local temperatures, and hence densities can change by an order of magnitude

over a small distance. In this model, the inlet gasses enter the device with a temperature of 300 K and increase to a maximum temperature of 1000 K, representing decrease in density of approximately thirty-three percent. In the experimental testing, the devices are controlled via mass flow rate controllers which deliver a precise flow rate of reactants and allow the inlet to be modeled as a constant velocity, constant pressure boundary. Experimental testing and the previous one-dimensional analytic model have shown that the flow through the channel extracts a very small pressure drop of approximately five to ten Pascal.

The continuity, momentum, and energy equations represent four equations and nine unknowns. The closure of this system requires five additional equations:

$$P = \rho R T$$

Equation 22. Ideal gas law

$$e = C_v T$$

Equation 23. Equation of state for calorically perfect gas

$$|V| = \sqrt{u^2 + v^2}$$

Equation 24. Velocity magnitude

$$\mu = \mu_o \left(\frac{T}{T_o}\right)^{3/2} \frac{T_o + 110}{T + 110}$$

Equation 25. Sutherland's approximation for viscosity

$$\mathrm{Pr} = 0.71 = \frac{\mu C_p}{k}$$

Equation 26. Thermal conductivity relation for gas

The first equation is the ideal gas law, which allows for the calculation of the pressure as a function of the density, temperature, and universal gas constant of the reactants. This equation presupposes that the fluid can be modeled as a perfect gas, which for the prescribed temperature and pressure range of this problem is acceptable. The second equation assumes the gas is calorically perfect with constant specific heats. The third equation is the definition of the magnitude of a vector confined to two-dimensional space. The fourth equation is Sutherland's viscosity approximation for a calorically perfect gas evaluated against a reference condition, in this case air at standard sea level temperature and pressure. The final equation assumes a constant Prandtl number for the flow field and allows for the thermal conductivity of the fluid to vary as a function of the changing viscosity. For this specific problem, the Prandtl number is 0.71, corresponding to air at standard conditions (Anderson, 1995).

The domain for this problem includes the solid surface adjacent to the channel. This solid is modeled using the time varying heat equation. This governing equation for the solid is solved independently of the flow field and uses a coupled temperature boundary condition along the channel wall. This boundary condition is outlined in a later section.

$$\frac{\partial T}{\partial t} = \alpha \left[\frac{\partial^2 T}{\partial x^2} + \frac{\partial^2 T}{\partial y^2} \right]$$

Equation 27. Heat equation, where α is the thermal diffusivity of the solid.

MacCormack's Technique

MacCormack's method for solving this set of nine equations is an explicit predictor-corrector technique (Pletcher, 1997). In essence, this method predicts the current flow field variables and uses the predicted values to obtain an updated estimate one time-step into the future. The true value in using this method is that the equations can be solved independently which greatly reduces the computational and programming intensity of the routine. This ease of creation and evaluation is somewhat offset by stringent stability requirements through the careful selection of a time step (Pletcher, 1997).

The continuity, momentum, and energy equations for the flow field are grouped into vectors containing the time and spatial derivatives.

$$\frac{\partial U}{\partial t} = -\frac{\partial E}{\partial x} - \frac{\partial F}{\partial y}$$

$$U = \begin{Bmatrix} \rho \\ \rho u \\ \rho v \\ E_t \end{Bmatrix} ; E = \begin{Bmatrix} \rho u \\ \rho u^2 + p - \tau_{xx} \\ \rho uv - \tau_{yx} \\ (E_t + p)u + q_x - u\tau_{xx} - v\tau_{xy} \end{Bmatrix} ;$$

$$F = \begin{Bmatrix} \rho v \\ \rho uv - \tau_{yx} \\ \rho v^2 + p - \tau_{yy} \\ (E_t + p)v + q_y - u\tau_{yx} - v\tau_{yy} \end{Bmatrix}$$

Equation 28. MacCormack equation vectors

A Taylor expansion allows the advancement of the flow field variables over discrete time intervals.

$$U_{i,j}^{t+\Delta t} = U_{i,j}^{t} + \left(\frac{\partial U}{\partial t}\right)_{av} \Delta t$$

Equation 29. Taylor expansion of U vector

To facilitate the calculation of the new flow field variables, a four-step process is used. The first step is to calculate the components of the E and F vectors with forward spatial differences using the known flow field at time t. The second step predicts the flow field variables at time t+Δt using the Taylor expansion presented in Equation 29. These two steps are combined as follows.

$$\overline{U}_{i,j}^{t+\Delta t} = U_{i,j}^{t} - \frac{\Delta t}{\Delta x}\left(E_{i+1,j}^{t} - E_{i,j}^{t}\right) - \frac{\Delta t}{\Delta y}\left(F_{i+1,j}^{t} - F_{i,j}^{t}\right)$$

Equation 30. Predictor step, MacCormack technique

Rearward spatial differences then correct the predicted flow field values for time t+Δt. The final flow field variables at time t+Δt are obtained using an average of the corrected and predicted values.

$$U_{i,j}^{t+\Delta t} = \frac{1}{2}\left[U_{i,j}^{t} + \overline{U}_{i,j}^{t+\Delta t} - \frac{\Delta t}{\Delta x}\left(E_{i,j}^{t+\Delta t} - E_{i-1,j}^{t+\Delta t}\right) - \frac{\Delta t}{\Delta y}\left(F_{i,j}^{t+\Delta t} - F_{i-1,j}^{t+\Delta t}\right)\right]$$

Equation 31. Corrector step, MacCormack technique

The preceding four steps are repeated until the change in flow field variables is acceptably small, indicating a converged solution. A secondary convergence check ensures that the mass flow rate of gas is equal across the inlet and exit planes of the device. After each step, the primitive variables are decoded from the U vector. Then,

using the ideal gas equation, Sutherland's viscosity model, and the assumption of constant specific heats, the remaining flow field parameters are calculated.

Time Step Calculation

To ensure the stability of the MacCormack algorithm, a limit on the maximum advancement in time is necessary. The proposed stability criteria is known as the Courant-Friedrichs-Lewy (CFL) criterion (Anderson, 1995). This ensures that the maximum time step does not exceed the stability limits of the explicit solution routine. The K term appearing in this equation is the Courant number and represents a user-selected variable to "adjust" the solution speed. Typical Courant numbers used in this simulation were between 0.1 and 0.8 (Anderson, 1995).

$$(\Delta t_{CFL})_{i,j} = minimum\left(K \left[\frac{|u_{i,j}|}{\Delta x} + \frac{|v_{i,j}|}{\Delta y} + a_{i,j}\sqrt{\frac{1}{\Delta x^2} + \frac{1}{\Delta y^2}} + 2v'_{i,j}\left(\frac{1}{\Delta x^2} + \frac{1}{\Delta y^2}\right) \right]^{-1} \right)$$

Equation 32. Courant-Friedrichs-Lewy stability criteria

Initial and Boundary Conditions

The equations modeling the flow physics are first order in time and second order in space. This requires both initial and boundary conditions to begin the simulation. The boundary conditions are broken into four regions, the inlet, wall, outlet, and symmetry regions. These distinct regions are depicted in Figure 33. To reduce the computation time, the flow field is assumed symmetric about the centerline of the flow. This is a common assumption for flows between parallel plates and does not reduce the accuracy of the results appreciably. At the symmetry plane, the derivative of all the primitive variables is assumed to be zero. Using a first-order rearward differentiation scheme, the nodes at the centerline are equal to the nearest neighbor node in the y-direction.

$$\frac{\partial(U,E,F)}{\partial y}\bigg|_{centerline} = 0 \Rightarrow (U,E,F)_{i,j} = (U,E,F)_{i,j-1}$$

Equation 33. Symmetry boundary conditions
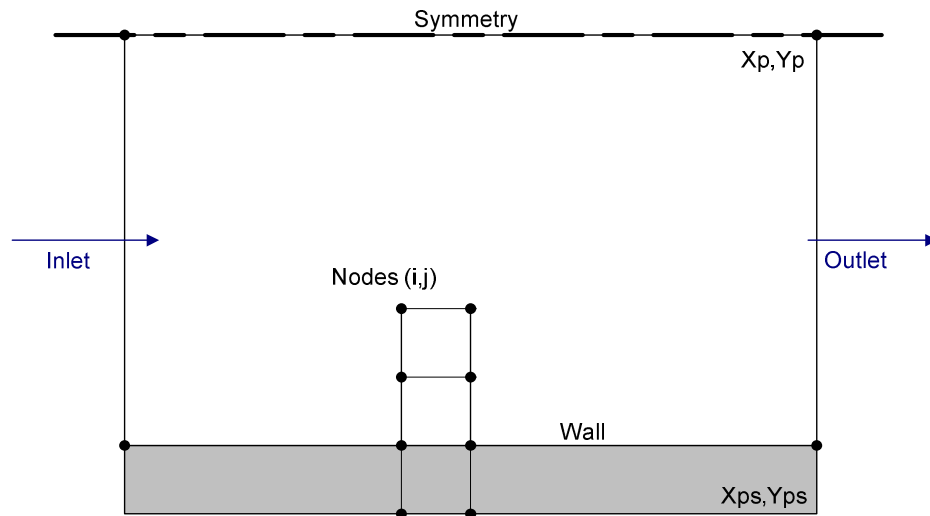
Figure 33. Distinct regions for numerical computations

The inlet conditions include restrictions on the velocity, temperature, and pressure. To match the experimental testing, the total pressure is assumed constant across the inlet of the device. The total pressure of a gas is formulated in terms of the static pressure, inlet Mach number, and the ratio of specific heats. Previous testing in fluent as well as experimental data indicates that the total pressure drop across the channel is approximately 100 Pa. This corresponds to an initial velocity of 1.5 m/s across the channel inlet at 300 K. The total temperature to the preheat region is assumed constant across the test section and equal to 300 K. Finally, the component of velocity in the y-direction assumed zero across the inlet.

$$T_{inlet} = 300K \; ; \; u_{inlet} = 1.5\frac{m}{s}; \; v_{inlet} = 0\frac{m}{s}$$

Equation 34. Inlet boundary conditions

The outlet region boundary conditions are simpler than the inlet conditions in that all flow parameters are extrapolated from the interior region except the pressure. The pressure is averaged across the exit plane between the closest exit node and the assumed free stream exit pressure. This in effect allows the static pressure at the exit plane to float during the computations, but will eventually force convergence at the exit plane static pressure value of 1 atm. This procedure is recommended in the FLUENT help menus and has worked well in stabilizing the computations to pressure fluctuations.

$$outlet_{i,j} = 2outlet_{i-1,j} - outlet_{i-2,j}$$

Equation 35. Extrapolation algorithm

$$P_{i,ymax} = \frac{1}{2}\left[P_{i,j-1} + P_{atm}\right]$$

Equation 36. Exit plane pressure relationship

The velocity component at the wall reflects the no-slip condition, implying that the u and v components are both uniquely zero. The pressure at the wall is extrapolated from the interior. The temperature at the wall is more complicated however. The wall represents the coupling between the solid and fluid regimes and is connected through a matching of the heat fluxes across the boundary. The solution procedure for this coupled boundary uses the current time solution for the flow field and solid to project forward the interface temperature to time t+Δt. This coupling temperature is shown in Equation 37.

$$-k_s\frac{\partial T}{\partial y} = -k_f\frac{\partial T}{\partial y}$$

$$T_{interface}^{t+\Delta t} = \frac{C_sT_s - C_fT_f}{C_s - C_f}$$

Equation 37. Solid-fluid coupling equation

Differencing Scheme

The MacCormack method is second order accurate in space and first order accurate in time. This accuracy is tied to the method in which the governing equations are differenced. To maintain second order spatial accuracy, the U, E, and F vectors are differenced using a first order approximation in the forward direction during the predictor step. However, the E and F vectors contain additional terms with x and y derivatives such as the shear stresses. The derivatives appearing in these terms are differenced in the opposite direction of the governing flow equations. The process is reversed for the corrector step where the U, E, and F vectors are backwards differenced and the shear stress terms are forward differenced. There is an additional level of complexity that must be added to ensure second order accuracy, which concerns the y derivatives appearing in the E vector and the x derivatives appearing in the F vector. These quantities use a central differencing scheme in both the predictor and corrector steps (Anderson, 1995).

$$Central\ difference = \frac{\partial^2 U}{\partial x^2} = \frac{U_{i+1,j} - 2U_{i,j} + U_{i,j}}{\Delta x^2}$$

$$Forward\ difference = \frac{\partial U}{\partial x} = \frac{U_{i+1,j} - U_{i,j}}{\Delta x}$$

$$Rearward\ difference = \frac{\partial U}{\partial x} = \frac{U_{i,j} - U_{i-1,j}}{\Delta x}$$

$$Central\ difference = \frac{\partial U}{\partial x} = \frac{U_{i+1,j} + U_{i-1,j}}{2\Delta x}$$

Equation 38. Differencing schemes for x and y derivatives

Grid Generation

Anderson recommends that the maximum allowable Reynolds number in any one direction define the cell spacing in the domain (Anderson, 1995). These limits are different for the x and y directions due to the larger flow gradients usually occurring in the y direction. For the purposes of this project, the Reynolds limitations are defined as follows

$$Re_{\Delta x} = \frac{\rho V \Delta x}{\mu} \leq 30$$

$$Re_{\Delta y} \frac{\rho V \Delta y}{\mu} \leq 3$$

Equation 39. Reynolds limit for grid generation

With the assumed inlet velocity of 1.5 m/s and a with a density of 1.225 kg/m^3 and a viscosity of 1.85e-5 kg/m-s gives an allowable x spacing of 0.3mm and an allowable y spacing of 0.03mm. With a known domain of 2 cm by 1mm, this translates to a grid size of 66 by 33, rounded in this case to 70 by 40.

Artificial Viscosity

The initial iterations of this code were subject to extreme oscillations in pressure across the domain. These oscillations left unchecked would increase in amplitude and frequency and eventually drive the solution towards divergence. Two methods were investigated to tackle this oscillatory nature of the solution process. The first was a pressure-correction method that attempted to predict the oscillation frequency and cancel the waves by adding or subtracting pressure from the flow field. This method proved to be ineffective through implementation and tuning difficulties. The second method investigated proved successful at damping the oscillatory nature of the pressure field. The damping is achieved using a technique that adds a fictitious energy quantity to the flow field known as artificial viscosity (Pletcher, 1997). In effect, artificial viscosity acts much like real viscosity in that it helps to smooth out the flow field by "smearing" high frequency oscillations. The net effect on the solution was a quick damping of pressure oscillations and much faster convergence. The artificial viscosity terms are pseudo fourth-order terms that approximate the higher order error introduced through the first-order differencing used in the predictor-corrector method. The artificial viscosity terms are formulated in terms of the local pressure gradient and take on large values near rapid changes in flow field pressure. These terms are added to the first order differencing of the U vector during the predictor and corrector phases of the solution process.

$$S_{i,j} = C_x \frac{|P_{i-1,j} - 2P_{i,j} + P_{i+1,j}|}{P_{i-1,j} + 2P_{i,j} + P_{i+1,j}} (U_{i-1,j} - 2U_{i,j} + U_{i+1,j})$$

$$+ C_y \frac{|P_{i,j-1} - 2P_{i,j} + P_{i,j+1}|}{P_{i,j-1} + 2P_{i,j} + P_{i,j+1}} (U_{i,j-1} - 2U_{i,j} + U_{i,j+1}) ; C_x = C_y$$

$$= 0.01 - 0.2$$

Equation 40. Artificial viscosity formulation

The implementation of the artificial viscosity coefficients, C_x and C_y were largely based on experience with failed simulations and required user dynamic tuning to achieve full stability. This consisted of detuning their effectiveness as the simulation progressed. It is hypothesized that the stabilizing nature of the equations can be overridden by round off error when the derivative calculations approach zero. There is little theory behind this adaptive tuning, but the process did provide stable solutions after a much shorter iteration time than without the artificial viscosity terms as seen in Equation 40. Anderson also comments on the use of artificial viscosity as a stabilization mechanism by cautioning the user to be wary of non-physical flow fields that can result through overuse (Anderson, 1995). This is followed by reasonable empirical bounds on C_x and C_y that are considerably larger than the ones used in this simulation.

Figure 36 shows the effect of adding artificial viscosity to the equation set. It also shows that in the steady state case, the pressure drop over the length of the channel is negligible. This further validates the isobaric assumption presented in the design section.
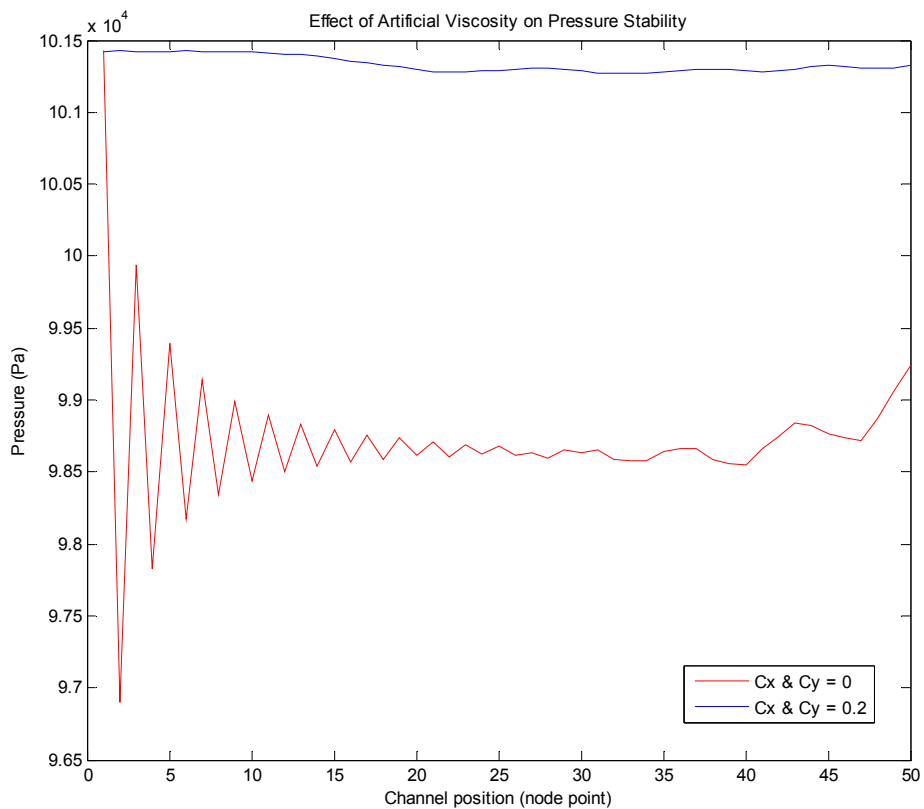
Figure 34. Effect of artificial viscosity on the solution stability. Note increased pressure fluctuations with no artificial viscosity. These numerical instabilities can lead to a divergent solution.

Numerical Simulation Results

The simulation presented in this section corresponds to the initial and boundary conditions presented in the previous sections. This simulation took 120,000 iterations to converge based on the inlet and outlet mass flow rates. The allowable residual error in the mass flow rate was set to 10^{-3}. The first set of graphs represents the condition where the flame is locked in the middle of the channel.
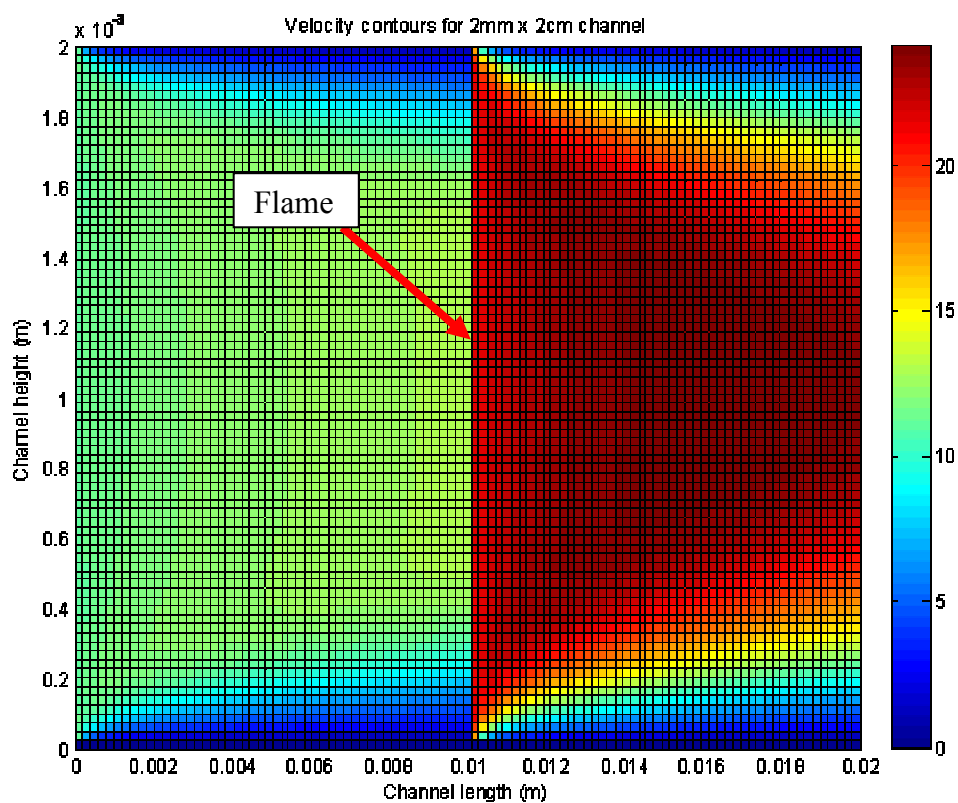
Figure 35. Velocity contours for 2mm x 2cm channel. Note two distinct momentum boundary layers, the first occurs before the flame and the second immediately after the flame front. Velocity contours in m/s

As depicted in Figure 35, two distinct momentum boundary layers develop in the pre and post flame regions.   This is due primarily to the rapid change in temperature and hence density that occurs across the flame width. This graph is somewhat deceiving in its dimensions in that the actual flow field is ten times longer than it is wide. For clarity, the flow field graphs are presented as being stretched in the vertical direction for better flow visualization.
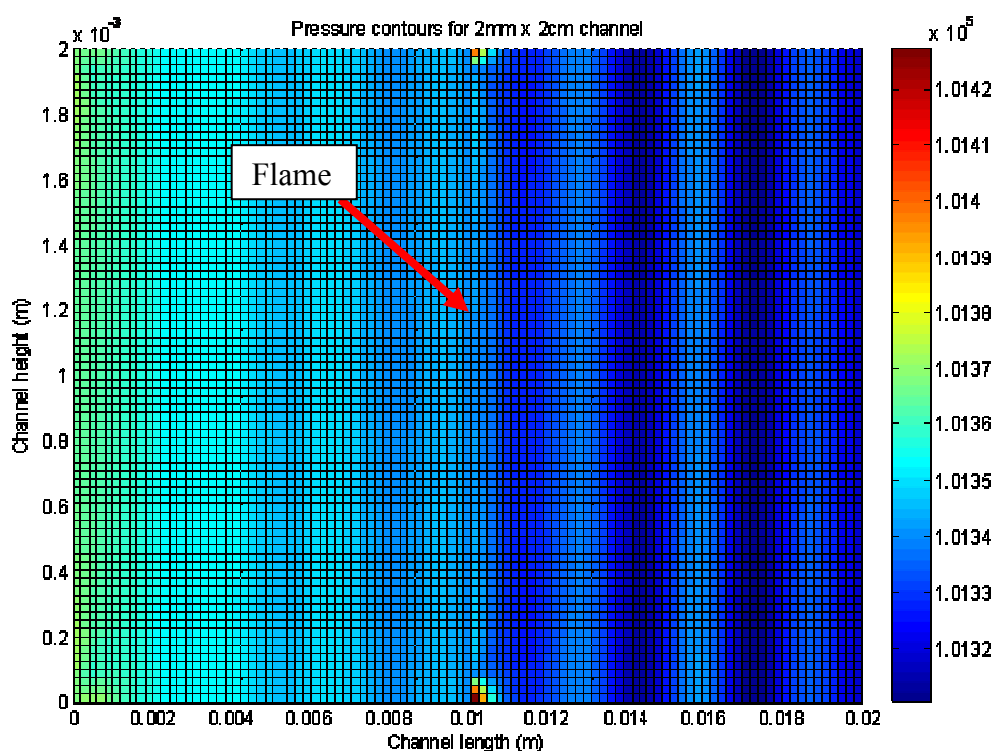
Figure 36. Pressure contours. Note pressure fluctuation magnitudes are very small and do not influence the energy or momentum equations. Pressure contours in Pa.

Though the solution converged, there were still significant pressure oscillations in the flow field. While these can be easily seen in the pressure surfaces, Figure 36 , the

oscillations do not appear in the velocity or temperature plots. Initially the artificial

viscosity helped to damp these oscillations, but as the solution progressed, the oscillation

magnitude and frequency reached a steady state value and did not significantly influence

the other primitive variables.
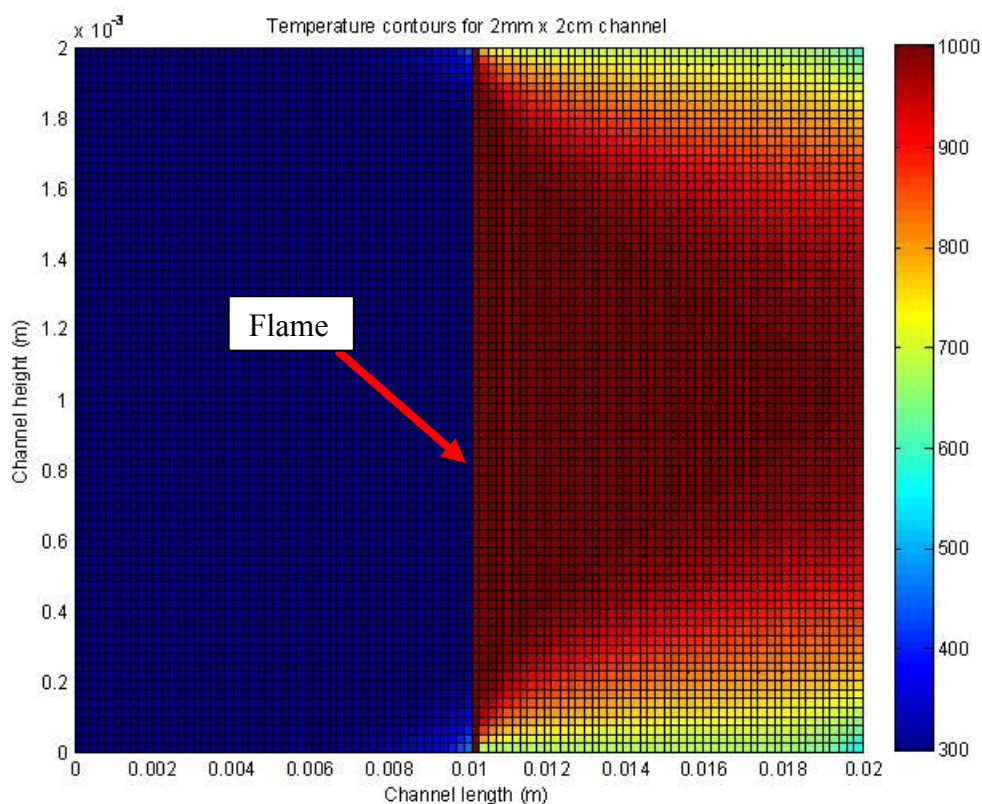
Figure 37. Temperature contours for 2mm x 2cm channel. Note two distinct

thermal boundary layers. Temperature profiles in Celsius.

The temperature contours in Figure 37 show the presence of two distinct thermal

boundary layers. The boundary layer in the post flame region is at a significantly higher

temperature than the pre flame region and hence washes out the temperature profile. This

graph is directly analogous to results seen during the initial Fluent feasibility

investigations. Namely, there is very little to no diffusion of heat in the axial flow direction. In the one-dimensional analytic model, this heat path was added as it is the main stabilization mechanism for flames in the standard macro scale LeChatlier model. Accounting for this potential heat path greatly increased the complexity of the model. According to the numerical simulations, this heat path does not significantly influence the upstream temperatures and was therefore removed.
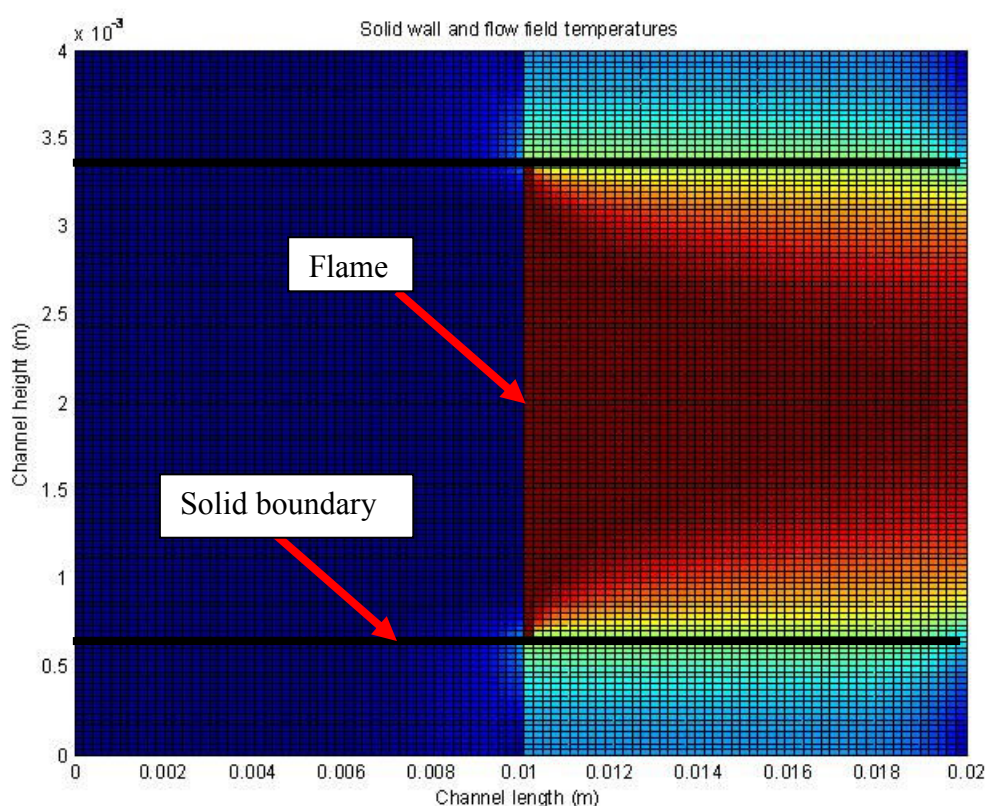
Figure 38. Conjugate heat transfer temperature plot. Note thermal feedback to preheat region through the solid material. Temperature contours in Celsius.

The heat flow into and out of the solid surface is modeled according to Equation 41. This equation represents the heat gradient in the solid material and is calculated per

unit depth. The majority of the heat entering the solid leaves through the external surface

which is modeled in this case using a natural convection boundary condition along the

outer edge of the solid.

$$q' = -k_s \frac{\partial T}{\partial y}\Big|_w$$

Equation 41. Heat flow into solid
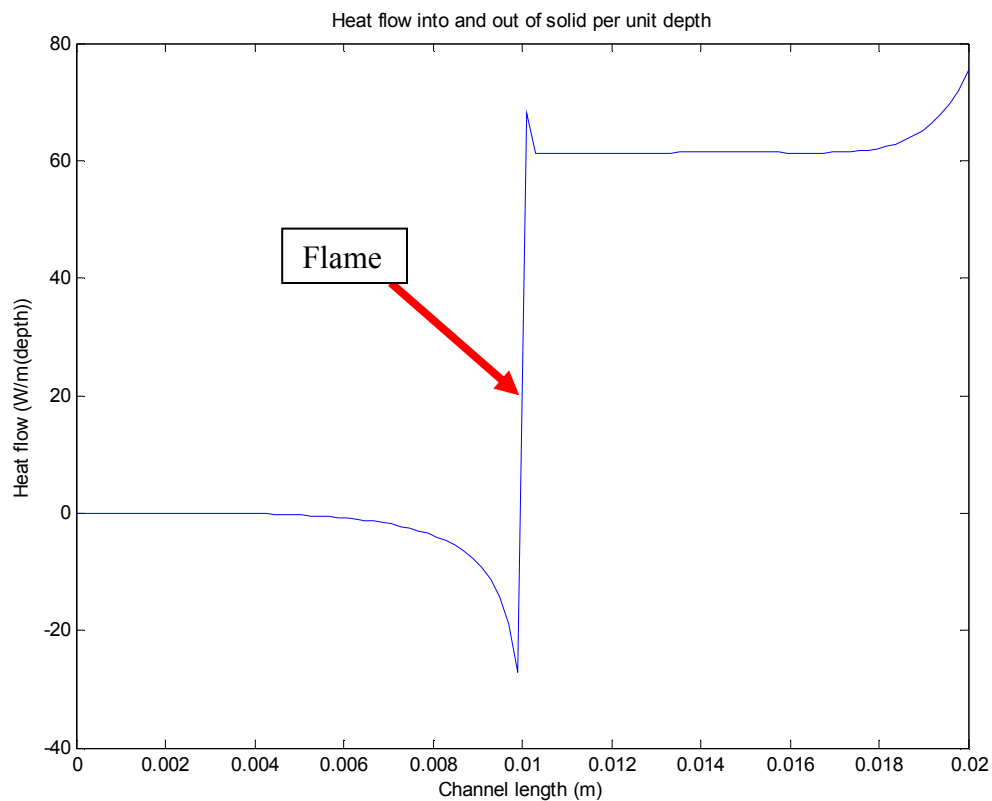
Figure 39. Heat flux into and out of solid wall boundary. Positive values represent heat flow into the solid and negative values represent heat flow out of the solid and back into the channel. The sharp line in the center of the graph corresponds to the location of the flame.

Figure 39 represents the total heat flux into and out of the wall per unit depth. Immediately after the flame front, occurring at approximately 0.01m, the heat moves into the solid material. Directly ahead of the flame, the negative heat flux represents the transfer of heat from the solid to the reactants. This heat transfer raises the temperature of the inlet gasses and is the cause of the increase in flame speed modeled by Equation 13.
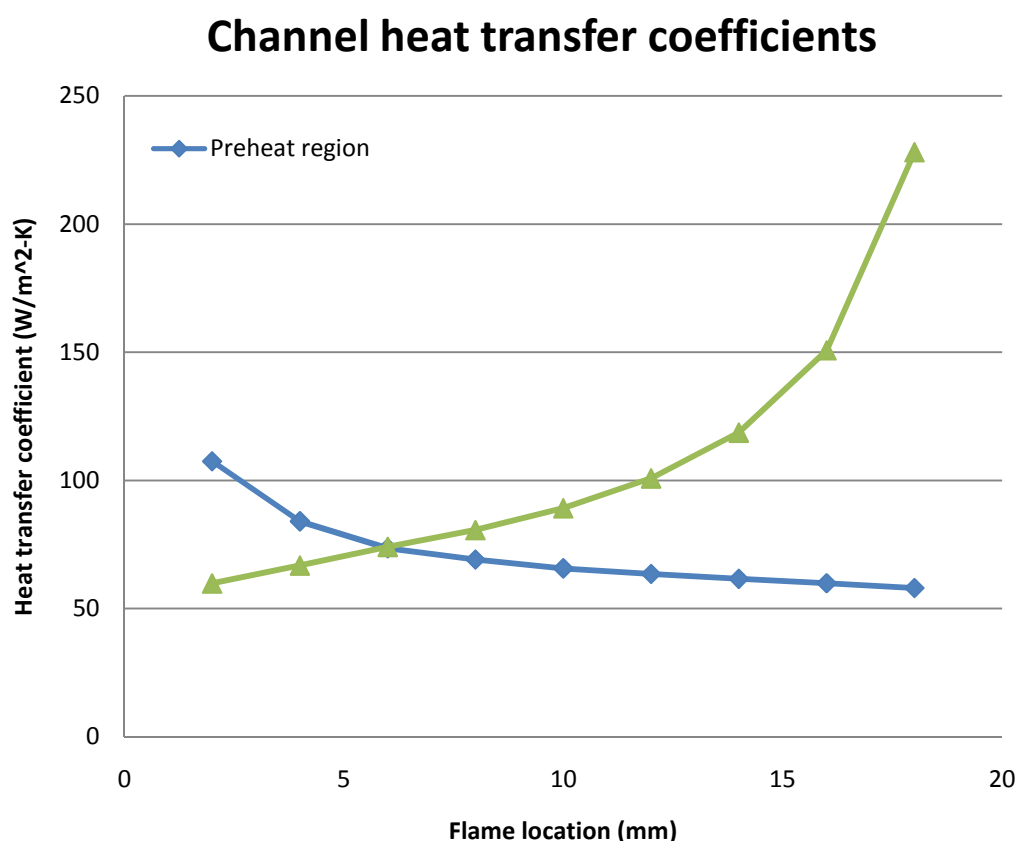
Figure 40. Heat transfer coefficients for preheat and post flame regions

The average heat transfer coefficients for the preheat and post flame regions are presented in Figure 40. These averages refer to the total surface average of the associated region. Therefore as the flame moves towards the exit, the area over which the heat

transfer coefficient is averaged for the preheat region increases, in this case, reducing the average coefficient value. This figure shows the effects of the reformulation of the thermal boundary layer immediately after the flame. The heat transfer coefficients in the flame region are an order of magnitude greater than either the post flame or preheat coefficient values. A fourth order polynomial equation was fit to each of the curves in

Figure 40 and used in the analytic model in place of the constant heat transfer coefficient values. Figure 41 shows the effect of adding in the variable heat transfer coefficients to the predicted flame temperatures.
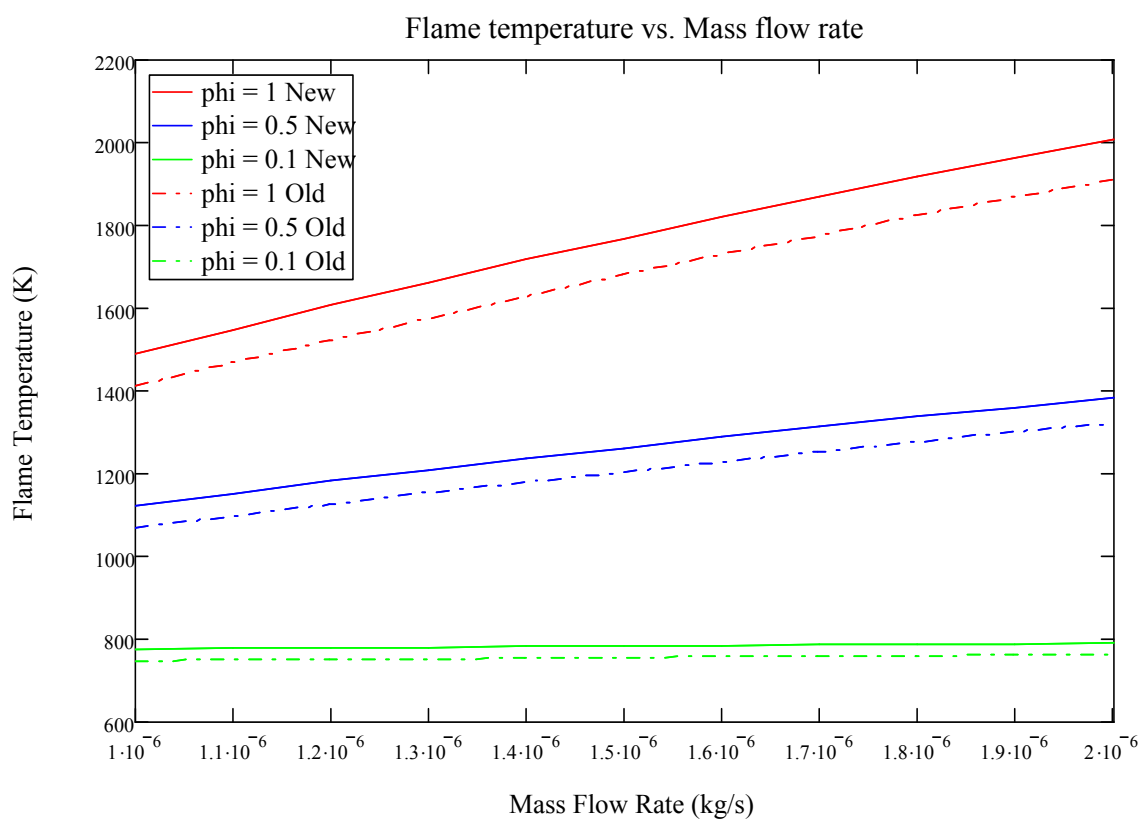
Figure 41. Variable heat transfer coefficients impact on the maximum flame temperature. Note an increase in flame temperatures for all equivalence ratios.

The effect of adding the variable heat transfer coefficients is an increase in the flames stability in the channel. This information provides a better estimate of the performance of the device. The updated model allowed for a rapid prediction of the operational parameters of differing size devices. The next step is to use this information in the design and experimental testing of a functioning LTCC device.

DEVICE CONSTRUCTION AND EXPERIMENTAL TESTING

Using the baseline performance indications provided by the analytic model and the chosen geometry presented in the design section, several test channels were produced. Several different methods were used to produce these channels by slight additions to the aforementioned construction process. The first generation channels were produced by inserting carbon tape as a sacrificial support for the upper channel walls. Omitting the carbon tape led to problems not only with channel sagging, but with cracking in the ceiling of the device. A potential reasoning for the cracking in the channels is the differential sintering of the material in the ceiling structure. A test of this hypothesis was carried out by decreasing the temperature ramp rate of the furnace during the sintering phase. This helped to eliminate the strong temperature gradients in the material, thus causing uneven sintering and shrinking. However, it was noted that the increased sintering time created an increased amount of sagging in the channel wall.

Another potential cause of the cracking witnessed in the early generation devices is stress introduced into the ceiling/wall interface during the lamination phase. Several devices showed signs of early stage cracking after they were removed from the hot press. During the high pressure lamination, the base layers were supported and allowed to fuse, while the unsupported ceiling material was forced into the channel cavity. This produced a stress gradient at the interface between the channel walls and the ceiling material, and allowed micro cracks to develop. Sacrificial carbon tape was used as a stopgap measure to help with cracking and sagging. The carbon sheets were processed using the same

tools and methods as the LTCC material. The LASER is the preferred method for rapid prototyping as the sheets of carbon are the same thickness as the LTCC layers. This allows the carbon to be cut at the same time as the LTCC. However, the addition of the sacrificial layers to the construction process greatly increases the time required to produce a finished device. There have been other methods proposed by (Jurkow & Golonka, 2008) to decrease the time commitment. These include using a rotating bit mill to machine a full size carbon plug instead of stacking individual sheets, and the proposed use of an organic liquid to fill the channel. One researcher reported success in using honey as a sacrificial material (Jurkow & Golonka, 2008).

While these processes involving sacrificial materials were being investigated, another construction method was tried with great success. This involved constructing the device in three distinct pieces, and using a low-pressure lamination to bind them. By separating the devices into a three regions, the high stress channel/ceiling interfaces were eliminated, reducing the formation of cracks in the device. The low pressure lamination requires the use of Poly-2-ethyl-2-oxazoline, or PEOX as a binding agent between the three layers (Plumlee, 2007). This process effectively solved the cracking problem that plagued the first generation devices, while requiring a significantly shorter production time than the sacrificial carbon channels. In summary, the construction process for generation 2 and later devices followed these basic steps:

1. LASER milling of the individual sheets.

2. Collation and alignment of the three individual device regions.

3. Individual high pressure lamination of the three device regions.

4. Alignment of the fused layers, forming the completed device.

5.   Low pressure PEOX lamination of the completed device.

6.   Firing, using a slow ramp cycle.

Experimental Testing

The experimental testing apparatus was designed to mirror the control variables described in the analytic modeling section. These are the mass flow rate, and equivalence ratio of the reactants. The micro combustors are premixed combustion devices, therefore, the mixing of the reactants takes place externally in a mixing tee. The mixed reactants are then passed through an interfacing flange and into the LTCC device. There, the combustion is initialized using an embedded spark electrode device. The exhaust products pass out the exit plane of the device and over a thermocouple, providing the exhaust temperature and a correlation parameter to the analytic model. The surface temperature was measured using an infrared camera and surface thermocouples. The entire system was controlled via a LabView interface and data acquisition module (DAQ board).

Testing Stand

The testing stand, depicted in Figure 42, was designed to provide easy visual access to the top surface of the micro combustion device for infrared visual imaging. To facilitate this need, the mass flow rate controllers were placed on the immediate left and right of the LTCC holder. The mass flow rate controllers were purchased from Parker and are specifically calibrated for the hydrogen and air at the flow rates predicted by the analytic model. Adjusted for standard conditions, the hydrogen mass flow controller is capable of delivering 0-20 SCCM with an inlet pressure of 10 psi. This corresponds to a device with a maximum channel cross sectional area of 4 mm at an equivalence ratio of 1.5, well above the operational window for the designed devices. The air mass flow rate controller mirrors the hydrogen and is capable of providing 0-1 SLPM with a 10 psi inlet pressure. The mass flow rate controllers contain built in proportional-integral-derivative (PID) controllers and require only a mass flow rate set point for operation.
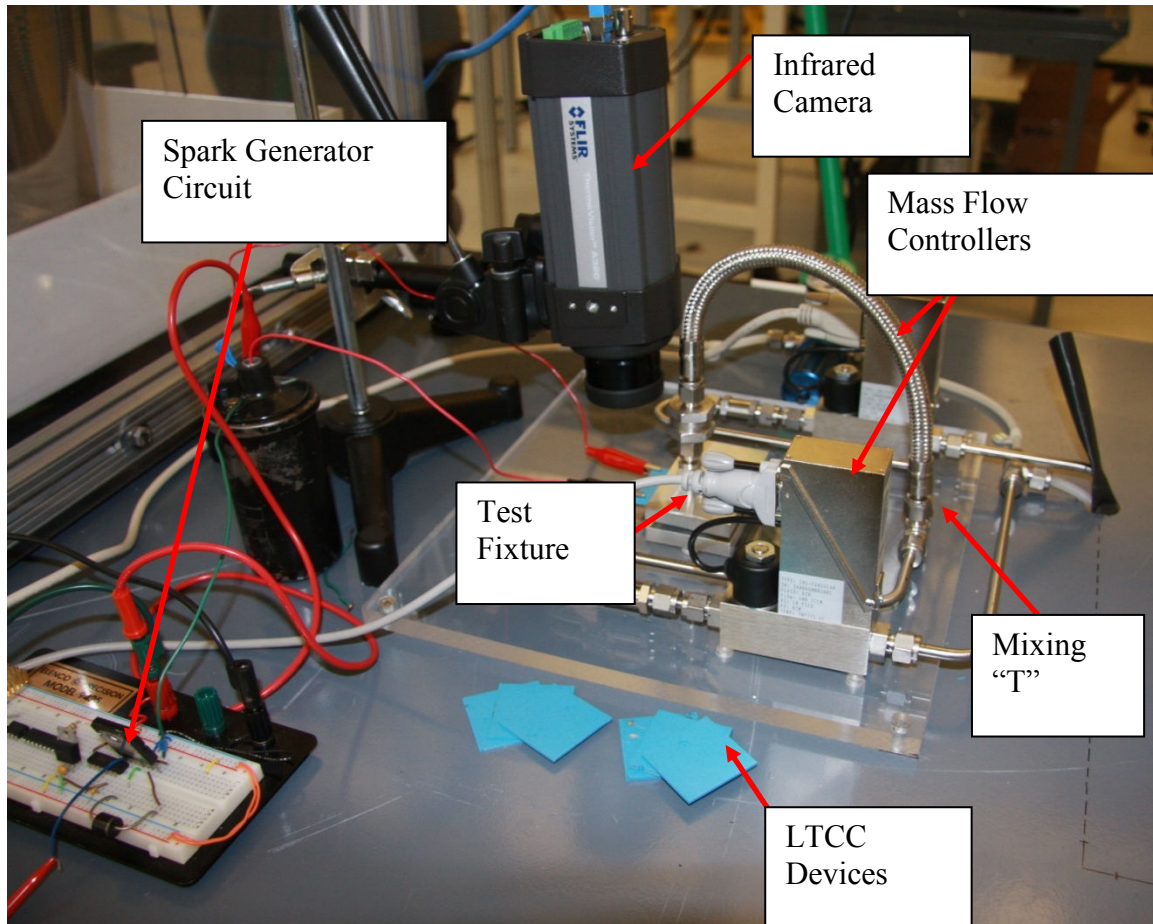
Figure 42. Experimental testing apparatus. Depicted are all major

components detailed in this section.

Once the gasses have passed through the mass flow rate controllers, they proceed to the inlet manifold. This consists of a T-fitting and flexible steel hose. The T-fitting allows the air and hydrogen streams to directly impinge and as a mixed gas, proceed to the LTCC combustor. The actual gas velocity in the mixing chamber and subsequent flexible tubing is 0.15 m/s at the maximum mass flow rate condition. With a total length of 0.3 m. this gives a minimum mixing time of 2 seconds, more than adequate for complete mixing of the reactants.

The combustible premixed gasses then pass through a wire screen flame arrestor. This device provides a flow restriction with a minimum hydrodynamic diameter that is smaller than the quenching distance of the fuels being used. In this case, the wire mesh was sized at 100 μm. The inlet channel to the combustion chamber in the LTCC also functions as a flow restrictor and flame arrestor as an added safety measure. The mixed gasses then pass into an aluminum flange device, specially constructed to interface with the inlet port geometry in the LTCC material. The flange contains an embedded seal to prevent gas leaks and facilitate quick replacement of the LTCC components. The flange covers approximately ten percent of the LTCC's exposed surface, minimizing the conductive losses through the aluminum plates. The design of the micro combustor also helps alleviate the losses through the aluminum plates by locating the combustion chamber outside of the flange.
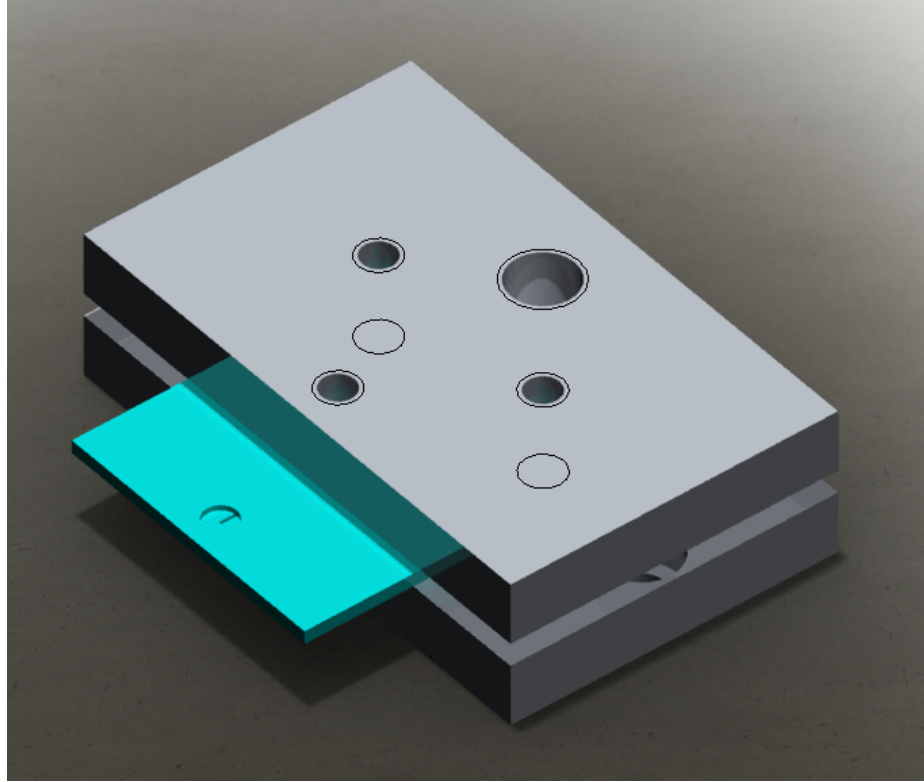
Figure 43. Aluminum fixture for interfacing the reactants to the LTCC

device. Device allows for variable clamping force to mitigate leaks.

On the upstream side of both mass flow rate controllers, a safety purging system
allows for rapid removal of the combustible gasses in the system. This safety device
simply bypasses the hydrogen's feed line and purges the entire hydrogen line with high
pressure air. In testing, the entire system can be purged in less than ten seconds after the
safety valve is opened.

Spark Electrode Circuitry

The spark ignition circuitry allows for LabView to pulse the igniter until a temperature increase in the exhaust plane gasses is detected, indicating successful ignition. This circuit relies on embedded timing elements and a high voltage flyback transformer. The timing circuit is tuned through variable resistors to match the resonant peak of the flyback coil and the spark ignition leads. In practice, the ignition circuitry required only minor adjustment for optimum spark generation. The high power nature of this circuit required the use of a high power MOSFET driving transistor. Depending on the exact geometry of the ignition coils in the LTCC device, the Metal-Oxide-Semiconductor Field-Effect Transistor (MOSFET) required between 6-7 amps at 16 volts. This represents a significant power input to initiate combustion, however, with more advanced timing and high voltage generation devices, this power requirement could be significantly reduced.

The circuit interfaces with the DAQ board through an optically isolated transistor. This prevents the high frequency feedback generated by the car coil from interfering with the precision mass flow rate commands and measurements. The circuit also relies on temperature readings provided by a thermocouple at the exhaust port. When the firing sequence is initiated by the user, LabView orders the spark circuitry to fire 10 Hz pulses with a 50% duty cycle. Between pulses, the temperature of the exhaust port is polled. When the thermocouple passes a preset threshold of 250 C or is active for more than ten seconds, the ignition circuitry is turned off, returning either a successful ignition or fault. The circuit boards were designed in EAGLE and were chemically etched into double

sided copper clad boards. This provided increased reliability over the original prototype

board design.
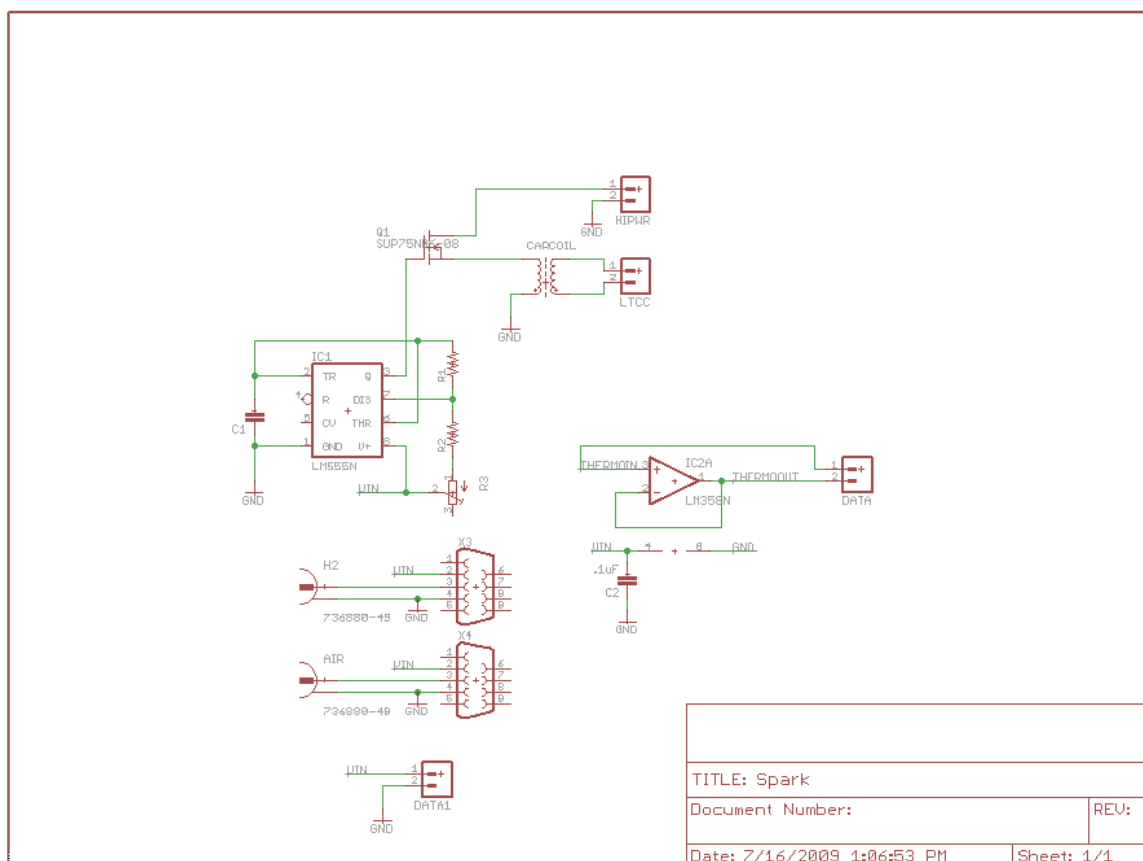
Figure 44. EAGLE schematic of spark generation circuitry.
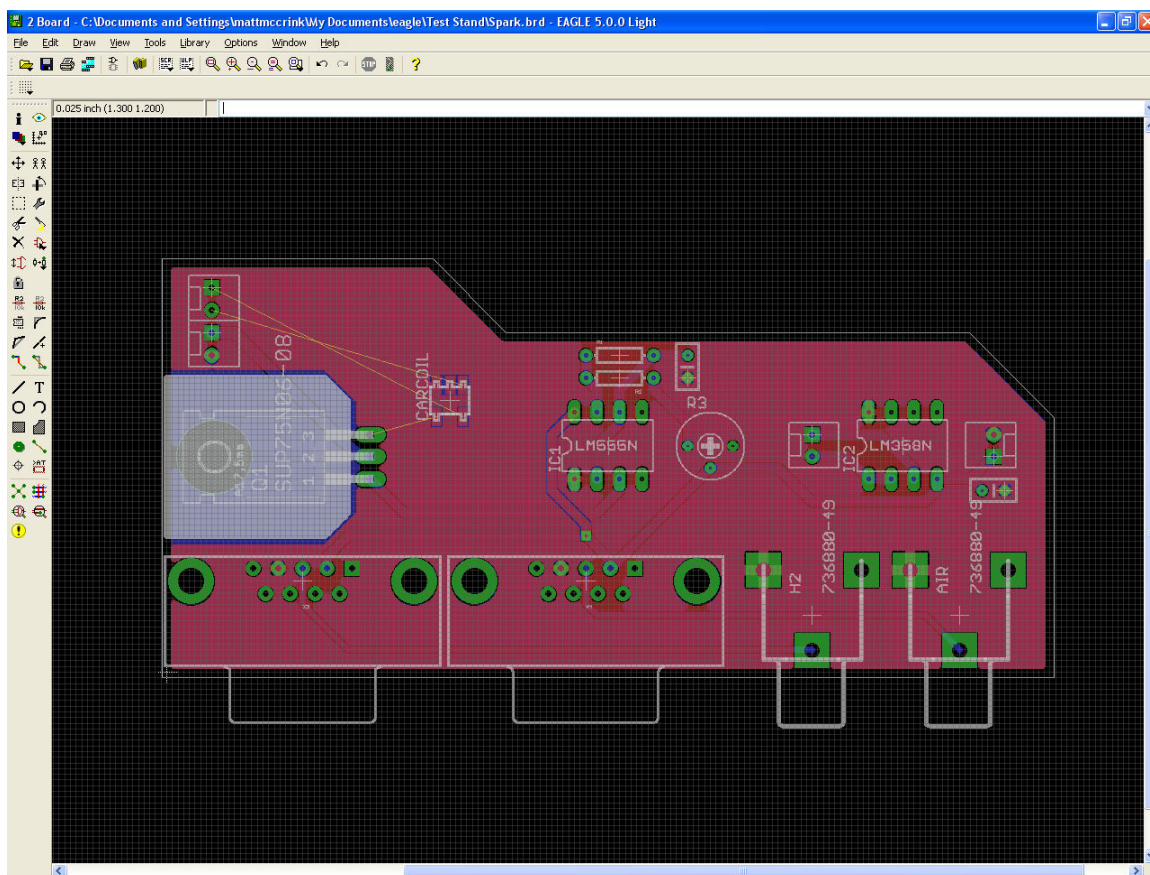
Figure 45. EAGLE board layout for the spark generation and control circuitry.

LabView Interface

The LabView interface created for this experimental apparatus allowed for direct control of the equivalence ratio and mass flow rate of the reactant gasses. The inputs for the control software are the required equivalence ratio, channel cross sectional area, and the predicted laminar flame speed of the mixture. The mass flow rate of the reactants is then calculated using the definition of the mass flow rate.

The interface also adds an additional layer of safety to the operation by incorporating an auto-purging feature. This feature automatically purges the hydrogen line on startup, shutdown, and at the end of a testing sequence. This added layer of safety requires no user input. Additional safety features include an auto-shutdown procedure that occurs in the event of a system crash or power failure. This occurs by embedded circuitry in the mass flow rate controller interface boards and ensures that the valves are closed if a spurious signal is received or power is lost.

The control portion of the interface is capable of ramping or holding the equivalence ratio or mass flow rate and reactants. The initial startup procedure purges the air out of the hydrogen lines for a preset period to ensure that the equivalence ratio of the reactants delivered to the device is the require amount for the given test. Purging time is dependent on the total system mass flow rate demanded and ranges from between two and five seconds. After the initial hydrogen purge, the air stream is initialized and the air streams are allowed to come into chemical equilibrium, requiring approximately ten seconds. As previously mentioned, the purge timing is calculated from the total mass flow rate of reactants and the enclosed volume of the interfacing tubing.

After reaching chemical equilibrium, the ignition circuitry is primed and fired for a maximum period of ten seconds. It was found that if ignition took longer than approximately ten seconds, there was most likely a problem with the LTCC device, or the flange seal to the combustor. If no change in temperature was registered after ten seconds, the system goes into a shutdown purge mode where the hydrogen is removed from the inlet lines, providing a safe environment for the disassembly of the apparatus.
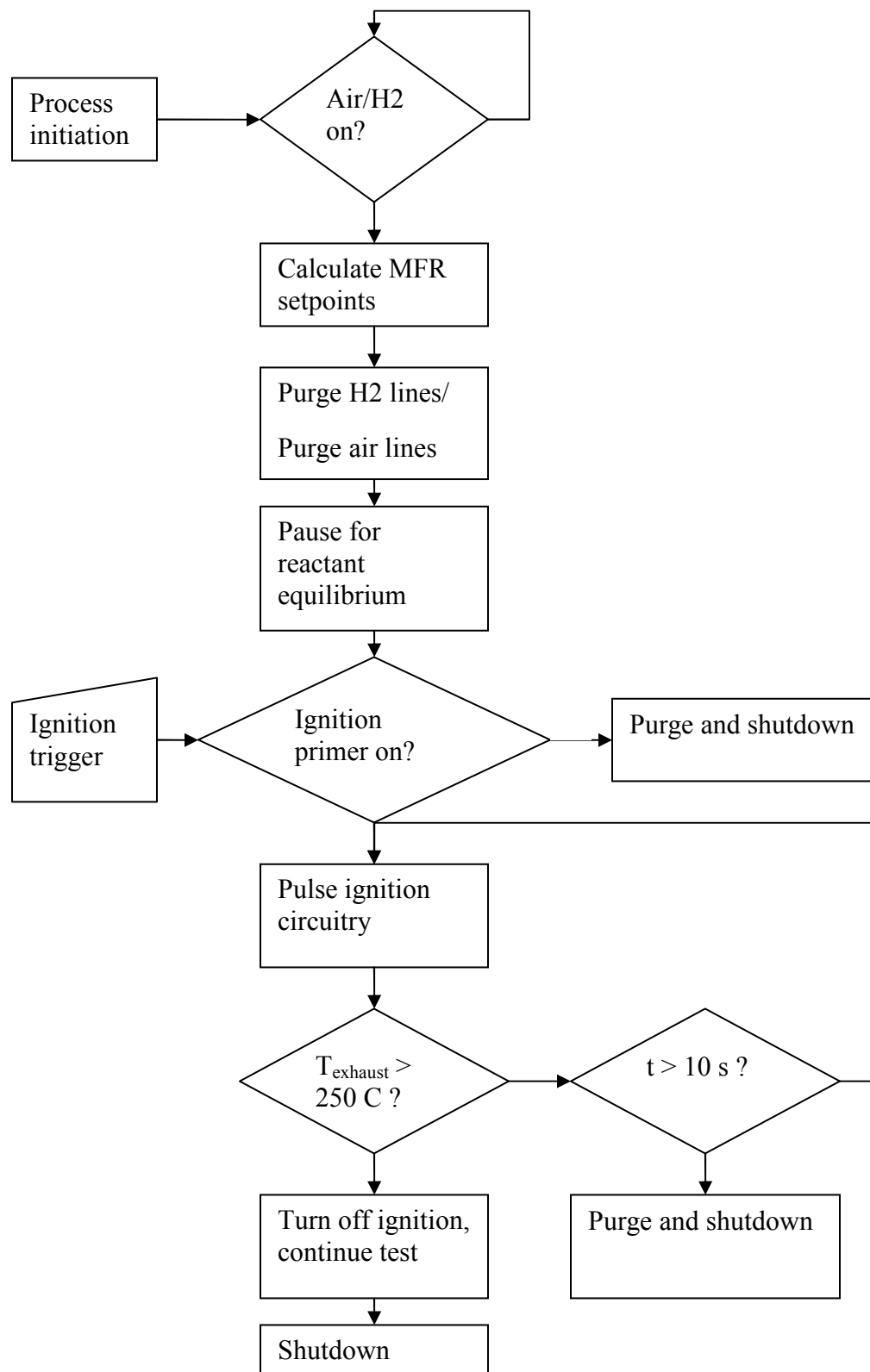
Figure 46. Control logic for LabView controller software.

In parallel with the testing apparatus, surface temperature data was gathered using a FLIR A320 infrared camera and the ExaminIR image capturing and analysis software. The infrared camera is placed directly above the extending LTCC combustor and captures the time history of the devices surface temperatures. The ExaminIR software studio allows for direct analysis of the temperature data and exportation to other analysis software packages such as Matlab and Excel. The software supports functions to determine the maximum, average, and temporal variation in surface temperatures, allowing for rapid determination of the performance of the LTCC combustors. The temperature data provided by the camera is the main means of determining the validity of the analytic and computational models.

To determine the surface heat flux, an estimate of the surface heat transfer coefficient is needed. To facilitate rapid analysis of the temperature and heat flux data, a Matlab script will scale the devices temperature profile and discretize the combustor into preset 1 mm x 1 mm surface points. Using an average nodal temperature and a prescribed heat transfer coefficient, the total heat flux from the surface is calculated according to the definition of the heat transfer coefficient. While it currently is only possible to visually analyze the top surface of the devices, it is assumed that the temperature profile of the bottom surface is a mirror image of the top. The heat transfer coefficient differs slightly in that it is based on a different correlation parameter for an inverted surface undergoing natural convection. This results in a heat flux from the bottom surface that is slightly less than the heat loss through the upper surface.

The thermocouple that is tied to the ignition circuitry also continues its measurements during the testing phase. It is assumed that the thermocouples measured

temperature represents an average temperature across the exit plane of the device. Therefore the heat leaving the exit plane of the device is computed simply as in Equation 42. The total heat output of the device is then the sum of the heat released through the top, bottom, and exit planes of the device. The current model does not account for heat leaving through the sides of the device or the heat loss to the aluminum flange. During the experimental testing, the regions of highest temperature were found to exist far away from these geometric features. It would be possible in future design iterations to incorporate the heat loss through the LTCC sides and aluminum fixtures by adding additional imaging cameras.

$$q_{exit} = \dot{m}C_p\left(T_{flame} - T_{exit}\right)$$

Equation 42. Exit plane heat flux formulation. The thermocouple measured the exit plane temperature T_{exit}.

The transient characteristics of the devices immediately after ignition show an exponential increase in temperature. The time constant for this increase in temperature is on the order of 2-5 seconds depending primarily on the equivalence ratio and substrate thickness. The device responds quickly to step changes in both mass flow rate and equivalence ratio step inputs, typically requiring less than two seconds to reach its new equilibrium state.

This testing apparatus and control circuitry allowed for the testing and data gathering from all the devices constructed for this work. The results of the experimental testing are the subject of the next section.

Generation 1 Testing

The first generation devices were designed to test the experimental apparatus and consisted of a 0.15 mm^2 channel exiting out the side of the device, shown in Figure 47. Using these channels, flames with a wide equivalence ratio were sustained and their temperature profiles recorded for comparison to future shrouded channels. The small channel size of these devices prevented the flame from entering the channel in the substrate, instead, the flame was stabilized at the exit plane of the device. This allowed the device to operate with equivalence ratios ranging from 0.3 to 1.5. The mass flow rates predicted by the analytic model were sufficient to stabilize the flame in the exit port.

The substrate temperatures were recorded using a FLIR infrared camera and a thermocouple placed on the top surface of the device, directly above the channel exit. The successful testing of this device allowed for confidence in the flow delivery performance of the testing apparatus. The next design focused on the substrates thermal performance when exposed to the hydrogen and air flame.
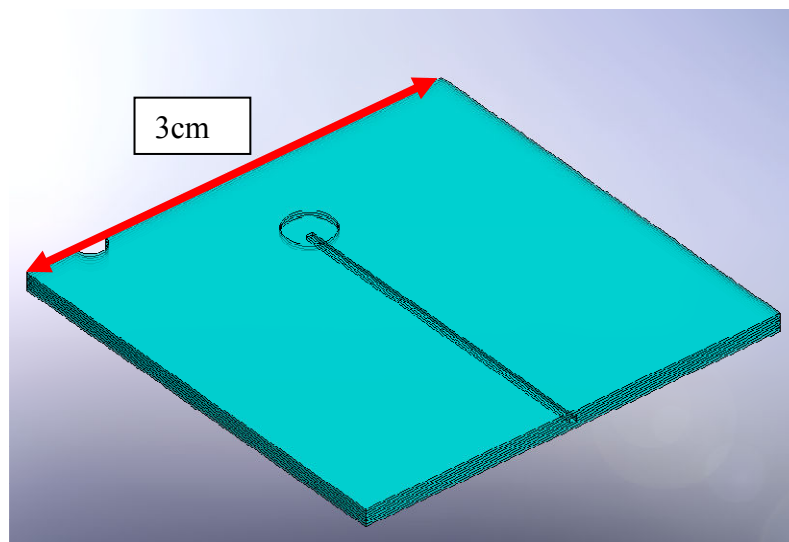
Figure 47. SolidWorks rendering of the first generation device. Note single channel exiting out the side of the device. This image is presented in the same perspective as the thermal image in the next figure. Note that the top device layers are transparent in the model for visualization of the channel.
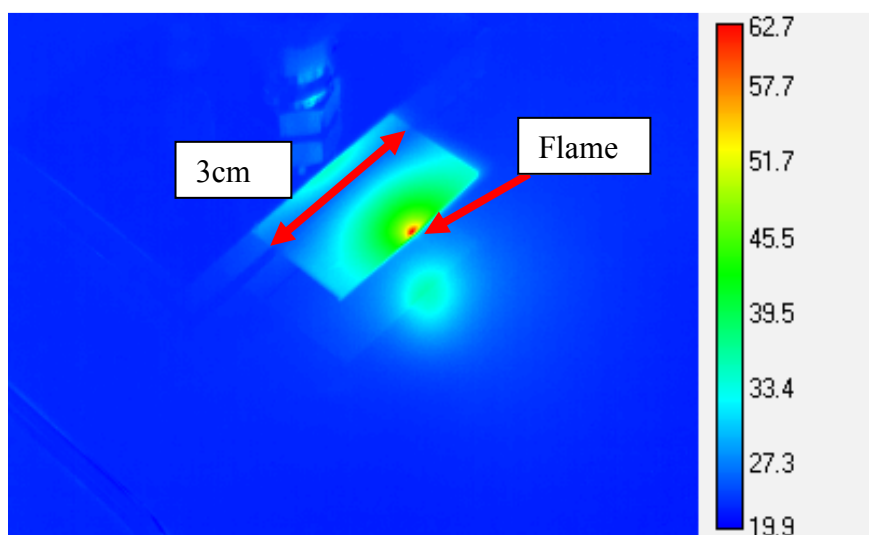
Figure 48. Thermal image of generation 1 device. This image was taken with an equivalence ratio of 1.2 and a total mass flow rate of 2.56e-6 kg/s. The temperature bar is calibrated in Celsius.

Generation 2 Testing

A second set of channels was then tested as depicted in Figure 49. These channels supported a flame in direct contact with substrate surface and tested the long-term duration of the LTCC when exposed to surface temperatures in excess of 250 C, shown in Figure 50. This testing was undertaken in response to micro propulsion device thermal failures at similar temperatures. The tests were run in two-hour blocks and no significant deformation or cracking of the channels was observed. These channels also served as the test bed for the embedded spark discharge contacts. The success of this generation moved the designs towards the analytic geometry consisting of an enclosed channel where the flame would be stabilized.

3cm
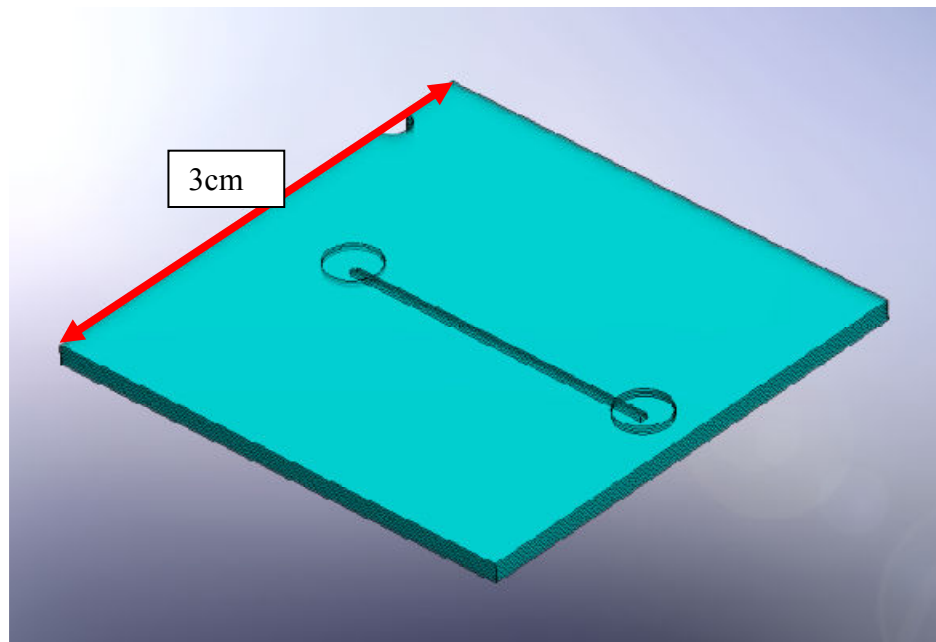
Figure 49. CAD image of generation 2 device. This device contains a single inlet port and an exit that forces the flame to impinge directly on the substrates

surface. This generation showed no adverse effects to high temperatures and high

substrate thermal gradients.
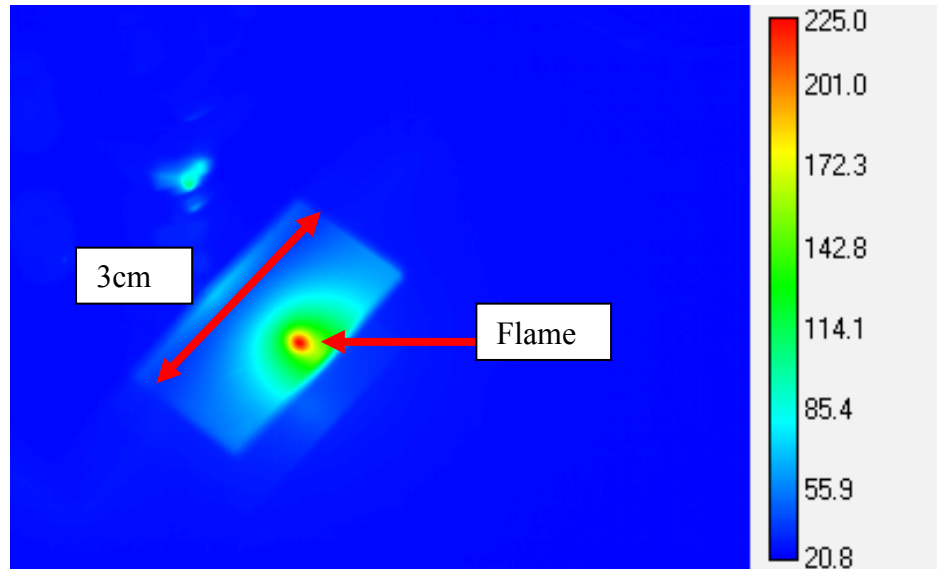
Figure 50. Generation 2 infrared image. Note flame is stabilized in direct

contact with the surface of the device. The temperatures in the scale bar are

reported in Celsius.

Generation 3 Testing

The third generation devices represented the first internal combustor geometry. This device did not successfully enclose the flame. Instead, the shortened large channel geometry was determined to be too short for successful stabilization of the flame. This is due primarily to the higher core velocity emanating from the smaller, 0.15 mm^2 feeder channel. A simple non-reacting Fluent simulation, shown in Figure 51, indicated that the higher velocity core did not dissipate until the gas had passed out of the channel, making successful flame stabilization impossible. To alleviate the problems encountered with this generation, a longer large channel portion was added to the future designs. This

addition increased the large channel length from 0.5cm to 2cm. This provided adequate time for the higher velocity core flow to dissipate into the large channel, reducing the reactant velocity to the predicted flame speed value.
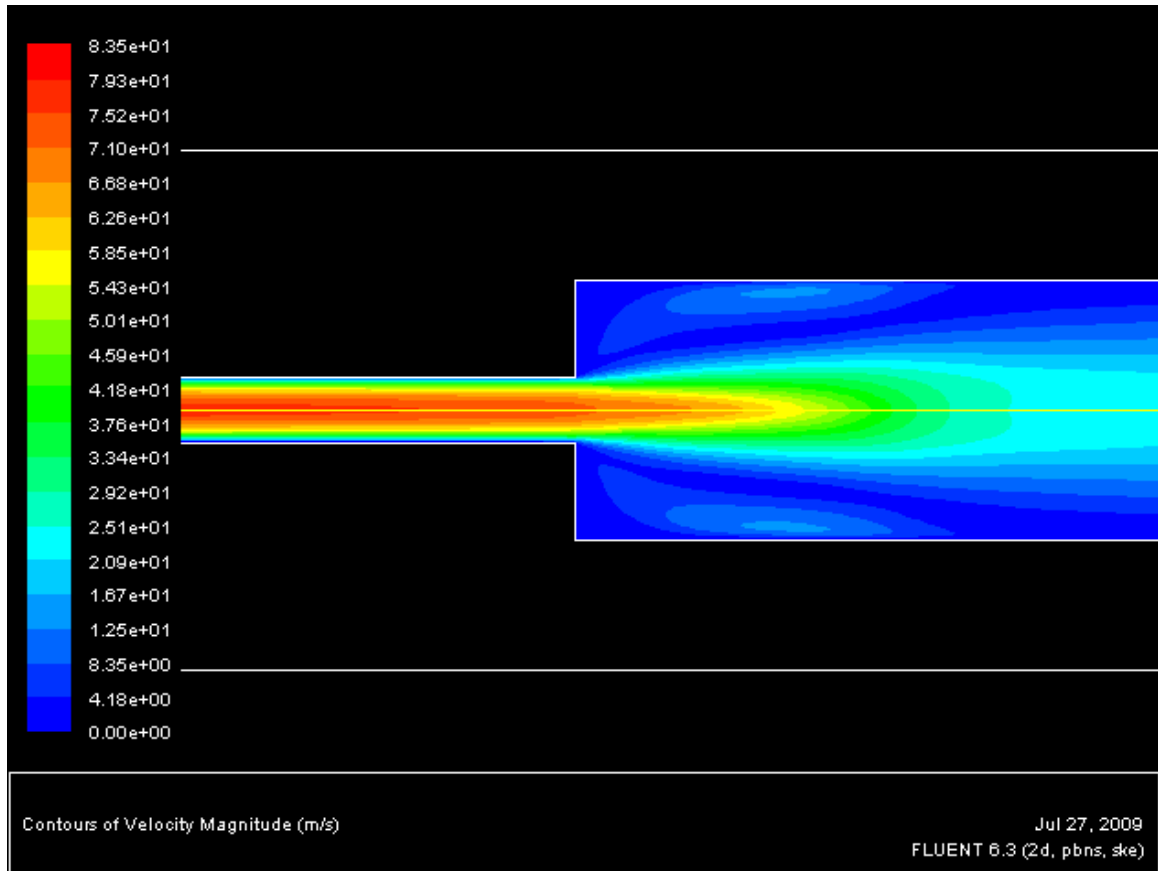
Figure 51. Fluent velocity contours for generation 3 device. Note high core flow velocity. This was determined to be the cause of this generation's failure. Future generations contained a longer inlet channel to better dissipate the high-speed core flow.

Generation 4 Testing

The fourth device was designed using the accumulated experience and knowledge of the first three devices. It consists of a small 0.15 mm^2 channel that opens into a larger 2 mm^2 channel, approximately 2 cm long. The small inlet channel acts as a safety mechanism to prevent flashbacks and to move the combustion region out of direct contact with the aluminum plates used to secure the device during testing. By shifting the device out from the plates, a direct optical path exists between the top surface of the channel and the infrared camera, limiting the thermal losses through the much more conductive aluminum. This is the first device in which a flame was stabilized inside the channel, with a corresponding maximum substrate temperature of 253 C. These results were obtained with a mass flow rate of 3.53 x 10^{-6} kg/s and an equivalence ratio of 0.4. To test the stability of the flame in the channel, step changes in the inlet velocity were applied at random times during the testing process. The flames proved to be very stable both above and below the published laminar flame speed range of premixed hydrogen and air.
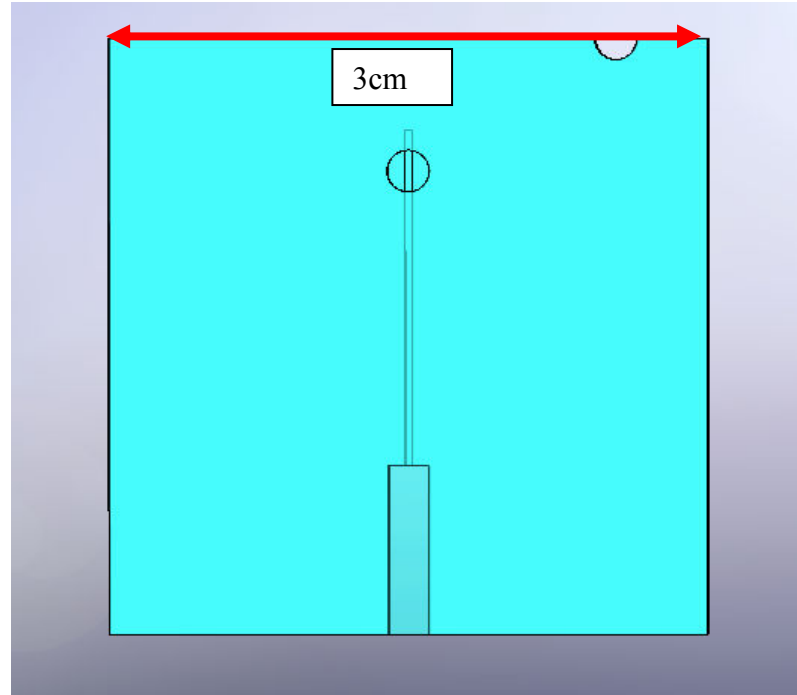
Figure 52. Generation 4 CAD rendering. Note increased large channel length over generation 3 devices. This increased channel length allowed for the successful stabilization of the flame inside the channel.
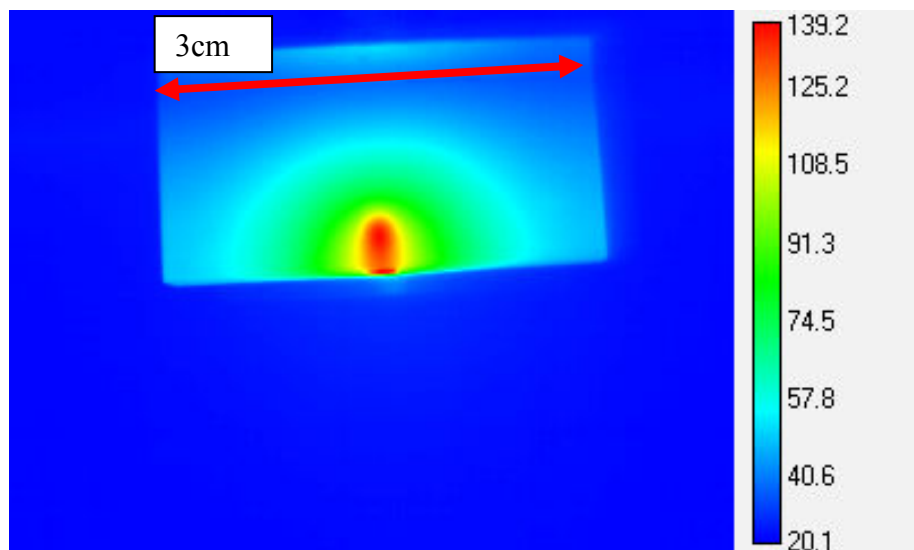
Figure 53. Infrared image of flame in generation 4 channel. The increased large channel length allowed for the successful stabilization of enclosed flames across a large operational regime.

The fourth generation devices were constructed in accordance with the predictions of the analytic models. The surface temperatures predicted by the analytic model were in close agreement with the infrared measurements taken during testing. The predicted exit plane temperature for an equivalence ratio of 0.5, as pictured in Figure 53, is 225 C, whereas the measured temperature was 175 C, giving an error of 22%. Perhaps more important than the prediction of the surface temperatures is the prediction of the stability margins over which the flame can be successfully stabilized. The measured flammability range for the generation four devices is from equivalence ratios of 0.5 to 1.2, well above the predictions of the analytic model. These corresponding mass flow rate ranges were between 2.0e-6 kg/s and 5e-6 kg/s. These mass flow rates were relatively close to the predicted mass flow rate ranges of 1.2e-6 kg/s to 4.5e-6 kg/s. The disparity in the

equivalence ratio operating ranges can likely be explained by the under prediction of the exit plane temperature measurements. This increase in exit plane temperatures over the predicted values indicates that the internal heat transfer coefficients may be incorrect, and not as much heat is being transferred to the device as is being predicted. A representative graph of the measured and predicted surface temperatures is shown in Figure 54
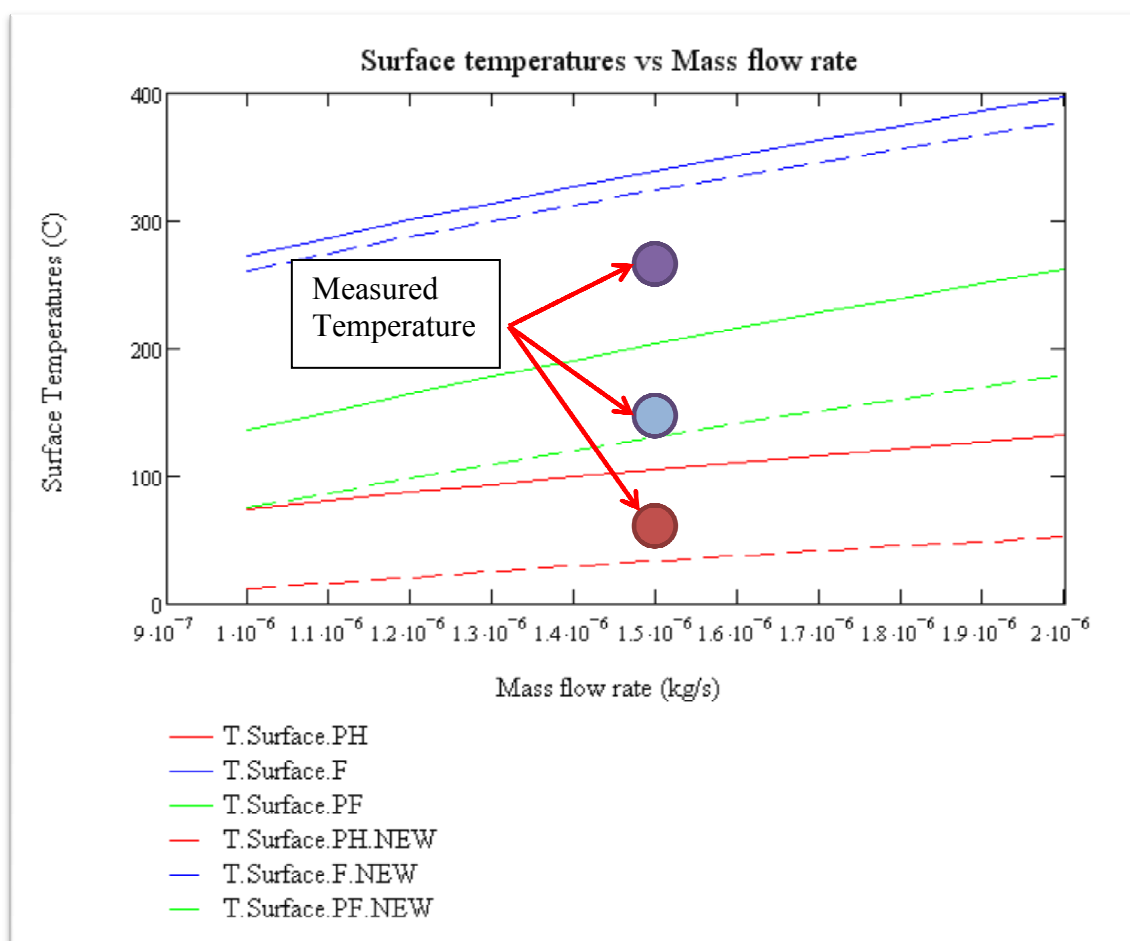
Figure 54. Measured and predicted surface temperatures for the fourth generation device. The dots represent the measured values at the indicated flow rate. The dashed lines are the updated predicted surface temperatures from the numerical model.

Generation 5 Testing

The fifth generation devices lengthened the burner from 2 cm to 5 cm, shown in Figure 55. This device was designed to further validate the flames stability margin in the channel. However, during the construction of the device problems were encountered with maintaining the channels integrity during the high pressure lamination phase. It is theorized that the high pressure lamination of the unsupported channel walls caused crack formations in the ceiling/wall interface. This problem was eventually mitigated by increasing the ceiling substrate's thickness and using a sacrificial carbon tape. By increasing the substrate's thickness, the thermal capacitance of the device was also increased. This increased thermal capacitance resulted in the flame extinguishing immediately after ignition.
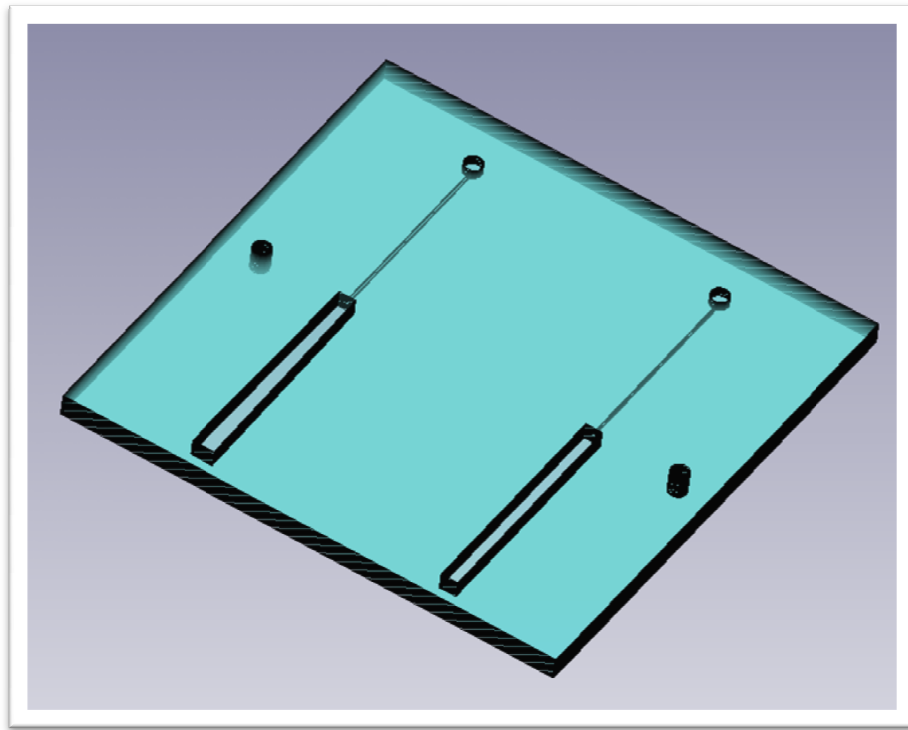
Figure 55. Generation 5 CAD rendering. Device was ultimately unsuccessful.

Generation 6 Testing

The sixth generation device was a departure from the first five generations. This design incorporated a combustor can in the transverse direction. This design was created to test an additional flame stabilization mechanism, dubbed eddy feedback. It is theorized that by artificially inducing an eddy by passing a high speed jet into a large open cylinder, there will exist some point between the stagnant core of the eddy and the high speed edges where the reactant velocity will equal the flame speed of the mixture. This region of high vorticity will then recirculate the heat from the product gasses back to the reactant gasses, stabilizing the reaction. To generate the eddies needed to test this theory, several candidate designs were produced. Pictured in Figure 56, these devices varied the location of the inlet port and the combustor geometry in an effort to induce a stable eddy. Fluent simulations were carried out for these geometries to qualitatively determine the intensity of the resulting eddy and as a method for which to determine the appropriate size of the combustor can.
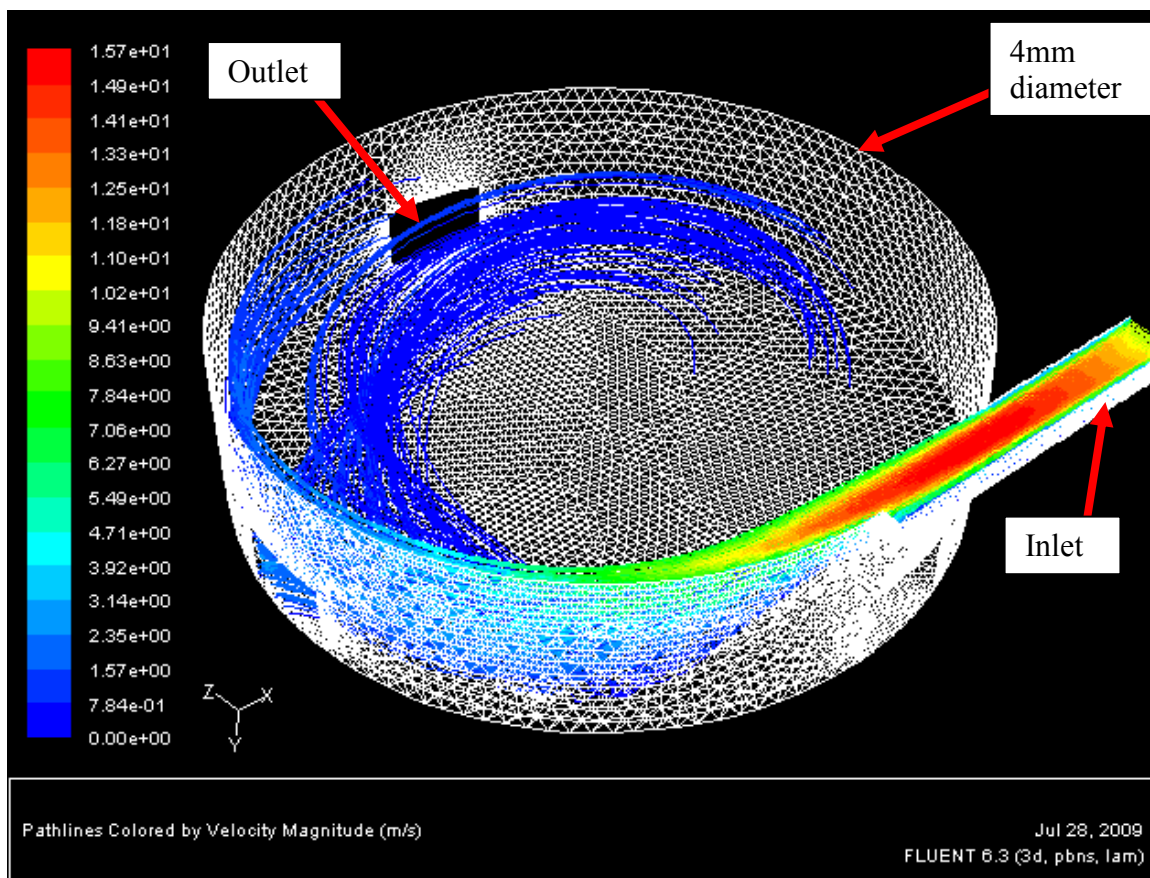
Figure 56. Fluent image of conceptual swirl combustion device. Only lower half of device is shown in the above figure, therefore, there are six exit ports and one inlet port for this device. Contours are colored by velocity
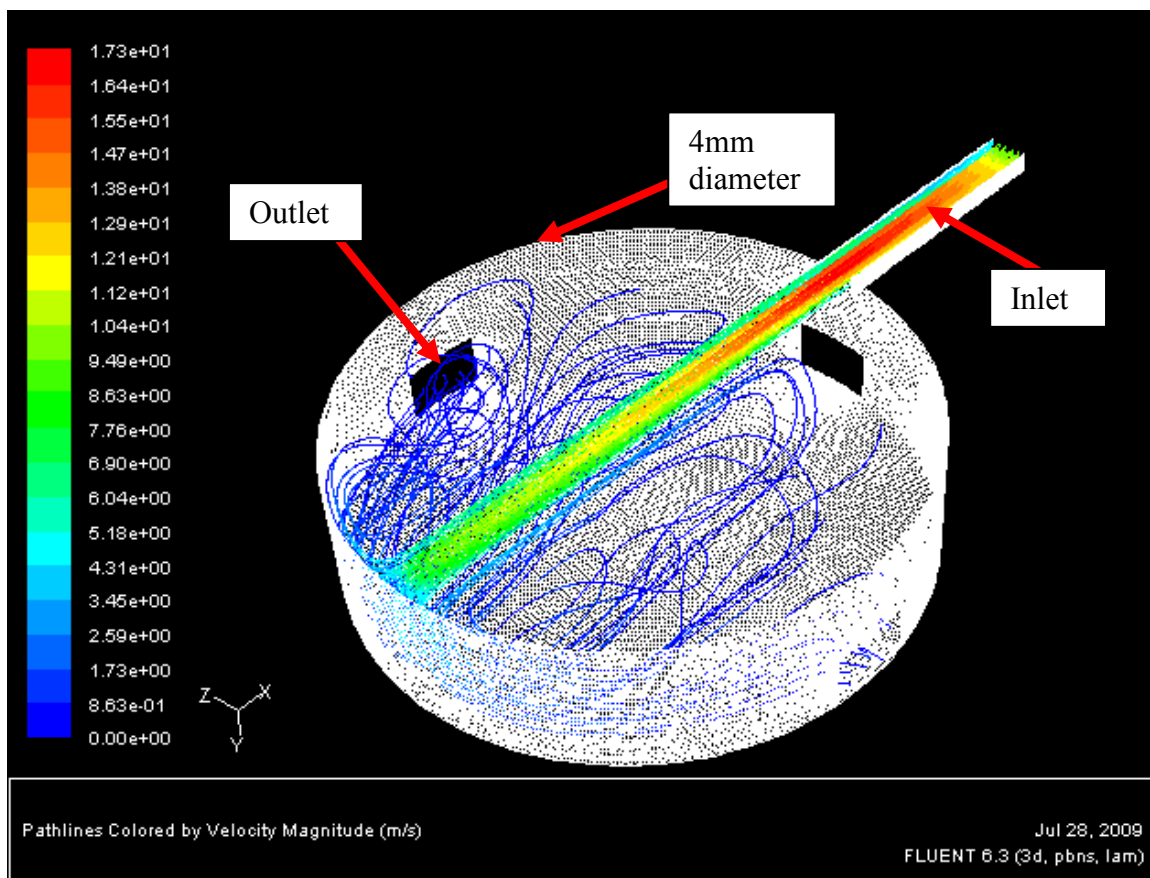
Figure 57. Conceptual design 2. Similar to previous image with inlet port in the center of the device. Velocity contours shown.

Pathlines Colored by Velocity Magnitude (m/s)

Jul 28, 2009
FLUENT 6.3 (3d, pbns, lam)
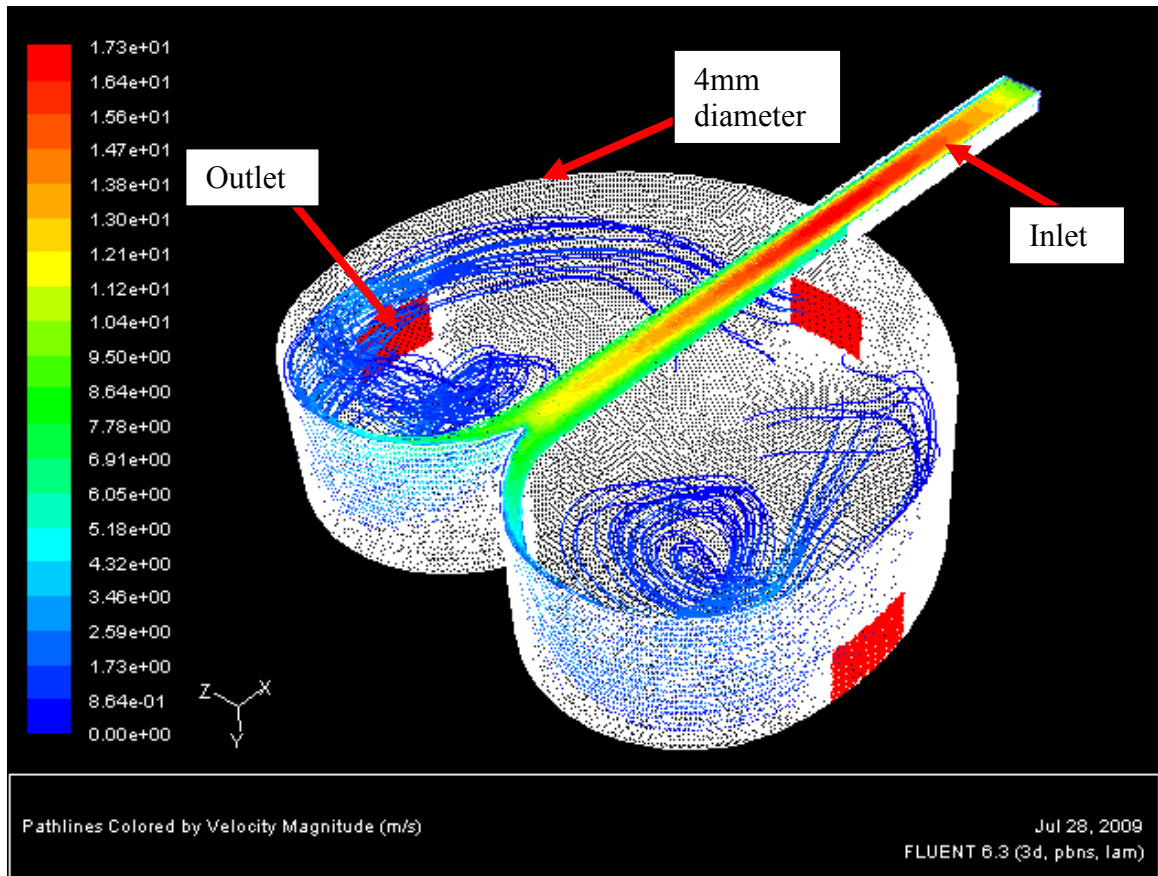
Figure 58. Fluent conceptual design 3. Note strong recirculation cells on either side of the flow splitter. This recirculation zone is the proposed stability mechanism for these devices. Contours are colored by velocity

These devices were successfully tested with reactant mixtures and flow rates similar to their axial counterparts. However, the flame would only remain stable for approximately 5-10 seconds and then extinguished itself. During this time span, the temperature would be increasing, indicating that the extinguishing mechanism was an excessive heat flux from the reaction zone.
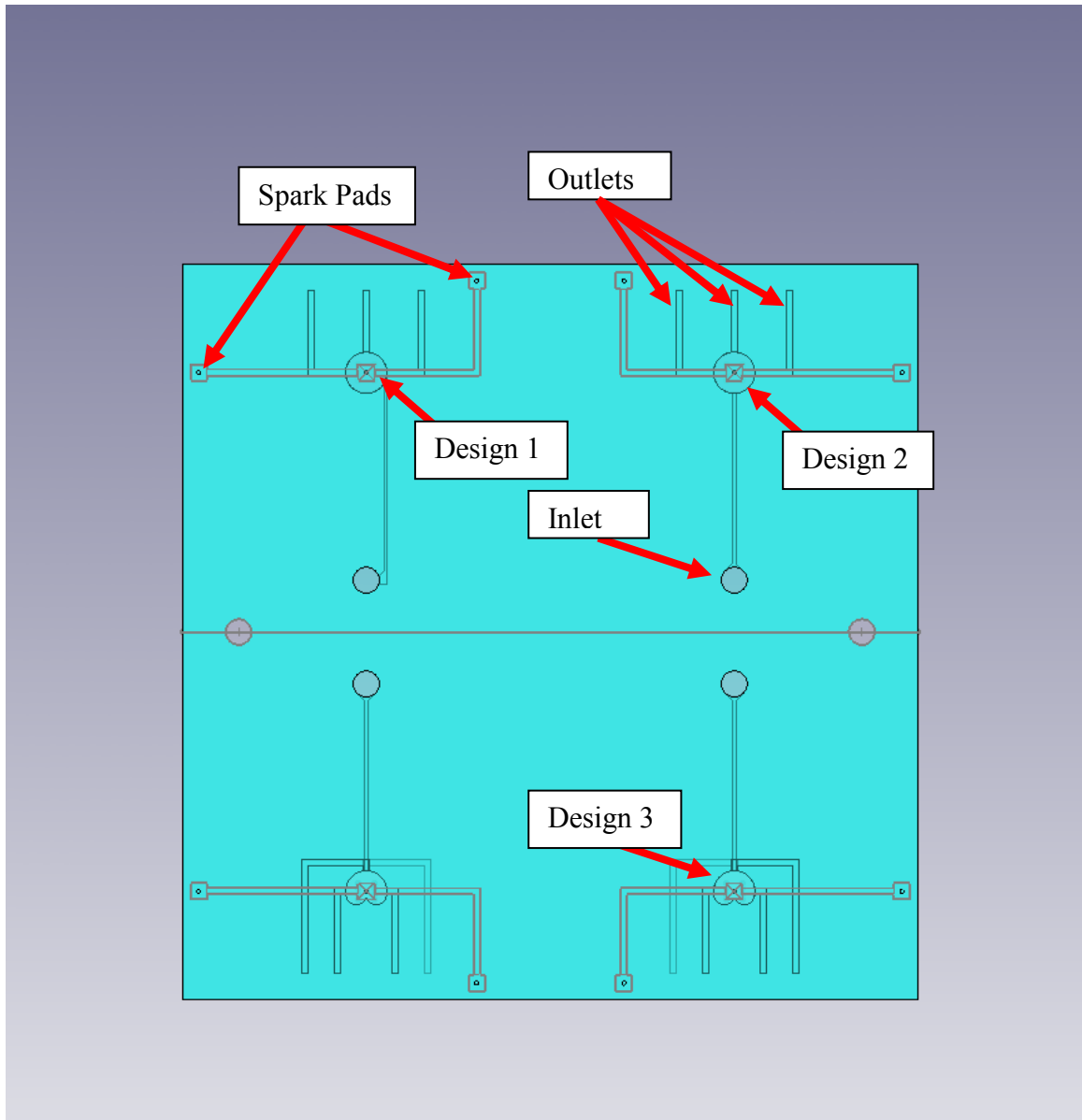
Figure 59. CAD image of generation 6 swirl combustor design. This image is transparent to show the internal channel structure. This design contains three distinct channel designs. The first is a circular region with the inlet entering from the side. The second is also a circular combustion region with the inlet port entering radially towards the center. The final design is a heart shaped combustor designed to split the flow from the inlet port.
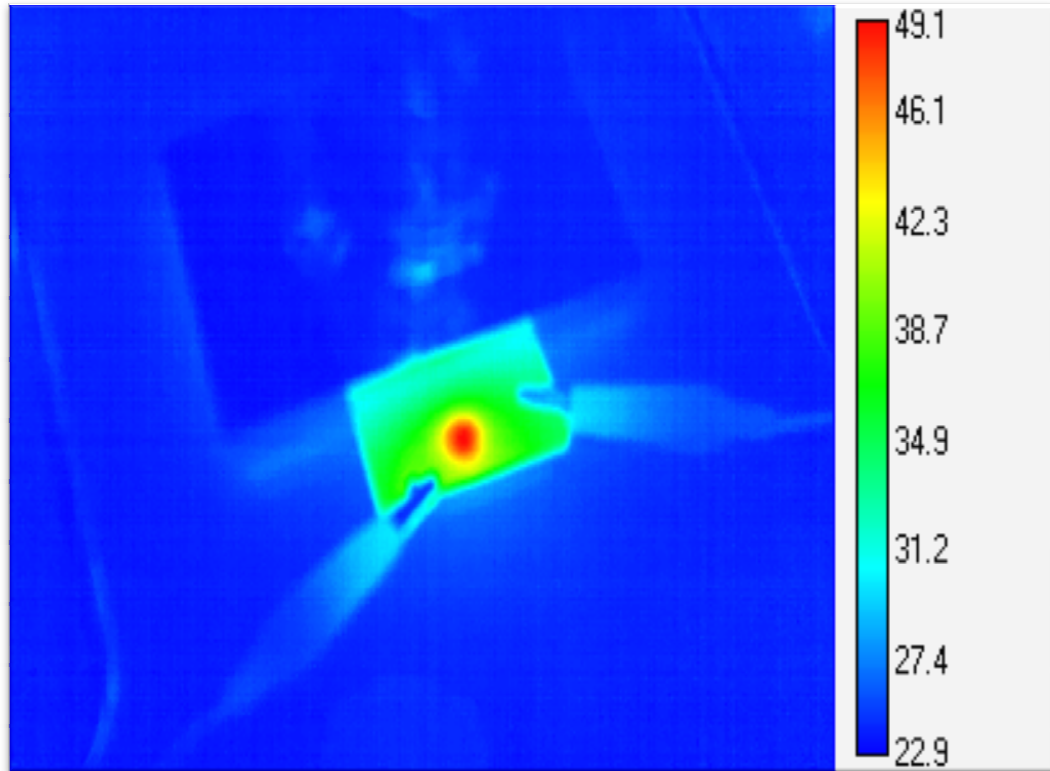
Figure 60. Successful ignition of heart shaped micro combustor. Maximum burn time was limited to approximately two seconds. Temperature plot is in degrees Celsius.

CONCLUSIONS

The success of the fourth generation micro combustor and the close prediction of the resulting surface temperatures indicates that the basic tenants of the modeling were correct. More precisely, the original assumption regarding the increased importance of the three-dimensional heat loss was proved correct through experimental testing. This effect is most noticeable in Figure 53, where the channel is clearly visible, but the heat has increased the surface temperature of the surrounding substrate considerably over the free stream temperatures. This effect represents the major departure from the modeling efforts of T. Leach and others (Leach & Cadou, 2004) (Kaisare & Valchos, 2007). Their major efforts have focused on the physics of the devices. The research presented in this thesis has taken the basic physics building blocks set forth by others and created a model reflecting actualities of a field functioning device.

The device behaviors presented by T. Leach, such as the flames stability and the effect of the bulk thermal conductivity on the device performance were reflected in the analytic model created for this specific LTCC device (Leach & Cadou, 2004). The departure from the predictions made by Leach occurred in the analysis of the heat fluxes inside the device. In these LTCC devices, a significant portion of the heat is not leaving through the top surface as in Leach's model. Conversely, a majority of the heat released through the combustion process passes through the extended surface, or fins of the device. This is primarily a result of assuming that the channel is not semi-infinite (Leach & Cadou, 2004). Along with the large fraction of heat leaving the device through the

fins, the next largest flux is through the exit port of the device. This loss is the impetus for many of the recirculating burner designs pursued by other researchers in the field (Sitzki, Borer, Schuster, Ronney, & Wussow, 2001). The recirculation of the exhaust gasses allows for a larger fraction of the heat produced to leave the device through the top surface, making it available for power production.

Having shown that loss through the exit plane of the device represents a significant fraction of the available heat, future LTCC designs could be designed to capture this energy. This would require a highly three-dimensional design and would correlate well with the construction capabilities of the material system. Another feature that would allow for better device performance and would better utilize the capabilities of the LTCC is the incorporation of silver pastes as a means of preferentially distributing the heat throughout the device. This would require the bulk properties assumption built into the analytic models to be replaced with anisotropic material properties. The preferential distribution of heat would allow for the material to function as if it had a higher thermal conductivity, widening the stability margins over the standard LTCC device and reducing the heat loss to the remainder of the substrate. These future devices would require significant additions to the models, but would not represent large departures to the current construction techniques presented in this research.

Finally, the addition of the numerical model should be expanded to include the out of plane heat transfer paths. This will in effect make the model three-dimensional and require a significant modification to the current code. This information could better tailor the predictions of the analytic model, yielding better performance estimates. This portion of the modeling proved critical in the original performance estimates and cannot

be neglected in future work. As mentioned in the introduction to the numerical modeling, the results of the analytic model are extremely sensitive to the choice of heat transfer coefficients inside the device. This knowledge led to the pursuit of a two-dimensional variable heat transfer coefficient. However, the addition of the fin surfaces could drastically affect the results obtained during the numerical modeling. Given the sensitivity of the results, this should be investigated in more detail.

This work has shown the viability of using LTCC as a rapid prototyping system for micro combustion devices. LTCC has proven advantageous through its low thermal conductivity and ability to embed electrical circuitry, such as a spark ignition system, directly into the substrate. Using this materials system, a hydrogen and air flame was successfully stabilized inside a channel created in the LTCC material. This experimental device was built on the predictions of an analytic and numerical model of the devices performance and showed similar stability trends. The experimental device did however prove to be more stable than the predictions indicated. This is due in part to the embedded assumptions in the analytic model that did not precisely capture the three dimensionality of the internal heat flows.

This work presented the design, analysis, and testing of a LTCC micro combustor. The successful designs and models presented in this work will provide a stepping stone the development of more advanced devices in the future.

REFERENCES

Anderson, J. (1995). *Computational Fluid Dynamics*. McGraw-Hill.

Carl. (2009). *"Carl's electronics"*. Retrieved 2009, from

http://www.electronickits.com/kit/complete/peltier/ck501.htm

Depcik, C. (2006, March). *Wikipedia*. Retrieved July 2009, from

http://en.wikipedia.org/wiki/File:Cvft.jpg

Dewitt, F. P., & Incropera, D. P. (1996). *Fundamentals of Heat and Mass Transfer* (6

ed.). John Wiley & Sons.

DiSalvo, F. J. (1999). Thermoelectric Cooling and Power Generation. *Science , 285*

(5428), 703-706.

DuPont. (2001, March). *951 Green Tape Datesheet*. Retrieved 2009, from

http://www2.dupont.com/MCM/er_us/assets/downloads/prodinfo/CFOXX.pdf

DuPont. (2003). *DuPont LTCC Green Tape Technology*. Retrieved July 2009, from

http://hdmicrosystems.com/MCM/en_US/LTCC_Overview.pdf

Flipsen, S. J. (2006). Power sources compared: the ultimate truth? *International Power*

Sources Symposium , 162 (2), 927-934.

Golonka, L. J., Zawada, T., Radojewski, J., Rogusczack, H., & Stefanow, M. (2006). LTCC Microfluidic System. *International Journal of Applied Ceramic Technology , 3* (2), 150-156.

Gongora-Rubio, M. (1999). LTCC Technology multilayer eddy current proximity sensor for harsh environments. *SPIE proceedings series , 3906*, 676-681.

Jiang, K. C., Prewett, P. D., Ward, M. L., Tian, Y., & Yang, H. (2001). Design of a micro Wankle rotary engine for MEMS fabrication. *SPIE Proceedings, MEMS Design, Fabrication, Characterization, and Packaging , 4407*, 54-60.

Jones, W. K., Liu, Y., & Zampino, M. (2003). Thermal management using low tempeature co-fired ceramic. *Proceedings, Electrochemical Society , 27*, 200-208.

Jurkow, D., & Golonka, L. (2008, December). Novel cold chemical lamination bonding technique - A simple LTCC thermistor-based flow sensor. *Journal of the European Ceramic Society* , 1971-1976.

Kaisare, N. S., & Valchos, D. G. (2007). Optimal reactor dimensions for homogeneous combustion in small channels. *Catalysis Today , 120*, 96-106.

Law, C. K. (2006). *Combustion Physics*. New York: Cambridge Hill.

Leach, T., & Cadou, C. (2004, January 5-8). Effect of Structural Heat Conduction on the Power Density of Micro-Combustors. *42nd AIAA Aerospace Sciences Meeting and Exhibit* , 5-8.

Liepmann, H. W., & Roshko, A. (2002). *Elements of Gas Dynamics*. Dover Publications.

Maruta, K., Takeda, K., Ahn, J., Borer, K., Sitzki, L., Ronney, P. D., et al. (2002). Extinction Limits of Catalytic Combusion in Microchannels. *Proceedings of the Combustion Institute , 29* (2002), 957-963.

NovaSensor. (n.d.). Data Sheet: NPC-107 Series Disposable Medical Pressure Sensor. Freemont, CA: Lucas NovaSensor.

Peterson, K., Patel, K. D., Ho, C. K., Rohde, S. B., Nordquist, C. D., Walker, C. A., et al. (2005). Novel Microsystem Applications with Now Techniques in Low Temperature Co-Fired Ceramics. *International Journal of Applied Ceramic Technology* , 345-363.

Pletcher, R. (1997). *Computational Fluid Mechanics and Heat Transfer.* Taylor and Francis.

Plumlee, D. G. (2007). *Development of a monopropellant micro-propulsion device in low temperature co-fired ceramics.* Moscow: University of Idaho.

Sadler, D. J., Changrani, R., Roberts, P., Chia-Fu, C., & Zenhausern, F. (2003). Thermal Management of BioMEMS Temperature Control for Ceramic-Based PCR and DNA Detection Devices. *IEEE Transactions on Component and Packaging Technologies , 26* (2), 309-316.

Sitzki, L., Borer, K., Schuster, E., Ronney, P. D., & Wussow, S. (2001). Combustion in Microscale Heat-Recirculating Burners. *The Third Annual Asia-Pacific Conference on Combustion* , 11-14.

Snyder, J. G. (2008). Small Thermoelectric Generators. *The Electrochemical Society Interface , 13* (3), 54.

Systems, Universal LASER. (2009). *Universal LASER Systems*. Retrieved 2009, from http://www.ulsinc.com/?gclid=CIujkrz8-JsCFR9N5QodNg7x_g

Tanaka, S., Yamada, T., Sugimoto, S., Li, J. F., & Esahi, M. (2003). Silicon nitride ceramic-based two-dimensional microcombustor. *Journal of Micromechanics and Microengineering , 13* (3), 502-508.

Taylor, B. E., Bidwell, L., & Lawrence, A. (2001). New Photoimageable LTCC Technology for making a wide range of Ceramic architectures and circuits. *SPIE Proceedings , 4428*, 87-92.

Thelemann, T. H., Thrust, H., & Hintz, M. (2002). Using LTCC for microsystems. *Microelectronics International , 19* (3), 19-23.

Turns, S. R. (2006). *An Introduction to Combustion.* Singapore: McGraw-Hill Higher Education.

Vican, J., Gajdeczko, B. F., Dryer, F. L., Milius, L., Aksay, I. A., & Yetter, R. A. (2007). Development of a microreactor as a thermal source for microelectimechanical systems power generation. *Proceedings of the Combustion Institute , 29* (2002), 909-916.

Yoshida, K., Tomonari, S., Yoshioka, H., Tanaka, S., Satoh, D., Esashi, M., et al. (2004). High energy density miniature eletrical and thermal power using catalytic combustion of butane. *17 IEEE Conference on Micro Electro Mechanical Systems* , 316-321.

Younsgman, J. (2006). *Mini and Micro-Channel Devices in Low Temperature Co-Fired Ceramics.* Boise: Boise State University.

APPENDIX

Code: Explicit Viscous Navier-Stokes Solver

Section 1: Initialization loop and main counter

```
INP1 = input('start = 1, continue = 0 ');


if INP1 ==1;


evalin('base','clc,clear') %clears root working directory from previous run



%Establish matrix size and initial constants;
length = .01;
height = .001;
Sheight = 0.002;
Slength = 0.01;


xp = 50;
yp = 40;
xps = xp;
yps = 20;


dx = length/(xp-1);
dy = height/(yp-1);
dxs = dx;
dys = Sheight/(yps-1);



RU1old = 1;
RU2old = 1;
```

```matlab
RU3old = 1;
RU4old = 1;


%Constants;
Pr = 0.71;              %Prandtl number
R = 287;                %Universal gas constant (J/kg-K)
gamma = 1.4;            %Ratio of specific heats


Twall = 500;            %Wall Temperature (K)
Tin = 350;              %Inlet fluid temperature (K)
Tinf = 300;             %Far field temperature estimate(K)
Tref = 288.16;          %Viscosity reference temperature (K)


Pin = 101425;           %Inlet total pressure (Pa)
Pinf = 101325;          %Far field pressure, will be updated (Pa)


Uinlet = 0;             %X component of inlet Velocity for flow field (m/s)
Vinlet = 0;             %Y component of inlet Velocity for flow field (m/s)


muinlet = 1.5e-5;       %Viscosity at fluid inlet (kg/m-s)
muref = 1.7894e-5;      %Reference viscosity used in Sutherland model
            %(kg/m-s)


%Constant boundary conditions
utop = zeros(1,xp);     %Creates constant boundary condition vectors such
ubottom = utop;         %as the zero velocity vectors for the walls and
vtop = zeros(1,xp);     %constant wall temperature vectors.
```

```
vbottom = vtop;

Poutlet(1:yp,1) = Pinf;

Ttop = Twall;

Tbottom = Twall;


%Calculate viscosity following Sutherland approximation;


%Far field viscosity for initialization
muinf = muref*(Tinf/Tref)^(3/2)*(Tref+110)/(Tinf+110);


%Calculate specific heat values;

Cv = R/(gamma-1);

Cp = gamma*Cv;


%Calculate thermal conductivity;

k = muinf*Cp/Pr;    %Assumes constant Pr number


%Initialize flow variables and generate base matrices
u(1:yp,1:xp) = (((((Pin./Pinf)).^((gamma-1/gamma)-1).*2./(gamma-1)).^...
    .5).*(gamma.*R.*Tin).^.5;

v(1:yp,1:xp) = Vinlet;

T(1:yp,1:xp) = Tin;

Ts(1:yps,1:xps) = 300;

P(1:yp,1:xp) = Pinf;

rho = P./(R.*T);


%Apply boundary conditions
```

```
[u,v,P,T,rho] = Boundary(rho,u,utop,ubottom,v,vtop,vbottom,...
    P,Pin,Poutlet,T,Tin,Ttop,Tbottom,gamma,xp,yp,R);


%Calculate viscosity, density, thermal conductivity,
% and energy at all points
mu = Sutherland(muref,T,Tref);
lamda = -2/3.*mu;


k = mu.*Cp./Pr;
e = Cv.*T;


Iteration = 1;


end;


INP2 = input('Iterations ');
INP3 = input('Courant Number (0.001 - 0.8) ');


start = Iteration;
finish = Iteration+INP2;
Dt(start:finish,1) = 0;
% INP3 = K;
K = INP3;


%Main loop
for I = start:finish;
```

```matlab
%Calculate the Courant based time step
dt = Timestep(u,v,dx,dy,R,mu,gamma,rho,T,K);


%Executes the MacCormack predictor-corrector scheme
[rho,u,v,e,T,Ts,P,mu,k,lamda,Vmag,U1,U2,U3,U4]=MacCormack(u,utop,...
    ubottom,v,vtop,vbottom,rho,P,Poutlet,e,T,Ts,Ttop,Tbottom,Tref,...
    mu,muref,k,Cv,Cp,xp,yp,xps,yps,lamda,dx,dy,dxs,dys,dt,R,Pr,...
    Pin,Tin,I);


Save = mod(I,20000);


if Save == 0;
    save Run2
end


It = mod(I,10);


if It ==0
    disp(I);
end;


U1old = U1;
U2old = U2;
U3old = U3;
U4old = U4;


if dt < 1e-12
```

```
            break
        end


    Iteration = Iteration + 1;
    Dt(I,1) = dt;
end;


[u,v,P,T,rho] = Boundary(rho,u,utop,ubottom,v,vtop,vbottom,...
    P,Pin,Poutlet,T,Tin,Ttop,Tbottom,gamma,xp,yp,R);


surf(P);
```

Section 2: MacCormack method

```
function
[rho,u,v,e,T,Ts,P,mu,k,lamda,Vmag,U1,U2,U3,U4]=MacCormack(u,...

    utop,ubottom,v,vtop,vbottom,rho,P,Poutlet,e,T,Ts,Ttop,Tbottom,Tref,...

    mu,muref,k,Cv,Cp,xp,yp,xps,yps,lamda,dx,dy,dxs,dys,dt,R,Pr,Pin,Tin,I);


av = .2;

gamma = Cp/Cv;

Vmag = (u.^2+v.^2)/2;

Et = P./T./R.*(T.*Cv+Vmag);


%Calculate input quantities

U1 = P./T./R;

U2 = U1.*u;

U3 = U1.*v;

U4 = Et;


%Calculate E quantities

c = 1;

etauxy = etxy(u,v,c,mu,dx,dy,dys,xp,yp,xps,yps);

c = 1;

etauxx = etxx(u,v,c,mu,dx,dy,dys,xp,yp,xps,yps,lamda);

c = 1;

qx = -k.*ddx(dx,dy,xp,yp,xps,yps,T,c);


E1 = U1.*u;

E2 = U1.*(u.^2) + P - etauxx;

E3 = U1.*u.*v - etauxy;
```

```
E4 = (Et+P).*u - u.*etauxx - v.*etauxy + qx;
```

%Calculate F quantities

```
c = 1;
ftauxy = ftxy(u,v,c,mu,dx,dy,dys,xp,yp,xps,yps);
c = 1;
ftauyy = ftyy(u,v,c,mu,lamda,dx,dy,dys,xp,yp,xps,yps);
c = 1;
qy = -k.*ddy(dx,dy,dys,xp,yp,xps,yps,T,c);
```

```
F1 = U1.*v;
F2 = U1.*u.*v - ftauxy;
F3 = U1.*(v.^2) + P - ftauyy;
F4 = (Et+P).*v - u.*ftauxy - v.*ftauyy + qy;
```

%Artificial Viscosity

```
c = 5;
```

```
dPdx = ddx(dx,dy,xp,yp,xps,yps,P,c);
dPdy = ddy(dx,dy,dys,xp,yp,xps,yps,P,c);
```

```
c = 4;
dU1dx = ddx(dx,dy,xp,yp,xps,yps,U1,c);
dU1dy = ddy(dx,dy,dys,xp,yp,xps,yps,U1,c);
dU2dx = ddx(dx,dy,xp,yp,xps,yps,U2,c);
dU2dy = ddy(dx,dy,dys,xp,yp,xps,yps,U2,c);
```

```
dU3dx = ddx(dx,dy,xp,yp,xps,yps,U3,c);

dU3dy = ddy(dx,dy,dys,xp,yp,xps,yps,U3,c);

dU4dx = ddx(dx,dy,xp,yp,xps,yps,U4,c);

dU4dy = ddy(dx,dy,dys,xp,yp,xps,yps,U4,c);


Cx = av*dPdx;

Cy = av*dPdy;


S1 = Cx.*dU1dx + Cy.*dU1dy;

S2 = Cx.*dU2dx + Cy.*dU2dy;

S3 = Cx.*dU3dx + Cy.*dU3dy;

S4 = Cx.*dU4dx + Cy.*dU4dy;


%Predictor


c = 0;


U1bar = U1 - (dt)*ddx(dx,dy,xp,yp,xps,yps,E1,c) -...
   (dt)*ddy(dx,dy,dys,xp,yp,xps,yps,F1,c) + S1;


U2bar = U2 - (dt)*ddx(dx,dy,xp,yp,xps,yps,E2,c) -...
   (dt)*ddy(dx,dy,dys,xp,yp,xps,yps,F2,c) + S2;


U3bar = U3 - (dt)*ddx(dx,dy,xp,yp,xps,yps,E3,c) -...
   (dt)*ddy(dx,dy,dys,xp,yp,xps,yps,F3,c) + S3;


U4bar = U4 - (dt)*ddx(dx,dy,xp,yp,xps,yps,E4,c) -...
```

```
(dt)*ddy(dx,dy,dys,xp,yp,xps,yps,F4,c) + S4;
```

```
%Decode U matrices into primitive variables
rho = U1bar;
u = U2bar./U1bar;
v = U3bar./U1bar;
e = U4bar./U1bar -(u.^2 + v.^2)./2;
T = e./Cv;
P = rho.*R.*T;
mu = Sutherland(muref,T,Tref);
lamda = -2/3.*mu;
k = mu.*Cp./Pr;
Vmag = (u.^2+v.^2)/2;
Et = rho.*(T*Cv+Vmag);
```

```
% %Apply boundary conditions
[u,v,P,T,rho] = Boundary(rho,u,utop,ubottom,v,vtop,vbottom,...
    P,Pin,Poutlet,T,Tin,Ttop,Tbottom,gamma,xp,yp,R);
```

```
U1bar = P./T./R;
U2bar = U1bar.*u;
U3bar = U1bar.*v;
U4bar = Et;
```

```
etauxx = zeros(yp,xp);
etauxy = zeros(yp,xp);
ftauyy = zeros(yp,xp);
```

```
ftauxy = zeros(yp,xp);

qx = zeros(yp,xp);

qy = zeros(yp,xp);


%Calculate Ebar quantities

c = 0;

etauxy = etxy(u,v,c,mu,dx,dy,dys,xp,yp,xps,yps);

c = 0;

etauxx = etxx(u,v,c,mu,dx,dy,dys,xp,yp,xps,yps,lamda);

c = 0;

qx = -k.*ddx(dx,dy,xp,yp,xps,yps,T,c);


E1bar = U1bar.*u;

E2bar = U1bar.*(u.^2) + P - etauxx;

E3bar = U1bar.*u.*v - etauxy;

E4bar = (Et+P).*u - u.*etauxx - v.*etauxy + qx;


%Calculate Fbar quantities

c = 0;

ftauxy = ftxy(u,v,c,mu,dx,dy,dys,xp,yp,xps,yps);

c = 0;

ftauyy = ftyy(u,v,c,mu,lamda,dx,dy,dys,xp,yp,xps,yps);

c = 0;

qy = -k.*ddy(dx,dy,dys,xp,yp,xps,yps,T,c);


F1bar = U1bar.*v;

F2bar = U1bar.*u.*v - ftauxy;
```

```
F3bar = U1bar.*(v.^2) + P - ftauyy;

F4bar = (Et+P).*v - u.*ftauxy - v.*ftauyy + qy;
```

%Artificial Viscosity

```
c = 5;


dPdx = ddx(dx,dy,xp,yp,xps,yps,P,c);

dPdy = ddy(dx,dy,dys,xp,yp,xps,yps,P,c);


c = 4;

dU1dx = ddx(dx,dy,xp,yp,xps,yps,U1bar,c);

dU1dy = ddy(dx,dy,dys,xp,yp,xps,yps,U1bar,c);

dU2dx = ddx(dx,dy,xp,yp,xps,yps,U2bar,c);

dU2dy = ddy(dx,dy,dys,xp,yp,xps,yps,U2bar,c);

dU3dx = ddx(dx,dy,xp,yp,xps,yps,U3bar,c);

dU3dy = ddy(dx,dy,dys,xp,yp,xps,yps,U3bar,c);

dU4dx = ddx(dx,dy,xp,yp,xps,yps,U4bar,c);

dU4dy = ddy(dx,dy,dys,xp,yp,xps,yps,U4bar,c);


Cx = av*dPdx;

Cy = av*dPdy;


S1bar = Cx.*dU1dx + Cy.*dU1dy;

S2bar = Cx.*dU2dx + Cy.*dU2dy;

S3bar = Cx.*dU3dx + Cy.*dU3dy;

S4bar = Cx.*dU4dx + Cy.*dU4dy;
```

```matlab
%Corrector
c = 1;


U1 =.5*(U1+U1bar-(dt)*ddx(dx,dy,xp,yp,xps,yps,E1bar,c)-...
    (dt)*ddy(dx,dy,dys,xp,yp,xps,yps,F1bar,c)) + S1bar;


U2 =.5*(U2+U2bar-(dt)*ddx(dx,dy,xp,yp,xps,yps,E2bar,c)-...
    (dt)*ddy(dx,dy,dys,xp,yp,xps,yps,F2bar,c)) + S2bar;


U3 =.5*(U3+U3bar-(dt)*ddx(dx,dy,xp,yp,xps,yps,E3bar,c)-...
    (dt)*ddy(dx,dy,dys,xp,yp,xps,yps,F3bar,c)) + S3bar;


U4 =.5*(U4+U4bar-(dt)*ddx(dx,dy,xp,yp,xps,yps,E4bar,c)-...
    (dt)*ddy(dx,dy,dys,xp,yp,xps,yps,F4bar,c)) + S4bar;



%Decode U matrices into primitive variables


rho = U1;
u = U2./U1;
v = U3./U1;
e = U4./U1 -(u.^2 + v.^2)./2;
T = e./Cv;
P = rho.*R.*T;
mu = Sutherland(muref,T,Tref);
lamda = -2/3.*mu;
```

```
k = mu.*Cp./Pr;
```

```
%Apply Boundary conditions
[u,v,P,T,rho] = Boundary(rho,u,utop,ubottom,v,vtop,vbottom,...
    P,Pin,Poutlet,T,Tin,Ttop,Tbottom,gamma,xp,yp,R);
```

```
% Solid surface solution
Ts = Solid(Ts,dx,dy,dys,xp,yp,xps,yps,dt);
```

```
Cf(1:xp) = k(1,1:xp)/dy;
Cs(1:xp) = 3.3/dys;
```

```
%Interface temperature
Tinterface = (Cf.*T((yp-1),1:xp)+Cs.*Ts(2,1:xps))./(Cf+Cs);
```

```
T(1,1:xp) = Tinterface(1:xp);
Ts(1,1:xps) = Tinterface(1:xp);
```

Section 3: Boundary conditions

```
function [u,v,P,T,rho] = Boundary(rho,u,utop,ubottom,v,vtop,vbottom,...
    P,Pin,Poutlet,T,Tin,Ttop,Tbottom,gamma,xp,yp,R);


%U boundary conditions

uinlet(1:yp,1) = (((((Pin./P(1:yp,2)).^((gamma-1/gamma)-1).*...
    2./(gamma-1)).^.5).*(gamma.*R.*T(1:yp,1)).^.5;;
uoutlet(1:yp,1) = 2*u(1:yp,xp-1)-u(1:yp,xp-2);


%V boundary conditions

vinlet(1:yp,1) = 2*v(1:yp,2)-v(1:yp,3);
voutlet(1:yp,1) = 2*v(1:yp,xp-1)-v(1:yp,xp-2);


%P boundary conditions

Ptop(1,1:xp) = 2*P(2,1:xp)-P(3,1:xp);
Pinlet(1:yp,1) = (((((Pin./P(1:yp,2)).^((gamma-1)/gamma)-1).*...
    2./(gamma-1)).^.5).*(gamma.*R.*T(1:yp,1)).^.5;
Poutlet(1:yp,1) = 2*P(1:yp,xp-1)-P(1:yp,xp-2);


%T boundary conditions

Tinlet(1:yp,1) = Tin./(1+(gamma-1)/2.*(u(1:yp,1).^2+v(1:yp,1).^2)./...
    (gamma*R.*T(1:yp,1)));
Toutlet(1:yp,1) = 2*T(1:yp,xp-1)-T(1:yp,xp-2);
Ttop(1,1:xp) = 300;


%U matrix

u(1:yp,1) = uinlet;
```

```
u(1:yp,xp) = uoutlet(1:yp,1);

u(1,1:xp) = utop(1,1:xp);

u(yp,1:xp) = u(yp-1,1:xp);
```

```
%V matrix

v(1:yp,1) = vinlet(1:yp,1);

v(1:yp,xp) = voutlet(1:yp,1);

v(1,1:xp) = vtop(1,1:xp);
```

```
%P matrix

P(1,1:xp) = Ptop(1,1:xp);

P(yp,1:xp) = P(yp-1,1:xp);

P(1:yp,xp) = Poutlet(1:yp,1);

P(1:yp,1) = Pinlet(:,1);
```

```
%T matrix

T(1:yp,xp) = Toutlet(1:yp,1);

T(1:yp,1) = Tinlet(1:yp,1);

T(yp,1:xp) = T(yp-1,1:xp);
```

```
%rho

rho(yp,1:xp) = P(yp,1:xp)./T(yp,1:xp)./R;
```

Section 4: Shear Stresses

```
function etxx = tauxx(u,v,c,mu,dx,dy,dys,xp,yp,xps,yps,lamda)


lamda = -(2/3)*mu;


d = c;
a = ddx(dx,dy,xp,yp,xps,yps,u,c);
c = 2;
b = ddy(dx,dy,dys,xp,yp,xps,yps,v,c);
c = d;


etxx = lamda.*(a+b)+2*mu.*a;



function etxy = tauxy(u,v,c,mu,dx,dy,dys,xp,yp,xps,yps);


d = c;
a = ddx(dx,dy,xp,yp,xps,yps,v,c);
c = 2;
b = ddy(dx,dy,dys,xp,yp,xps,yps,u,c);
c = d;


etxy = mu.*(a+b);
```

```
function ftxy = tauxy(u,v,c,mu,dx,dy,dys,xp,yp,xps,yps);


d = c;
a = ddy(dx,dy,dys,xp,yp,xps,yps,u,c);
c = 2;
b = ddx(dx,dy,xp,yp,xps,yps,v,c);
c = d;


ftxy = mu.*(a+b);


function ftyy = tauyy(u,v,c,mu,lamda,dx,dy,dys,xp,yp,xps,yps);


lamda = -(2/3)*mu;


d = c;
a = ddy(dx,dy,dys,xp,yp,xps,yps,v,c);
c = 2;
b = ddx(dx,dy,xp,yp,xps,yps,u,c);
c = d;


ftyy = lamda.*(a+b)+2*mu.*a;
```

Section 5: Differencing schemes

```
function ddx = fdif(dx,dy,xp,yp,xps,yps,P,c)

dPdx = zeros(yp,xp);

%% Forward differencing scheme

if c == 0

dPdx(1:yp,1:(xp-1)) = (P(1:yp,2:xp) - P(1:yp,1:(xp-1)))/dx;
% dPdx(1:yp,xp) = (P(1:yp,xp)- P(1:yp,(xp-1)))/dx;

ddx = dPdx;

end

%% Rearward differencing scheme

if c == 1

dPdx(1:yp,2:xp) = (P(1:yp,2:xp) - P(1:yp,1:(xp-1)))/dx;
% dPdx(1:yp,1) = (P(1:yp,2) - P(1:yp,1))/dx;

ddx = dPdx;
```

```matlab
        end


        %%% Central differencing scheme


        if c == 2


        dPdx(1:yp,2:xp-1) = (P(1:yp,3:xp)-P(1:yp,1:(xp-2)))/(2*dx);          %central

        % dPdx(1:yp,xp) = (-3*P(1:yp,xp) + 4*P(1:yp,(xp-1)) - P(1:yp,(xp-2)))/(2*dx);
%rearward

        % dPdx(1:yp,1) = (-3*P(1:yp,1) + 4*P(1:yp,2) - P(1:yp,3))/(2*dx);
%forward


        ddx = dPdx;


        end


        %%% Central differnce second derivative


        if c == 3


        dPdx = zeros(yps,xps);

        dPdx(1:yps,2:(xps-1)) = (P(1:yps,1:(xps-2)) - 2*P(1:yps,2:(xps-1)) +
P(1:yps,3:xps))/dx^2;

        dPdx(1:yps,xps) = (-3*P(1:yps,xps) + 4*P(1:yps,(xps-1)) - P(1:yps,(xps-
2)))/(2*dx); %rearward

        dPdx(1:yps,1) = (-3*P(1:yps,1) + 4*P(1:yps,2) - P(1:yps,3))/(2*dx);
%forward

        ddx = dPdx;
```

```
end


%% Central differnce second derivative


if c == 4


dPdx = zeros(yp,xp);
dPdx(1:yp,2:(xp-1)) = (P(1:yp,1:(xp-2)) - 2*P(1:yp,2:(xp-1)) + P(1:yp,3:xp));
ddx = dPdx;


end


%% Central differnce second derivative


if c == 5


dPdx = zeros(yp,xp);
dPdx(1:yp,2:xp-1) = abs(P(1:yp,1:xp-2)-2*P(1:yp,2:xp-1)+P(1:yp,3:xp))./(P(1:yp,1:xp-2)+2*P(1:yp,2:xp-1)+P(1:yp,3:xp));
ddx = dPdx;


end
```